EXPLORING THE SOLAR SYSTEM WITH THE NOIRLAB SOURCE CATALOG

by

Katie Marie Fasbender

A dissertation submitted in partial fulfillment
of the requirements for the degree

of

Doctor of Philosophy

in

Physics

MONTANA STATE UNIVERSITY
Bozeman, Montana

July 2024

DEDICATION

for David Nidever, my academic advisor
for my teachers and mentors
for staff, administrators, technicians
for my friends and kindred spirits
and, most of all, for my family

ACKNOWLEDGEMENTS

Computational efforts were performed on the Hyalite High Performance Computing System and the Tempest Research Cluster, operated and supported by University Information Technology Research Cyber infrastructure (RCI) at Montana State University.

I would like to acknowledge and thank the RCI team for their endless work and assistance in providing learning and existing researchers at MSU with a high-quality source of computation.

I would also like to acknowledge and thank the members of my graduate committee, Dr. David Nidever, Dr. Anne Lohfink, Dr. Angela Des Jardins, and Dr. Hang Yu, for their time, patience, and efforts, and for lending their expertise in the thoughtful reviewing of this work.

Funding for this work was provided by the Montana Space Grant Consortium Graduate Fellowship (`https://spacegrant.montana.edu`), the National Science Foundation's National Optical-Infrared Research Laboratory (`https://noirlab.edu`), the National Optical Astronomy Observatory (`https://www.noao.edu`).

VITA

Katie Marie Fasbender was born in Mountain View, Califorina in September of 1994 to Cory Alan Fasbender and Leticia Castillo Fasbender. She grew up in the south San Francisco Bay Area with her brother, Adam.

Katie graduated from Homestead High School in Cupertino, California in 2012. She graduated with a Bachelors of Science in Physics with a concentration in Astronomy from California Polytechnic University, Humboldt (then Humboldt State University) in May of 2017. In 2022, Katie earned a Masters degree in Physics from Montana State University.

TABLE OF CONTENTS

TABLE OF CONTENTS – CONTINUED

LIST OF TABLES

LIST OF FIGURES

LIST OF FIGURES – CONTINUED

Figure Page

LIST OF FIGURES – CONTINUED

Figure | Page

LIST OF FIGURES – CONTINUED

Figure Page

LIST OF FIGURES – CONTINUED

LIST OF FIGURES – CONTINUED

Figure | Page

NOMENCLATURE

$^\circ$	Angular degree
$''$	Arcsecond
	$1''\text{hr}^{-1} = 1^\circ/3600$
AU	Astronomical Unit (average Earth-Sun distance);
	$1AU = 1.496 * 10^{11}$ meters
MJD	Modified Julian Date [days]
μ	Apparent/Observed/Proper motion [$''\text{hr}^{-1}$, $^\circ\text{day}^{-1}$, etc.]
mag	Magnitude (logarithmic scale of brightness)

Geocentric Equatorial Coordinates

α	Right Ascension (RA) from vernal equinox [0-360°]
δ	Declination (Dec) from celestial equator [±90°]

Geocentric Ecliptic Coordinates

l	Longitude from vernal equinox [0-360°]
b	Latitude from ecliptic plane [±90°

Proper Orbital Elements

a	semimajor axis [AU]
e	eccentricity [0-1]
i	inclination of from ecliptic [°]
Ω	ascending node [degrees]
ω	argument of perihelion [°]
ν	true anomaly [°]
α	phase angle (Sun-Object-Earth angle) [°]

ABSTRACT

Millions of objects, from micrometer-sized grains of dust to the largest main planets, orbit and interact with the sun and each other. Their relative proximity makes them important topics of study, but their relative size and complex apparent motion makes them difficult to find. Further calculations of SSO motion, magnitude, size, color, and rotation are needed for a complete and accurate model of the solar system in order to reveal how such a large number of objects interact and evolve together. The National Science Foundation's Optical-Infrared Astronomy Research Laboratory (NOIRLab) hosts a collaboration of ground-based observatories which have been imaging the sky for years. All public images are combined periodically in the NOIRLab Source Catalog, a multi-billion-row amalgamation of independent datasets which currently cover over 80% of the sky with nine years of observations. The NSC's seven photometric filters and extensive spatial and temporal coverage make it an excellent resource for exploring our solar system. Two methods, CANFind and the Tough Transform, were developed to identify measurements of solar system objects in the NSC. 4 million observations of SSOs were found in the latest data release of the NSC; over three million of these detections represent objects unknown before the NSC was searched. Initial determination of object orbits reveals that objects across the inner and outer solar system are represented in the catalog. The colors of unknown objects are explored, showing that the phase angle of an observed object may impact blue surfaces more so than red surfaces. Furthermore, source measurement of over 500,000 exposures for the third data release of the NSC is in progress; a new method of measurement has been implemented, and tests are performed to establish a new set of reference catalogs for source calibration. These improvements will undoubtedly positively affect the quality and quantity of SSO measurements represented in the NSC.

INTRODUCTION

Solar system objects, our closest celestial companions, orbit our sun with us at a huge range of distances. We've been observing them for thousands of years, yet details of their nature have only been revealed in the past few decades. Advancements in observational and computational abilities have resulted in an explosion of new discoveries of objects and their characteristics, in turn advancing our knowledge of the solar system our planet is a part of.

Rocky asteroids, icy dust-covered comets, and "centaurs" which display characteristics of both are distributed among Earth and the seven other main planets, and numerous dwarf planets, today in a way that is intricately connected to the system's evolution as a whole. Even while most of these objects remain unvisited by humans, documentation of their orbits and measurement of the sunlight reflected off their surfaces reveals a multitude of information which paints an elaborate picture of our local neighborhood. Over a million objects in the solar system have been detected, but observation continues as a majority of these objects are not well-studied, and millions more remain unidentified.

The NOIRLab Source Catalog (NSC), established in 2017 (Nidever et al., 2018) and updated every few years with public data from ground-based telescopes, is a multi-billion row source catalog which covers over 80% of the sky with 9 years of images in the optical-infrared regime. Vast sky coverage, measurements of faint objects in multiple photometric passbands, and nearly a decade of data make the NSC a useful resource for many kinds of science. We search for detections of solar system objects (SSOs) in the NSC with two curated methods: the Computationally Automated NSC tracklet Finder (CANFind, Chapter 3) and the Tough Transform (Chapter 4). In both published data releases, millions of observations of thousands of asteroids were identified in all seven of the NSC's filters.

This chapter will provide a short background of photometric observing from ground-based instruments and standard processing methods for corresponding data, and an overview of relevant solar system objects: their detection, determination of orbits, their observed characteristics, and the hypothesized evolution of the main asteroid belt. The rest of the chapter covers a brief outline of this work.

A description of the NOIRLab Source Catalog and development of its upcoming third release of data is found in Chapter 2. Chapter 3 describes CANFind, the first method created to identify solar system objects in the NSC, and the measurements found in the first data release. Chapter 4 introduces the Tough Transform, a supplemental SSO detection method to CANFind, and describes the SSO measurements identified in NSC DR2. Finally, a summary of techniques and findings and an outline of future work to be completed is provided in the Conclusion, Chapter 5.

Observing

All data used for this project were observed from ground-based telescopes in the optical-infrared regime of the electromagnetic spectrum. An overview of relevant topics follows, starting with the concept of photometric observation and finishing with the measurement and calibration of observed sources.

Photometry

Objects as distant as celestial sources, within and outside of our solar system, are either unreachable or to say the least challenging to observe in close proximity. All we receive from them is the energy they radiate across the electromagnetic spectrum, from short-wavelength, high-energy ultraviolet radiation at one extreme to low-energy radio frequencies at the opposite end. Photometry, the measurement of radiation from a source, is a vital method of collecting and recording information in all fields of astronomy. The ability to not only observe but record light from billions of galaxies, stars, and rocks provides the framework for countless theories and discoveries.

Photometric observations of light are constrained to “passbands” or “filters” that cover discrete portions of the electromagnetic spectrum. Only light within a filter’s wavelength range can be measured through that filter. Each passband has a characteristic transmission curve (TC) which describes the fraction of light transmitted through the filter at a given wavelength. The flux, or intensity, of photons passing through a filter can be recorded by taking an image, usually with a charge-coupled device (see Chapter 2) that converts the number of incident photons in each of its sensor’s pixels to an electric charge, then read and recorded by a computer. To illustrate the filters of a passband system, Figure 1.1 shows all seven of the photometric filters referenced in this work.

The flux of a source measured through a filter can be converted into the magnitude system, a logarithmic scale of brightness. The relation between flux f and magnitude m is

$$m = -2.5log_{10}(f) + ZP, \tag{1.1}$$

where ZP represents the “zero point” magnitude, which an object would exhibit if it produced one count per second on the detector being used to observe it. To maintain some sort of regularity between countless independent observers, magnitudes are measured and calibrated with respect to the common zero point value.

To measure the brightness of a source, its angular cross-section on the must be considered. The energy radiated from any one source extends over all of the sky, overlapping with the radiation from all the sources around it. The number of pixels that are used to calculate the brightness of the single source may be constrained to an aperture, usually a circular or elliptical area centered on the source. Only the light within the aperture is considered, only a fraction of the total light to be measured from the source. Small apertures

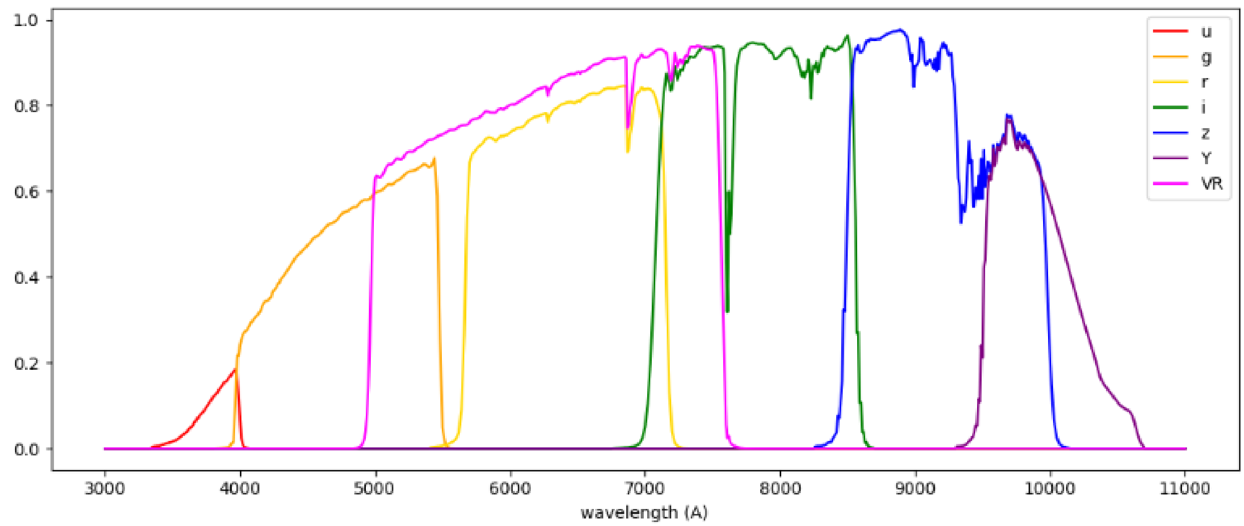

Figure 1.1 Transmission curves for the Dark Energy Camera (DECam, Flaugher et al., 2015) passband system, with atmospheric and instrumental TCs included, used to obtain much of the archival dataset (the NOIRLab Source Catalog, Chapter 2).

identify a greater ratio of the source's light to the background radiation contributed by all other sources, where larger apertures include more total light from the source but more background as well. By changing the size of the aperture to include more or less of the background sky and calculating the flux for each size, an estimate of the brightness and of the background radiation from all other sources can be obtained; this is the basis of aperture photometry. There are other ways to determine source brightness, one of which will be discussed further in Chapter 2.

If a source is observed in two different bands, the difference in magnitude between the two detections is interpreted as the color index. "Blue" colors indicate an excess in magnitude measured with the bluer of the two filters, while red colors indicate an excess in the "redder" filter. A source's color depends on some combination of several factors: its temperature, its composition, its rate of motion relative to an observer, the filters used to measure the source and calculate its color, etc. This information can all be determined with the right analysis.

Once intercepted, photons that have often traveled billions of miles from their source can be carefully recorded to measure its source's brightness and color to then reveal clues about the source's location, composition, age, and classification relative to other objects. The question of how to infer their nature falls to the quality and quantity of photometric observations, as well as the type of object being observed.

Ground-based Observing

Reflecting telescopes in the optical and infrared range of wavelengths capture exposures, or images, of the sky from the ground or from space with increasing regularity as technology permits for more industrious and ambitious missions. The biggest drawback to this method of observing is the presence of the Earth's atmosphere. It is a challenging element to account for - observing around the horizon is difficult, and even when looking directly up at the zenith, the atmosphere introduces noise and distortion to the images, limiting the precision and quality of measurements. Light traveling through the atmosphere scatters off of its particles and produces a warped image of its source. Because of this scatter, the stars are unobservable in the optical region for the half of each day when the Earth has rotated so that an observatory is on the side of the planet illuminated by the sun. Even during the night, light from far more distant celestial objects is affected by our atmosphere.

To complicate matters, this motion of the Earth must always be accounted for. The constant rotation around its axis and motion about the sun and sometimes our solar system's trajectory through the galaxy significantly affects observation coordinates and apparent flux. If a telescope's aim is not adjusted, long exposure times may cause stars to leave trailed images, introducing uncertainty in their measurement. This effect is very significant in the observation of solar system objects, which exhibit a large range of proper motions that often leave their detections trailed.

However, benefits of ground observing are worth the tradeoff. Damaged or malfunctioning equipment is replaced far more easily if nothing has to be to space. The details of developing instruments become far less convoluted without consideration of the various damaging effects the machines will experience outside of the protection of Earth's atmosphere. Instruments and sensors can be added or traded more frequently to achieve a wider variety of observing uses.

Images subject to atmospheric effects can be adjusted to counteract distortion. Calibration of images, and of the sources identified in them, should always follow observation.

Measurement and Calibration of Sources

Once images are taken, the precise location and brightness of each source is measured and calibrated. This is a standard step taken when making astronomical observations, especially when preparing a reference dataset or a large catalog.

An image is represented by an array of pixel values, each recording the incoming flux from whatever source's photons intercepted its sensor on the camera. A single image can capture thousands, or millions, of sources, and the position of each can be determined by finding their corresponding peaks in the image array in pixel units then converting to a sky location. Coordinates can be measured with great care, but should still always calibrated with reference to a different catalog that is known to have accurate measurements of sky position, or astrometry. This is astrometric calibration.

The brightness of each source is also calculated from the pixels that captured it. This flux may be converted to a magnitude value which is also calibrated against a reference catalog that, again, is known to possess accurate photometry. Sources in varying brightness and color are all measured relative to a common zero-point magnitude. Achieving a uniform zero point across a set of images in a survey or catalog, each image independently calibrated, is highly desired.

Solar System Objects (SSOs)

Our sun is estimated to be approximately 4.5 billion years old, and the gaseous disk from which it formed also provided the material to form most of the bodies that still orbit it today. Although solar system objects (SSOs) are the closest objects to the Earth, their faintness makes them quite difficult to find. The first objects discovered, other than the classical planets, were large, nearby bodies. Their proximity made it easier to see them than objects further away from both the earth and sun. In fact, most of the light we see when observing SSOs is sunlight reflected off their surface, so they can remain quite faint unless they approach the Earth, making the most nearby objects easiest to identify.

Elaborated upon in the following sections, SSOs appear to move at a very fast rate with relation to the more distant stars and galaxies due to the parallax effect. The closer an object is to an observer on Earth, the greater its proper motion; it would appear to move faster than a more distant object moving at the same rate. Both target (SSO) and observer (always Earth in the case of this work) are in motion, causing SSOs trace complex apparent paths in the sky as they wander amongst the more stationary distant stars, paths that can be predicted with great accuracy if observed for long enough.

The sun imparts a considerable gravitational force to cause this motion, but this is not the only way it effects the SSOs around it. Its intense radiation across the electromagnetic spectrum affects object spins, orbits, and surface evolution. “Space weathering” caused by the sun is most prominently experienced by small bodies which lack an atmosphere and by objects in the inner solar system, leaving SSOs further out with more of the unchanged, “pristine” material that they formed from in the early days of the solar system. The following sections include observational examples of this.

So great is the number of discovered SSOs that the matter of classifying objects by their features is a complex matter. They are categorized by their various characteristics: color, surface texture, size, shape, rotation period, orbit, etc.

A very relevant parameter is an SSO's distance from the sun; SSOs are observed in all different regions of the solar system, with icy objects and gas giants most prominent at greater distances and more rocky surfaces that experience the effects of the sun more acutely in the interior spaces. The formation and migration of the main planets, namely Jupiter, shaped the solar system into its current distribution of matter and orbits. An object's current orbit is likely not the one in which it formed. Comparing populations of SSOs at various distances from the sun through simulation (Nesvorný et al., 2024), identifications of dynamical relations between objects (Ferrone et al., 2023), or considering patterns in large numbers of objects (Dermott et al., 2023) constrains the possible histories of the system.

As mentioned, object's proximity to the sun will affect its chemical evolution. The main processes of space weathering include bombardment from cosmic rays, meteorites, and micrometeorites, and the irradiation, implantation, and sputtering/spitting of particles onto or off of an object's surface due to solar wind (Nesvorný et al., 2005). Smaller SSOs with little to no atmosphere are particularly subject to space weathering, a phenomenon caused by the impact of incident particles and solar radiation on surfaces which lack the protection of a gaseous envelope. Various effects of this, from the slight alterations to an object's orbit to the gradual change in its surface composition, are touched on in the following subsections, and Chapter 4 provides additional background.

Objects are additionally classified by size and shape, which are usually related. All of the main planets, most of the dwarf planets, many of their natural satellites, and some particularly large asteroids have accrued enough mass to overcome rigid-body forces and become spherical under their own self-gravity. Through gravitational pressure, radioactivity of internal materials, and impacts, massive objects are heated enough that they partially melt and undergo differentiation, their heaviest materials sinking to the center to leave lighter substances near the surface.

Although object interiors cannot be directly studied in the optical regime, their surface composition and estimated mass infers what materials are likely to be layered within them. The observed color of SSOs, and to a greater extent their reflectance spectra, are also used to classify them into taxonomic groups (i.e. Bus and Binzel, 2002; DeMeo et al., 2009; Tholen and Barucci, 1989). This information provides characteristics of the object's surface, which likely has changed over time from its various interactions. Observed brightness and color depends on the observing conditions, the distance between target and observer, the visible cross-section of the target and by association the target's phase angle (the angle drawn between the Earth, the target, and the sun), and the target's composition, among other factors.

Small bodies display a much wider variety of shapes than their larger counterparts, and either lack an atmosphere or are surrounded by a very weak, disperse envelope. Apart from smaller natural satellites of the main planets, these objects consist mostly of minor planets (asteroids), some comets, and the occasional interstellar visitor. These populations are the focus of this work.

Brief History of SSO Observation

Before the use of telescopes for observing the sky was adopted by Galileo Galilei in 1608, the only objects in the earth's close proximity that had been identified by humans were the ones largest or closest enough to be seen with the naked eye. Mercury, Venus, Mars, Jupiter, and Saturn were not known to be planets as the Earth was, as they appeared to be the same as the rest of the stars apart from their constant wandering across the sky Once inspected in closer detail, the detailed features of each of the known planets and the moon made apparent that the wandering lights were far more complex than they had always appeared.

Not by coincidence, the first solar system object (SSO) other than the "classical" main planets to be discovered is also the largest known minor body, 1 Ceres, a nearby resident of the main asteoid belt (Cunningham et al., 2009). In 1801, astronomer and priest Guiseppe Piazzi observed Ceres through a refractor telescope, initially believing it to be a star until realizing upon his next observation that it had changed position relative to the other stars in the field. Ceres was in fact lost after about 40 days of observation once it disappeared behind the sun, and it was only recovered through prediction of its orbit around the sun in the first practical application of Kepler's Laws to Planetary motion, calculated by mathematician Carl Friedrich Gauss (see the following subsection).

In the following years, more of the largest minor bodies were identified through telescope observations (2 Pallas, 3 Juno, 4 Vesta), but the only way to record their presence and motion was to draw their position in relation to the motionless stars they seemed to move through. The first asteroid to be discovered via astrophotography, 323 Brucia, was also serendipitously found by astronomer Max Wolf, who in 1891 noted a difference between the location of a source on glass plates (Campbell, 1892). Following this, hundreds of objects were detected in the same fashion in new and archival plates. They were yet to be observed in greater proximity, but it was clear that the companions of Earth were far greater in number than what had been followed by eye for thousands of years.

Astrophotography changed not only the science of solar system objects, but the entire field of astronomy. The next paradigm shift came with the computer, and the ability to not only record object information but analyze it faster than previously possible. The first automated asteroid detection program came at the end of the next century, written by Rabinowitz (1991) and identifying 304 asteroids with images from the Spacewatch Telescope.

This has become the standard method of SSO detection, yielding identifications of over a million objects in our solar system to date and revealing countless interactions and structures within the disk In order to understand our system's composition, history, and evolution, we must create the most complete model of how is matter distributed in the present day.

Orbit Determination

The first time the position of an object was predicted using a model of the solar system was in 1801 when Gauss applied Kepler's Laws to coordinates of Ceres. Kepler's Laws of Planetary motion dictate the general orbit of every body in the solar system; (1) that objects orbit in an ellipse with its sun at one focus, (2) that a line between the sun and object sweeps out segments of equal area in equal intervals of time, and (3) that square of the orbital period of an object is proportional to the cube of the semimajor axis of its orbit. Gauss made the assumption that these were the only three determiners of an object's orbit, and therefore used solely information of Ceres' measured position to make his calculations.

He estimated Ceres' future location by approximating its orbit with the measurements available and making guesses of the distances to Ceres at the epoch of observation. After calculating the resulting positions of Ceres under the assumption of this orbit, the discrepancies between observed and calculated positions were used to make adjustments to the original estimates of distance. A new orbit was calculated with the new guesses, and the process iterated until the calculated positions matched measured ones to within Variations of this method are still used to make initial estimation of SSO orbital parameters with few detections, for example, the method of Herget (1935) also makes assumptions about the distance between observer and target to iteratively converge on an orbital solution. This is the method used to estimate initial orbits of objects detected in Chapter 4

Determining accurate estimates of an SSO orbit is no easy feat; it usually requires many detections of an object over several months, and is not a static attribute. All objects in the solar system, including the sun, interact with one another in a complex dance of forces. Gravity is the dominant participant, most strongly affecting the objects orbiting the sun. The sun may be the most prominent mass in the nearby area, but the effect of gravity is felt between every pair of objects in the system, regardless of size. As a planet completes a full rotation around its star it passes by the other objects in the disk, the force of gravity increasing between them as they approach each other. In a system of millions of moving objects, the number of perturbers to an orbit constantly changes it so an object does not follow one path defined by itself and the sun. The resulting path that is observed from Earth is called an ephemeris, recorded positions of an SSO over its period of observation.

Other forces push and pull objects into new orbits as well. The Yarkovsky effect, a small thermal radiation force caused by outwards solar radiation that mainly affects asteroids with diameters less than 30-40 km, depends on an object's size, orbit, and composition (Vokrouhlický et al., 2015). The acceleration it causes is a fraction of the force felt by the sun and planets, but over millions to billions of years the Yarkovsky effect becomes apparent in the changing structures of the disk (Nesvorný et al., 2015). It also creates a thermal torque called the (YORP) effect that can increase/decrease objects' spin and affect spin axis orientation (Vokrouhlický et al., 2015).

These interactions force SSOs from their trajectories, altering orbits and bringing objects into proximity with even more new perturbers. The orbit calculated from one month of observations may differ from that calculated from observations taken in another month, so the ephemeris of an object is the best way to record its motion and make time-specific calculations of its orbital elements.

Characteristics of the Main Asteroid Belt

Through decades of photometric and spectroscopic monitoring across most wavelength ranges, astronomers have used the physical nature of SSOs to form a general model of the current state of our solar system and the interactions that occur between its inhabitants. Theories of its formation and future evolution depend strongly on the completeness of this model. The Main Asteroid Belt, the largest of our solar system, is home to countless diverse asteroids and provides constraints to the solar system's past. No confirmed comets reside in the belt, the difference between comets and asteroids being outgassing of volatile compounds from the surface of comet ("activity") and a comet's highly eccentric orbit that takes it very far from, then very close to, the sun. This distinction may change, however, with the discovery of active asteroids which maintain orbits in the main belt, but show signs of outgassing (Jewitt et al., 2015), another example of the importance of discovering new objects.

The belt sits between the orbits of Mars, the furthest terrestrial planet from the sun at 1.5 AU, and Jupiter, the closest gas giant at 5 AU. Roughly defined in the region between 2-3.5 AU, the Main Belt is filled with millions of objects but hosts only a fraction of the solar system's mass, estimated at $\sim 4.5 * 10^{-4} M_{Earth}$ (DeMeo and Carry, 2013; Krasinsky et al., 2002; Raymond and Nesvorný, 2022). Its members have dynamically excited orbits, meaning they are often highly eccentric ($0 \leq e \leq 0.3$, inclined from the ecliptic plane ($0 \leq i \leq 30°$), and often have unstable orbits that will eventually take them to another part of the solar system, or eject them completely (Nesvorný et al., 2015; Raymond and Nesvorný, 2022). The cause of this distribution is unknown; theories are introduced in the following section.

Certain types of material are known to be found in certain regions of the belt. To understand the exact surface composition of SSOs, spectral information is needed to identify signature traces left by specific compounds. However, the color of an object is a good approximator for spectral slope and can indicate the presence of large ratios of material. Asteroid colors are observed change throughout the belt; using the Tholen classification system of describing "S-type" asteroids as silicious and water-rich, "C-type" asteroids as carbonaceous and dry, the main belt is populated with S-type asteroids dominating the interior orbits, C-types populating the outer belt, and significant mixing between the two populations (Raymond and Nesvorný, 2022). The dichotomy of these two carbonaceous and non-carbonaceous groups likely indicates that these two groups formed seperately in the early solar system and were maintained, then disturbed from their orbits, by Jupiter's growth and migration (Kleine et al., 2020). Object colors indicate not only composition, but surface texture as well. For instance, (DellaGiustina, 2020) notes a relationship between surface morphology and color on asteroid Bennu. Zhang and Michel (2021) discusses the wide array of asteoid surfaces and discusses the various ways in which they can be changed, all of which contribute to an asteroid's color.

The main belt is home to dozens of collisional asteroid families, the members of which are fragments of a parent body which broke apart upon impact with another object (Nesvorný et al., 2015). When objects intercept each other, one or both of them may fragment or completely shatter. The leftover debris from the collision continues to orbit the sun, some of it maintaining a similar trajectory to the parent body or bodies, the rest ejected to another orbit or out of the solar system. The pieces that stay behind start out with the same orbital elements as their parent body, but disperse over time because of their different sizes and altered trajectories.

Collisional families are useful laboratories for studying the various forces and effects to which SSOs are subject (Knežević, 2020). Because the members all originate in common orbits, the degree of spread seen in their orbital elements is an indicator of the age of the family, i.e. when the collision occurred. This situation is also a rare chance to see the interiors of objects, which can usually not be accessed unless samples are physically retrieved or a collision is witnessed/initiated (i.e. the DART mission, Moreno et al., 2023). Asteroid magnitudes and colors are only reflective of their surface features, but a fragmented parent body provides exposed interior material for observation. Objects can be connected with parent bodies via spectroscopic similarities, for example, Gaia DR3 reflectance spectra was used to associate Bennu with the Eulalia collisional family (Delbo et al., 2023).

This framework of collisions in the Main Belt helps give context to its history, which is further illuminated by the distribution of surface colors and textures in the space.

Evolution of the Main Belt

It is necessary to be familiar with the theories of our solar system's evolution to understand how and why today's structure is so important. It is observed that SSOs with similar surfaces are present in different regions of the solar system, possibly indicating that many objects were removed from their location or origin (Trinquier et al., 2007). Objects of similar material may have formed in reservoirs between the growing planets.

The solar system started as a disk of gas and dust around the forming sun, a period referred to as the "gaseous disk phase." During this time, planetary embryos callled "planetesimals" formed from the pristine early-disk material and cleared their orbital path of debris. It is likely that primordial objects were massive enough to have undergone differentiation (Carry et al., 2021). Large planetesimals may have trapped other bodies through an outwards pressure trap (Lambrechts and Johansen, 2014) or by the disk itself (Brasser and Mojzsis, 2020). Objects trapped in reservoirs between planetesimals in the gaseous disk phase would have experienced little intermixing.

After dissipation of the gaseous disk, it possible that the gas giants underwent a period of migration, which would have disturbed the orbits of objects across the solar system and may have depleted the main belt of its original inhabitants. Objects in the disk may have even undergone gravitational self-stirring; a higher-mass disk of planetesimals excites itself due to mutual gravitational interactions faster and to a higher degree than a lower-mass disk (i.e. Ida and Makino, 1992; Kokubo and Ida, 2000; Wetherill and Stewart, 1989). Whether the main belt was depleted and repopulated via giant planet migration (Grand Tack scenario, O'Brien et al., 2014; Walsh et al., 2011), or if it originated as a low-mass belt that was populated after the gaseous disk phase (Hansen, 2009), or if it began as a dynamically-excited main belt that was depleted and repopulated (Clement et al., 2018), the model must produce the distribution of material observed in the main belt today.

Project Outline

The following chapters include a description of the updates being made to the NSC for its next data release (2), which will and two manuscripts regarding SSO detection and science with the NSC (3 and 4. The overarching goal of this project is to identify measurements of solar system objects in the NOIRLab Source Catalog, analyze their characteristics, and to work on the NSC itself.

Data: the NOIRLab Source Catalog

A perfect dataset to use for solar system science is the NOIRLab Source Catalog, covered in detail in Chapter 2. It consists entirely of archival data, already used for the original surveys or observing runs that they were part of. Archival data must be used to its full potential because celestial observations are expensive computationally, financially, and temporally.

The NOIRLab Source Catalog has been updated once (DR2, Nidever et al., 2021) and is due for a new release of data to include recent observations. A new method to measure sources is developed to improve accuracy in crowded regions by iteratively identifying, modeling, and subtracting sources from each exposure. As with DR1 and DR2, sources are identified with the Source Extractor (Bertin and Arnouts, 1996) software, which identifies sources through their isophotal footprint and measures their brightness with aperture photometry. Sources are now additionally measured via point-spread-function (PSF) modeling of select measurements with DAOPHOT (Stetson, 1987), a more precise way to determine position and magnitude than aperture photometry. The resulting catalog length will be significantly longer than previous data releases and will feature many faint sources in the galactic plane which may have been missed in previous data releases.

Astrometric calibration with Gaia coordinates for entire sky remains the same as before, updated to DR3 from DR2. Photometric calibration with synthetic photometry using GaiaXPy, in order to use same method on north and south hemispheres (previously was model magnitudes), is considered and ultimately rejected due to reddening and source crowding effects.

This chapter will contribute to a manuscript in preparation Fasbender et al., which will additionally describe the combination and ubercalibration of sources and performance of the final catalog.

Manuscript 1: Solar System Object Detection

The second chapter is a published manuscript, *Exploring the Solar System with the NOIRLab Source Catalog I: Detection with CANFind* (Fasbender and Nidever, 2021). The first manuscript regards the first SSO detection method developed to be applied uniformly on the entire NSC (CANFind). The process of identifying and validating tracklets of SSO measurements is described, as is a simulation that was written to test the efficiency of CANFind's tracklet detection for a range of apparent motion.

NSC DR1 was searched with CANFind, yielding 500,000 tracklets. Their observed proper motions indicate the presence of near-Earth objects, Main Belt asteroids, Jupiter Trojans, and Kuiper Belt Objects. Tracklets were detected in all seven photometric bands of the NSC with a majority showing detections in at least two bands. Many tracklets are observed in two colors, g-r,r-i being the most prevalent. Two groups in this color space, a red S-like group and a slightly smaller blue C-like group, reflect results from prior surveys and catalogs. This shows that SSOs in multiple regions of the solar system are represented in the NSC, and that they are well-measured because observation characteristics generally match those of known objects and expected values.

Input data for this project is the NSC Exposures table and the NSC Measurements table, queried using psql, joined on NSC Objects table. Python code written for this analysis and a description of its implementation is found at `https://github.com/katiefasbender/CANFind`.

Output data include a list of NSC measurements not associated with stars and galaxies, and a subset of those measurements which are associated with tracklets, saved in the file `cfdr2_tracklet_mmts.fits.gz`. These, along with a list of tracklets identified in the NSC with their positions, observation timespans, proper motions, and their colors (`cfdr2_tracklet_cat.fits.gz`) are also available at `https://github.com/katiefasbender/CANFind`.

Manuscript 2: Solar System Object Color Analysis

Exploring the Solar System with the NOIRLab Source Catalog II: Magnitude and Color in the Main Belt is a manuscript prepared for submission to the Astronomical Journal.

This chapter focuses on SSO detection and analysis in the second data release of the NSC (Nidever et al., 2021) with CANFind and the Tracklet Hough Transform, an adapted form of the Hough Transform for image feature extraction (Hough V, 1962).

4 million measurements of 600,000 tracklets are identified in NSC DR2 and crossmatched with observations from the Minor Planet Center[1], an organization which maintains a database of all known observations of all discovered asteroids. From 4 million, under a million observations were crossmatched with detections from the MPC database. These detections belong to objects outside of Earth's orbit, almost entirely in the Main Belt. Several hundred have color information and known rotation periods, but only a few have both.

Initial Orbit Determination (IOD) of all tracklets was implemented with the `Find_Orb` sofware (Gray, 2022). These estimated orbital elements are compared calculated orbital elements given in the MPC's orbital elements database `MPCORB.DAT.gz`, showing that while one night of observation is not sufficient to properly determine a tracklet's orbital elements,

[1] https://minorplanetcenter.net

it is enough to place it in the larger structure of the solar system.

Many tracklets have color information, again the most popular two being *g*-*r*,*r*-*i*. Analysis of color for objects in the main belt shows that the effect of phase angle on an object's observed color may be more prominent for blue surfaces than for red ones.

The Tough Transform will be made available once the manuscript has been published. Python code written to estimate tracklet orbits with `Find_Orb` is found at `https://github.com/katiefasbender/nsc_sso_orbits`. Scripts which handle catalog creation and cross-matching with MPC measurements are available at `https://github.com/katiefasbender/mpc_xmatch`.

Input data for this project again includes the NSC Exposures table, NSC Measurements table, and NSC Objects tables. Additionally, MPC observation and orbital element databases were obtained from `https://www.minorplanetcenter.net/iau/ECS/MPCAT-OBS/MPCAT-OBS.html`, and the Asteroid Light Curve Database is found at `https://sbn.psi.edu/pds/resource/lc.html`.

Output Data again include a list of tracklets and their measurements, as well as lists of crossmatched measurements and their associated objects, and a list of initial orbital elements for all tracklets. These will be found at `https://github.com/katiefasbender` once the manuscript has been published.

Conclusion and Future work

Finally, the next steps to be taken regarding both development of the NOIRLab Source Catalog and the analysis of SSOs represented in it will be covered in the conclusion, Chapter 5. Once a method has been determined for photmetric calibration of the NSC, processing will be started. The next steps, combination, and ubercalibration, will complete the dataset, updating the NSC with another several years of exposures.

Solar system science in the NSC is far from complete - although color has been explored, the size distributions and rotation periods should be calculated when possible. Members of asteroid families exist within the data; known objects have been identified, but new additions to families and even new family candidates may be found with closer inspection.

THE NOIRLAB SOURCE CATALOG

Background

The data of celestial source measurements used for every part of this work come from the all-sky NOIRLab Source Catalog (NSC). Combining years of data from independent surveys and proposals from NOIRLab's observatories, the NSC presents billions of source detections that are all measured, calibrated in position and brightness, then finally combined to identify unique objects using a standard method for the entire catalog. A third data release of 500,000 exposures is expected in 2024; the processing for this set of exposures is described in the following chapter.

The National Science Foundation has supported countless researchers in the United States since its formation in 1950, carrying the mission to promote the progress of science. To encourage collaboration, which is increasingly important as the finer details in astronomy are explored, in 2019 the NSF combined several independent, ground-based astronomy operations to establish the NSF's Optical-Infrared Astronomy Research Laboratory, or NOIRLab. NOIRLab provides the scientific community with a variety of observing capabilities in the optical-infrared wavelength regime, a dynamic set of science and technology collaborations, and a multi-faceted source of data.

Observations come from three of NOIRLab's programs; the International Gemini Observatory, Cerro Tololo Inter-American Observatory (CTIO), and Kitt Peak National Observatory (KPNO). All collect data in the optical-infrared wavelength regime with photometry and spectroscopy instruments paired with ground-based reflecting telescopes. CTIO and KPNO were formerly a part of the National Optical Astronomy Organization (NOAO), which focused on the same wavelength regime.

Both observatories house large telescopes which are paired with various imaging insturments that use charge-coupled devices (CCD) to convert photon count to an electrical charge. An integrated circuit which allows incident photons to be read by analog-to-digital electronics is etched onto silicon to form the surface of a CCD chip. Through the photoelectric effect, a mechanism in which releases electrons from a substrate hit by a photon that imparts enough energy for the electron to overcome its binding energy, a photon emitted from a celestial source which hits one of the pixels of a CCD surface releases a number of free electrons. A charge builds up in each pixel that is proportional to the intensity of light incident on that pixel; this electron count is read as an analog-to-digital unit (ADU) for each pixel. The pixel array forms an image from which the flux from each source captured over the duration of the exposure can be measured. Sources are measured in brightness and sky location, then calibrated in both.

NOIRLab catalogs all exposures in the Astro Data Archive[1], where they can be accessed once they become available to the public.

Previous Data Releases

The first data release of the NSC was established in 2017 and included seven years of public data from the NOIRLab Astro Data Archive, resulting in 34 billion source measurements from 250,000 exposures (Nidever et al., 2018) in the $ugrizY, VR$ bands. 2.9 billion unique objects were discerned from these measurements through combination with a $0.5''$search radius. The second data release (Nidever et al., 2021) increases in size to 69 billion measurements of 3.9 billion objects, from 412,000 exposures covering 9 years of observations.

Median depth in all seven photometric bands is $\sim$21 mag, with a limiting magnitude of about 23 mag. Most of the sky is covered in exposures; over 80% is filled in DR2. Approximately two thirds of the galactic plane, the magellanic clouds, and the entire southern hemisphere is included. A majority of exposures are captured in the *g,r,z* bands in both hemispheres. The same measurement and calibration methods are implemented on the entire

[1]https://astroarchive.noirlab.edu

sky, regardless of location or filter, to achieve the most uniform results possible.

The size and coverage of the catalog make it difficult to find an adequate reference to calibrate it against. Enough well-measured sources in all seven photometric bands must be found in every region, and there are few catalogs which can provide this. As a result, a combination of public catalogs is used for photometric calibration, along with model magnitudes where no reference is found (see (Nidever et al., 2018)). Astrometric calibration is not as restricted as only coordinates and proper motion are needed, and it is performed with reference to the Gaia catalog, which covers the entire sky (see the follwing section).

The photometric zero-point across the sky is not uniform and differs for each filter. It deviates particularly in the galactic plane, Magellanic clouds, and in the u-band, which has the fewest exposures. This offset may be due to the lack of a single reference catalog available for photometric calibration. It could also arise from a blending issue; source extraction in crowded areas of the sky is compromised in the need to apply a single, uniform measurement method to all exposures, and some sources are missed or extracted incorrectly.

Gaia Astrometry and Synthetic Photometry

The Gaia Space Mission (Gaia Collaboration et al., 2016b) is a project of the European Space Agency that scans the sky with the Gaia Spacecraft to create extremely well-measured, three-dimensional maps of stars in and outside of our galaxy. The recent third data release (Gaia Collaboration et al., 2023c) provides astrometry for $\sim$1.46 billion sources. The catalog of highly precise measures of source coordinates, parallax, and proper motion has a limiting magnitude of approximately 21 mag in the spacecraft's green photometric G band. To determine these source coordinates, Gaia observes thousands of stars simultaneously and calculates their relative separations.

The spacecraft includes a low-resolution spectrometer that captures blue and red photometer (BP/RP) spectral data in the 330-1050 nm range. The third data release is accompanied by a catalog of time-averaged mean BP/RP spectra for 220 million bright sources, mostly G≤17.65, each with a reasonable number of observations and an adequate signal-to-noise ratio.

From these mean spectra, a mean photometric flux can be calculated by integrating over the spectra and the transmission curve of a selected photometric filter within the spectra range, 300-1505 nm. the photometric flux is converted into a magnitude; this can be done for any requested set of filters within the Gaia range. The GaiaXPy Python Package[2] (Gaia Collaboration et al., 2023b) was developed to convert mean spectra from Gaia DR3 to synthetic fluxes and photometry for several photometric systems with filters between 330-1050 nm, including the DECam filters grizY.

Because synthetic photometry can be generated for any of Gaia's 200 million sources across the sky with mean spectra, it had the potential to act as a synthetic reference catalog for photometric calibration of the NSC in both celestial hemispheres. We considered this against Pan-STARRs (Chambers et al., 2016) and model magnitudes, which had performed well on previous data releases. Gaia Collaboration et al. (2023b) describes standardization in certain photometric filter systems by applying cuts in magnitude and color to avoid deviations caused by systemic differences between Gaia and other instruments, and from astronomical effects such as reddening, or extinction, from dust. Section 2 covers the testing executed to determine whether Gaia synthetic photometry provide a reliable reference for NSC calibration. The use of synthetic photometry was ultimately rejected for a numbe of reasons, also covered in section 2.

---

[2]https://gaia-dpci.github.io/GaiaXPy-website/

Processing of the Third Data Release

The process of identifying sources, measuring their coordinates and brightness, and calibrating both has changed considerably since the previous data release (Nidever et al., 2021). All exposures are measured and calibrated with the same standard methods, explained in the following sections.

Measurement

The measurement of sources has been expanded since DR2 to achieve a more complete catalog with Source Extractor (SExtractor or SE, Bertin and Arnouts, 1996), which is used for detection, measurement of positions, calculation of morphological parameters, and automatic aperture magnitudes. Now, sources are modeled with the DAOPHOT photometry software (Stetson, 1987) as well, allowing iterative source detection and subtraction. DAOPHOT additionally provides concentric aperture photometry for each source and calculation of aperture correction by growth curve for each chip. The entire measurement technique of source detection and PSF-modeling, both iterative processes, is summarized in Figure 2.1.

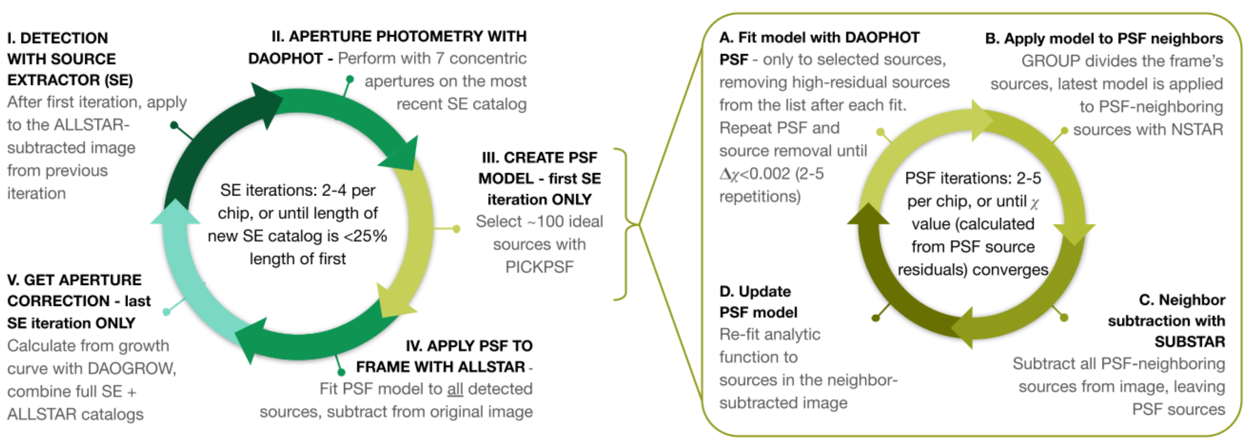

Figure 2.1 Flowchart of iterative source detection and PSF fitting in the measurements process described in Section 2.

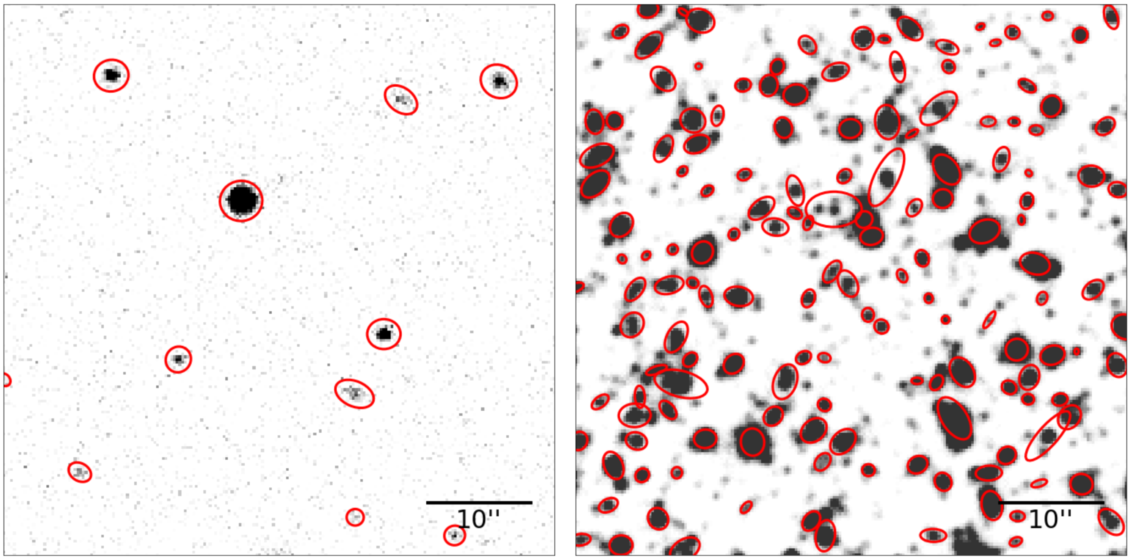

Figure 2.2 Comparison of source extraction in a low-density field *(left)* and a crowded field *(right)*. The number of sources overlapping and blending together in an exposure affects the quality of source measurement. This method was applied to DR1 and DR2.

I. Detection with Source Extractor Although a single application of SExtractor per chip accurately identifies a majority of objects and returns adequate sources for PSF fitting, it does not always produce desirable results in highly crowded fields. SExtractor's detection threshold (`DETECT_THRESH`), the value above which a pixel must have to be considered, would typically be chosen according to an exposure's field density. If `DETECT_THRESH` is set too high, the S/N of each source is improved but SE misses faint sources in crowded fields and near much brighter or saturated objects. If it is too low, SE has trouble distinguishing between adjacent sources in crowded areas. In order to apply the same analysis to every exposure regardless of the degree of crowding, a compromise in SE parameters was necessary: `DETECT_THRESH` was set to 1.1 for all exposures in DR1 and DR2.

This is not necessary for DR3, as the addition of PSF-fitting to the measurements process offers a workaround. After sources are detected from a chip, a PSF model can be created and then used to subtract them from the exposure to produce a new image with a lower maximum ADU value and lower object density. With the brightest sources removed, another round of source detection in this new "subtracted image" yields fainter objects that were missed by SE in the original exposure. As a result, maximizing the number of sources detected is no longer an issue in the first application of SE on a chip and `DETECT_THRESH` can be set to a higher value (1.7) without missing out on faint sources in crowded areas. SExtractor configuration files with a full list of parameters applied to NSC DR3 exposures is found at `https://github.com/astro-datalab/noaosourcecatalog/tree/master/python/nsc/config`.

II. Aperture Photometry with SE After each application of SExtractor, aperture photometry is performed on the resulting catalog by the DAOPHOT `PHOTOMETRY` routine with 7 concentric apertures (`APERTURE_RADIUS` = 3.0, 6.0803, 9.7377, 15.5952, 19.7360, `INNER_SKY_RADIUS` = 40.0, `OUTER_SKY_RADIUS` = 50.0 pixels) centered on each source. DAOPHOT returns a table of magnitudes for all sources along with the estimated magnitude limit for the exposure. Aperture photometry is completed for every SE catalog, so the results may be used to subtract the sources from the frame.

III. PSF Modeling with DAOPHOT In any exposure, the light from each source is spread to some degree due to effects from atmospheric turbulence and the imaging system used to detect it. This blurring, assumed to be relatively consistent across each field, adds uncertainty to the measurements taken of the exposure's sources. Because most objects can be approximated as point sources, better measurements can be achieved by modeling the dispersal of their light with a point-spread function (PSF), created by fitting an analytic function to at least one source from the field.

An ideal PSF should be fit on a bright, round source in an otherwise empty sky so that only its signal is counted towards the model. However, in a real scenario the signal from any source will be contaminated by light from the other sources in the sky, most significantly from brighter and nearby objects. A solution is to fit the PSF using a number of bright, round, and relatively isolated sources from the exposure that best approximate the scenario of point sources in an empty field devoid of other light. Because this is not always possible, especially in dense fields, we take several steps to address the complications of real-life PSF-fitting with an iterative modeling process using tools provided by DAOPHOT.

DAOPHOT accepts a number of parameter options. We set the `FITTING RADIUS` = full-width-half-max (FWHM) as calculated by SExtractor, and the `PSF RADIUS` to 4*FWHM, in pixels. The choice of analytic function is set to AN = -7 for first PSF fit, so that all seven analytic functions will be considered. After the initial fit, we reset AN to select the function that yielded the best model for every subsequent fit. The option files for DAOPHOT (`daophot.opt`) and ALLSTAR (`daophot.als.opt`) can be viewed at `https://github.com/astro-datalab/noaosourcecatalog/tree/master/python/nsc/config`.

To get the best sources for building a chip's model, this entire PSF-fitting process is completed only after the first round of SE. From this initial catalog, we use the DAOPHOT command `PICK` to select roughly 100 bright, round sources from the chip on which to start creating the model. `PICK` is given the chip's limiting magnitude as estimated by `PHOTOMETRY` and ignores sources that are fainter than this value, as well as those within one `FITTING RADIUS` away from the edge of the frame or within one `FITTING RADIUS + PSF RADIUS` from the center of a brighter or saturated source. There will inevitably be a number of PSF sources that do not adequately model the ideal PSF situation; these will be identified and removed from the list as the PSF is developed.

First, DAOPHOT `PSF` creates models for the seven analytic functions to compare and select the one that best describes the light spread in the chip. Each function is fit to the PSF sources, which are then subtracted from the frame. `PSF` returns the function's associated χ value, the root mean square of the residuals left within one fitting radius of each source's center, and chooses the function yielding the lowest value to build the model in every subsequent iteration. `PSF` also reports individual chi values for the PSF sources after subtracting them from the image with the selected analytic function, flagging any source with a chi value greater than two times the average. We remove these flagged objects from the PSF source list, as they negatively contribute to the frame's model.

We monitor each frame's χ value as a measure of how well the PSF has been fit, comparing $\Delta\chi$ between applications of DAOPHOT `PSF` as a metric to stop the iterative model-fitting process. We repeat the fit and update the source list up to five times to improve the model, removing flagged sources each time, until either no new sources are flagged or the difference in the frame's χ value between subsequent fittings of the model, $\Delta\chi$, changes by less than 0.002. This usually happens after 2-3 repetitions of re-fitting the model and removing high-residual sources from the PSF list.

`GROUP + NSTAR` are used to detect neighbors of PSF sources and apply the model to them. χ changes most dramatically after removing high-residual PSF sources that are identified every time the PSF is re-fit, but the model is also affected by the signal from neighboring sources. To identify the objects most likely to strongly contaminate a PSF source, we organize a chip's sources into groups. Two sources belong in the same group, according to DAOPHOT `GROUP`, if the light from one is strong enough to influence the profile-fit of the other.

PSF neighbors are then removed from the frame with DAOPHPT `SUBSTAR`. Using the latest PSF model, `SUBSTAR` creates a model for every neighbor and uses it to remove the neighbors from the image. The absence of neighbor stars results in a cleaner image that DAOPHOT then uses to recreate the model.

Updating the PSF after neighbor subtraction results in an improved fit. Each iteration of nei-sub fits the final PSF to an image from which all PSF-neighbor stars have been subtracted, which improves the fit, but those neighbor stars are subtracted using the inferior model (not the final one). Neighboring sources are again subtracted to achieve an improved model fit. Iterating neighbor subtraction increases the number of chances a bad PSF source has to be flagged and removed before the final model is fit. Typically only two iterations of neighbor-subtraction are performed before the chi value converges.

IV: ALLSTAR A chip's derived PSF models the dispersal of light for all sources detected in the chip, even though it is only fit with the best sources from the first application of SExtractor. After the model is created and adjusted, we use the DAOPHOT ALLSTAR routine to apply the PSF model to every source in the catalog and subtracted all from the frame. ALLSTAR uses a source's current best-guessed positions and magnitudes to fit the model and remove it, repeating this on the frame until each source has been completely removed. The remaining image, now with the signals from all detected sources subtracted from it, will be used for the next iteration of SE to detect sources that were missed because they were fainter or nearby a brighter object.

Multiple rounds of source detection with SE on each chip are now possible because of the newly included PSF-modeling and source subtraction. Sparse fields typically only require one more pass to detect all the chip's sources, but denser areas require up to 4 passes to identify a majority of measureable sources. The process of detecting and subtracting sources is repeated on each chip until the number of sources in the latest iteration is less than 25% of the number in the first, or when more than 50% of sources in the latest iteration exhibit S/N$\leq$5. Each iteration after the first is performed on the ALLSTAR-subtracted image produced with the most recent full catalog. Average source brightness decreases with each iteration, as the removal of the brightest sources reveals fainter ones. Changes to the source extraction method used for DR2 result in an improved extraction for exposures of dense areas, and the code now identifies more sources in each chip than code used for DR1 and DR2.

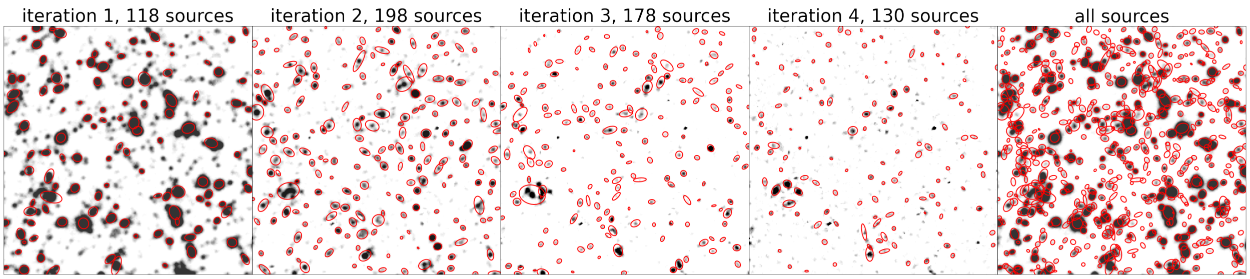

Figure 2.3 DR3 source detection on chip 20 of dense exposure `tu2670800` in the galactic bulge (RA=270.236° , Dec=-33.553°). The original application of Source Extractor (performed on DR1 and DR2) failed to identify several smaller, fainter sources in dense areas. New iterative source detection (four left panels) yields a larger final catalog for denser exposures (right panel).

V. Aperture Correction: Finally, a growth curve is calculated with DAOGROW. Two concentric apertures are applied to the PSF sources and increased in size to achieve a curve of measurements increasing in flux. The ratio of signal from the source and systemic, random, and background noise changes as the area enclosed between the two apertures moves away from the source's center, and the flux measured between them changes. Eventually as the apertures grow large enough, the growth curve of measurements levels out. The difference between concentric measuremnts is calculated from largest aperture to smallest, determines the median, then this aperture correction is applied to all sources to correct for the aformentioned sources of noise. See Stetson (1990) for more details on DAOGROW's function.

Once sources have been identified, the Source Extractor and ALLSTAR catalogs are combined, keeping sources that have information from both catalogs.

The need for iterative source measurement arises from the variety of source crowding in NSC exposures. Iterative source extraction can identify objects missed in DR1 and DR2, but takes a considerably longer time to do so, as exposures in dense areas can take up to a day and a half to process. Approximately 250,000 exposures have been measured to date. Measurement was being conducted on Montana State University's Tempest Research Cluster, and is being moved to the Texas Advanced Computing Center's servers.

Calibration

Calibration of NSC measurements is similar to the methods used for NSC DR1 and DR2, described in Nidever et al. (2021). Astrometric calibration will be conducted with Gaia DR3 coordinates. Photometric calibration is Gaia DR3 synthetic photometry was considered for use across the sky to achieve a uniform reference catalog.

Astrometry After exposures have been processed with the NOIRLab Community Pipeline, it is still necessary to make a small, aadditional adjustment to the coordinates measured in each chip. Astrometric calibration for very exposure in NSC DR3 is performed with coordinates from Gaia Early Data Release 3 (Gaia EDR3, Lindegren et al., 2021). The astrometry available for ∼1.46 billion sources in the EDR3 is the same catalog included in DR3 (Gaia Collaboration et al., 2021)), and are known to be extremely accurate. For each chip, Gaia sources are crossmatched to the most well-measured chip sources with a search radius of $0''.5$ to ensure the same object is being crossmatched between the two catalogs. These reference sources are used to determine corrections to α and δ for all sources in the chip.

Two steps are taken to achieve an even more accurate result. First, the measurements of each chip are projected from a 2D plane tangent to the celestial sphere, centered at the center of its corresponding exposure. This is necessary because of the slight difference between the physical coordinates of a source on the three-dimensional celestial sphere and the projection of the sphere onto a two-dimensional image, described in Chapter 1. Then, Gaia proper motions are used to precess the positions of the selected reference sources from their observation epoch to that of the chip. This accounts for the small offset that each source exhibits when observed at two different times.

Coordinates from data release 1 and 2 of the NSC were both calibrated with Gaia DR1 (Gaia Collaboration et al., 2016a) and Gaia DR2 (Gaia Collaboration et al., 2018a) astrometry, respectively. The process remains largely the same; scripts from DR1 and DR2 were adapted to calibrate using positions measured through PSF-modeling with DAOPHOT, rather than SExtractor positions.

Photometry Due to a lack in abundance of deep, all-sky catalogs with well-measured magnitudes in all seven of the DECam filters, photometric calibration of sources was previously performed with a combination of reference catalogs and model magnitudes. For $\delta \geq$-29°, Pan-STARRS $grizY$ photometry was used to calibrate the DECam $grizY$ bands. For the u, VR bands everywhere, and for $grizY$ below -29° declination, model magnitudes were created from other bands from a number of reference catalogs.

For each reference source without photometry in the necessary ugrizY,VR band, these models were constructed as linear combinations of measurements of the source in other available passbands, similar to the method used by Magnier et al. (2020) for "real-time" PS1 calibration (Nidever et al., 2018). All-sky catalogs 2MASS (Skrutskie et al., 2006), Gaia DR1 (Gaia Collaboration et al., 2016a), APASS (Henden et al., 2015), and GALEX (Bianchi et al., 2011), with Galactic reddening accounted for by Schlegel et al. (1998), SFD maps, were used to construct linear combinations of measurements that best approximated PS1 $grizY$ photometry for the DECAm $grizY$ filters, SMASH u band photometry (Nidever et al., 2017) for the DECam u filter, and Gaia G for the DECam VR band. Color cuts were determined by comparing residuals in vs color re A full description of model magnitudes is found in Nidever et al. (2018).

The necessity for a more uniform catalog to method of calibrate source magnitudes is prominent when considering the zero-point for NSC regions across the sky. The release of 220 mean, low-resolution BP/RP spectra of Gaia DR3 sources is accompanied by the ability to generate synthetic photometry for passbands between 330-1050 nm using the GaiaXPy[3] BP/RP spectra Python software package (Gaia Collaboration et al., 2023b).

We considered the use of Gaia synthetic photometry for calibration of NSC DR3 sources in order to achieve a uniform calibration method. Primarily, Gaia measurements are known to be very accurate, and cover the entire sky. Gaia coordinates are already used for astrometric calibration of sources, and a majority of NSC filters can be used to create synthetic photometry. Gaia Collaboration et al. (2023b) shows that standardized photometry in wide and narrow filters can produce results consistent with measurements.

On the other hand, Gaia does not provide full coverage for all NSC sources. Of the seven $ugrizY, VR$ bands represented in the catalog, only the $grizY, VR$ filters are within the defined wavelength range of BP/RP spectra (330-1050nm). The u band is defined from 312-400 nm and is only partially covered by the spectral data; Gaia Collaboration et al. (2023b) advises that Gaia synthetic photometry not be implemented for passbands outside of the required range. Similar UV bands have been standardized, for example, Gaia Collaboration et al. (2023b) described performance of the SDSS the Johnson-Kron-Cousins u bands, but both dispayed a much greater degree of scatter about the mean difference between the system and standardized synthetic photometry than the redder filters, in both magnitude and color. Use of Gaia synthetic photometry in the DECam u band, therefore, would have to be restricted to small ranges of color and magnitude to optimize results.

Additionally, many areas of the NSC do not have enough Gaia reference sources with mean spectra. Although over 200 million sources have mean spectra, they are dispersed throughout the entire sky and any one HEALPix, NSIDE=32 is typically not covered by more than 200 of these sources. If Gaia synthetic photometry is used to calibrate NSC magnitudes, it must be supplemented with either additional reference catalogs or with model magnitudes.

[3] `https://gaia-dpci.github.io/GaiaXPy-website/`

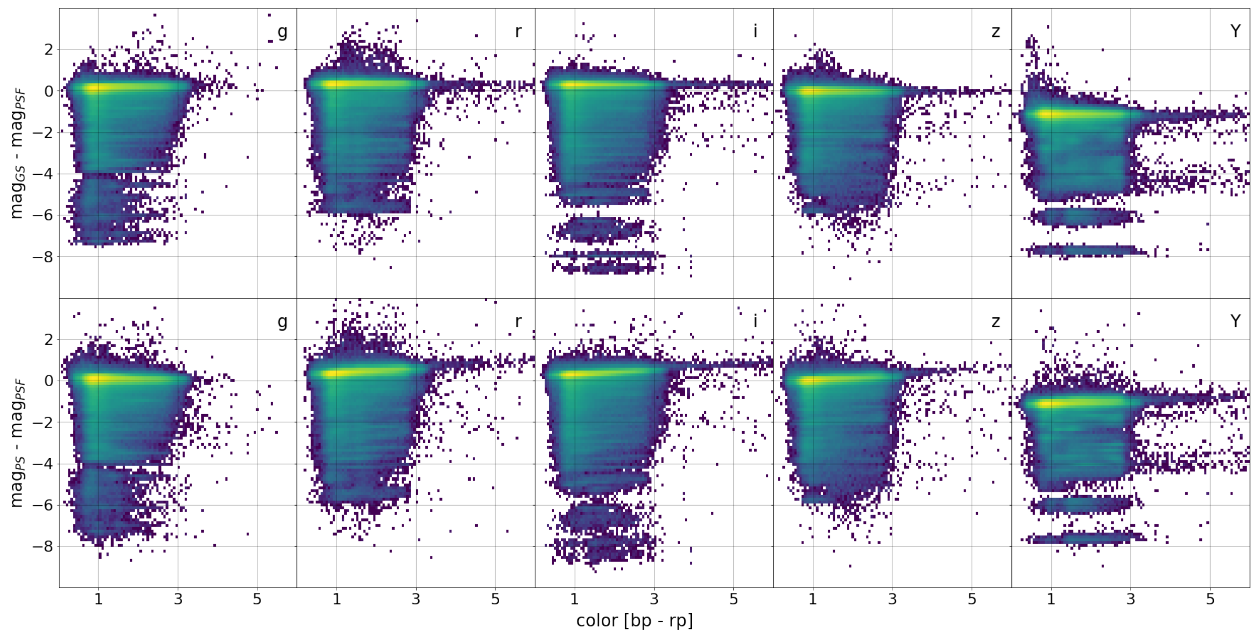

Figure 2.4 For Gaia synthetic photometry *(top row)* and Pan-STARRS photometry *(bottom row)*, the difference in magnitude between each respective catalog (mag_{GS} and mag_{PS}) and the observed PSF magnitude (mag_{PSF}) vs BP-RP color.

To evaluate the performance of synthetic photometry in DECam filters, calibration of exposures in the *grizY* bands was performed with both PS and Gaia synthetic photometry.

Zero-point terms differ across the sky - the difference in terms calculated for individual chips increases in crowded regions, likely due to extinction and the overlapping of sources in the galactic plane. The median is different for each filter, -0.051 for g, +0.089 for r, +0.084 for i, +0.092 for z, and +0.011 for Y. The decrease in zero-point for g, Y compared to r,i,z may indicate that the reddening effect is more apparent at the extreme ranges of the filter system where transmission curves show less efficiency.

Observed NSC magnitudes of sources were compared with the given magnitude from PS1 and their corresponding Gaia synthetic photometry in the *grizY* filters, for Gaia BP-RP color. Figure 2.4 shows both comparisons; a trend in color that changes for each filer is apparent in the difference between Pan-STARRS and observed magnitude, as well as significant dispersion in the bluer range of colors. The average offset in magnitude is also different for each filter; in both cases, magnitudes measured in the Y band have a greater difference between the reference catalog than the rest of the filters.

To investigate further, the difference in source magnitude between Pan-STARRS photometry to Gaia synthetic photometry is analyzed as a variable of BP-RP color. For each filter, a distinct trend of increasing difference in magnitudes for redder color is seen in Figure 2.5. The trend is again most apparent in the Y band, the reddest of the $grizY$ filters. Sources fall into at least two distinct trends for each filter. These are distinguished by separating sources by galactic latitude, as shown in the top two rows of Figure 2.5. This dichotomy is likely is an example of the issues the Gaia DR3 synthetic spectra encounter in areas of the sky with high extinction and high source density. If used, both a cut in color to bluer sources and a color adjustment to account for the trend of increasing error with reddness would have to be made to reference sources.

Future Work

It is clear that more consideration must be taken in order to determine the appropriate calibration method for NSC data. Although synthetic photometry is quite accurate, it suffers from extinction effects in the galactic midplane and from source crowding issues in dense areas.

Next steps include comparison of calibration with Gaia synthetic photometry and the SkyMapper Southern Sky Survey, which covers the southern hemisphere with the *ugriz* filters. Data release 4 of SkyMapper (Onken et al., 2024) is available this year and includes measurements of over 15 billion detections. Combined use of SkyMapper sources in the south and Pan-STARRS in the north may result in a more uniform zero-point for the catalog.

Once measurement and calibration are completed, sources will be combined into unique objects using the new software `yente`, written by collaborator Dan Caselden. `yente` can

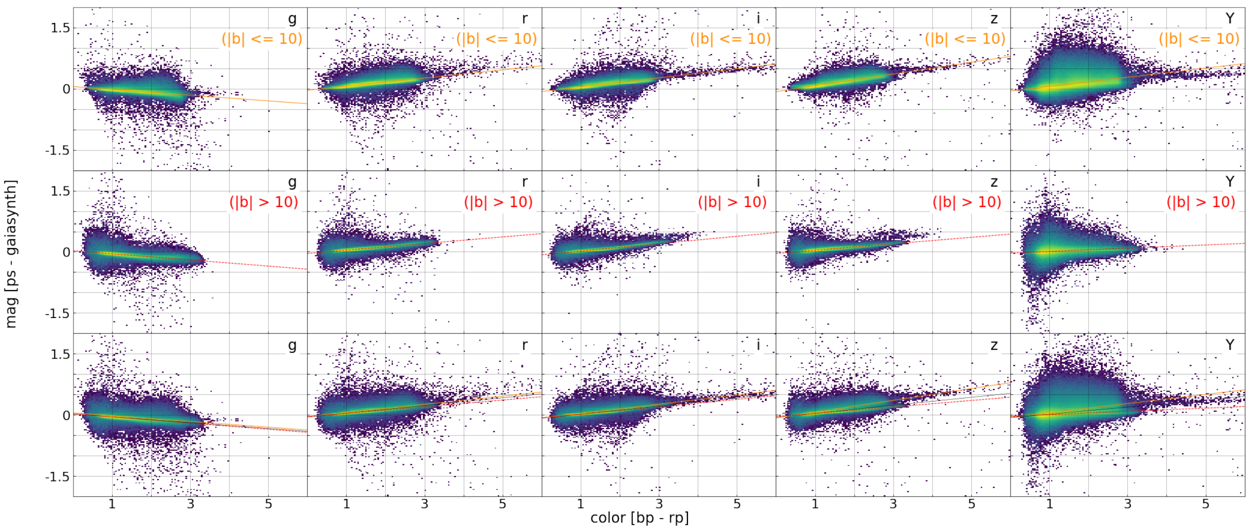

Figure 2.5 Comparison of Pan-STARRS photometry and Gaia synthetic photometry for the DECam *grizY* bands, from left to right, vs Gaia bp-rp color. The top row shows sources within 10° of the galactic plane at $b = 0$, the middle row shows all sources at least 10° away from the plane, and the bottom shows all sources. Extinction and crowding of sources in the galactic plane results in a greater offset in magnitude for redder objects in each band, more so than the offset seen for red objects away from the plane. The best-fit lines for the top two selections are plotted in orange and red, respectively, and each is shown in the final row. The difference between trends of in-plane vs. out-of-plane sources is greatest in the Y band

cluster measurements of objects with high proper motion, which was not previously available for the NSC outside of SSO detection (in the following two chapters). Both solar system objects and stars with high proper motion should be identified by this method.

An extra calibration step will be performed once the catalog has been completely measured and calibrated. Ubercalibration, developed by Padmanabhan et al. (2008) and similar to work done in Magnier et al. (2020) for Pan-STARRS, solves issues of problem of "relative" and "absolute" calibration. Padmanabhan et al. (2008) refers to relative calibration in regards achieving consistent photometric calibration over a survey or dataset, and to absolute calibration as the transformation of relative calibrations into physical fluxes. Ubercalibration addresses both by comparing calibrated magnitudes of detections of the same source and cross-calibrating sources against other sources in the catalog. Implementation of this method on the NSC will likely decrease photometric errors accross the sky.

EXPLORING THE SOLAR SYSTEM WITH THE NOIRLAB SOURCE CATALOG I: DETECTING OBJECTS WITH CANFIND

Contribution of Authors and Co-Authors

Manuscript in Chapter 3

Author: Katie M. Fasbender

Contributions: Lead author of paper, developed methods and software.

Author: David L. Nidever

Contributions: Second author of paper, project designer.

Manuscript Information

Katie M. Fasbender and David L. Nidever

Astrophysical Journal

Status of Manuscript:
____ Prepared for submission to a peer-reviewed journal
____ Officially submitted to a peer-reviewed journal
____ Accepted by a peer-reviewed journal
_X_ Published in a peer-reviewed journal

Institute of Physics Publishing
2020 December 17
2021 November 16
Volume 162, Article 244
10.3847/1538-3881/ac2230

Abstract

Despite extensive searches and the relative proximity of solar system objects (SSOs) to Earth, many remain undiscovered and there is still much to learn about their properties and interactions. This work is the first in a series dedicated to detecting and analyzing SSOs in the all-sky NOIRLab Source Catalog (NSC). We search the first data release of the NSC with CANFind, a Computationally Automated NSC tracklet Finder. NSC DR1 contains 34 billion measurements of 2.9 billion unique objects, which CANFind categorizes as belonging to "stationary" (distant stars, galaxies) or moving (SSOs) objects via an iterative clustering method. Detections of stationary bodies for proper motion $\mu \leq 2.5''\mathrm{hr}^{-1}(0.017\mathrm{d})$ are identified and analyzed separately. Remaining detections belonging to high-μ objects are clustered together over single nights to form "tracklets". Each tracklet contains detections of an individual moving object, and is validated based on spatial linearity and motion through time. Proper motions are then calculated and used to connect tracklets and other unassociated measurements over multiple nights by predicting their locations at common times, forming "tracks". This method extracted 527,055 tracklets from NSC DR1 in an area covering 29,971 square degrees of the sky. The data show distinct groups of objects with similar observed μ in ecliptic coordinates, namely Main Belt Asteroids, Jupiter Trojans, and Kuiper Belt Objects. Apparent magnitudes range from 10–25 mag in the $ugrizY$ and VR bands. Color-color diagrams show a bimodality of tracklets between primarily carbonaceous and siliceous groups, supporting prior studies.

Introduction

Although the sky has been extensively searched for solar system objects (SSOs) over the last few hundred years, new bodies are still being found today. Long before the first discovery of an asteroid (Ceres) at the Palermo Observatory in 1801 (Cunningham et al., 2009) until as recently as 1991, the process of identifying SSOs depended entirely on the human eye. Through the origin of astronomical surveys specifically intended for SSO detection, and later the addition of charge-coupled devices (CCDs) for astronomy purposes by the Spacewatch Telescope at the Steward Observatory (Gehrels, 1991), SSOs were spotted either by direct observation or by "blinking" between physical exposures of the sky in a lengthy process. This changed when Rabinowitz (1991) created the first automated method used for detecting Earth-approaching asteroids in near real time using the Spacewatch Telescope. With sequential exposures taken by the telescope, the detection software identified trails that moving objects (MOs) left in the first two exposures, and displacements between them and a third exposure. This new method of MO detection marked the beginning of a striking growth in the rate of asteroid discovery, and of our knowledge of the solar system.

SSOs fall into categories based on their orbital parameters and composition, called "groups" and "families". While groups have similar orbits, families are more closely related as they often consist of fragments from past collisions. Distinct to us by their high proper motion and perihelia $\leq 1.3\ AU$, Near Earth Objects (NEOs) are potential impactors due to their proximity. It wasn't until 2008 that the first detection of an asteroid before its impact was made by the Catalina Sky Survey (CSS, Boattini et al., 2009). Various organizations and warning systems like the Asteroid Terrestrial-impact Last Alert System (ATLAS, Tonry et al., 2018) are dedicated to the NEO search, as even a relatively small asteroid has the potential for mass destruction (Dearborn et al., 2020) and lasting effects on the Earth's environment (Koeberl and Ivanov, 2019; Marchi et al., 2019). To address the problem, in 1991 the Spaceguard Survey Network was established by NASA in response to direction from the United Stated Congress to increase the detection rate of asteroids which cross Earth's orbit (Morrison, 1992). Spaceguard has led to a significant increase in surveys dedicated to discovering NEOs, and in 2011 the NEO subset of the Wide-Field Infrared Survey Explorer (NEOWISE, Mainzer et al., 2011) reported the completion of the initiative to identify 90%

of NEOs greater than 1 km in diameter. The search expanded in 2005 when NASA was instructed to find 90% of NEOs with diameters greater than 140 m within 15 years, a time window which is closing. Despite CSS, NEOWISE, ATLAS, the Pan-STARRS Survey (Denneau et al., 2013) and further programs and surveys dedicated to reaching this goal, surprise impacts continue; the 2013 event in Chelyabinsk was caused by an undetected NEO with an estimated diameter of 20 m (Popova et al., 2013). This goes to show that blind spots still exist in our tracking methods and additional SSO exploration is, at the very least, beneficial.

Observational limitations also make it particularly difficult to detect many of the smaller subsets within the NEO population, including Atens (Earth-crossing orbit), Atiras (orbits within Earth's), Vatiras (orbits within Venus's), and Earth Trojans (co-orbiting with Earth). Due to their close proximity to the sun, members of these groups elude observation and it is estimated that only 5–7% of Atiras with absolute magnitudes less than 20 ($d \approx 300\ m$) have been found (Ye et al., 2020). The least studied groups are the Vatiras and the Earth trojans, as only one of each has been discovered as of 2020 (Connors et al., 2011; Greenstreet, 2020). Studies such as Markwardt et al. (2020)[1], which searched for Earth trojans using exposures from DECam, sometimes require confining the area included in their search in order to optimize the chances of detection. This and other surveys that constrain their fields to small sections of the sky to improve detection prospects, like those performed by Terai et al. (2013) and Ivezić et al. (2001), often do not allow for orbit determination as the observation arcs observed were too short to extrapolate.

Further out beyond the orbit of Mars, the Main Belt is filled with dozens of dynamic asteroid groups and families that can be constrained by searches through large catalogs (Lemaitre, 2005). Main Belt Asteroids (MBAs) observed by the Sloan Digital Sky Survey are shown to have a bimodality of carbonaceous and rocky siliceous objects (Ivezić et al., 2001),

[1]Data from Markwardt et al. (2020) are included in the NSC and were analyzed as a part of this study.

with size distributions estimated assuming consistent albedos throughout each population. MBA size and color can be relatively well-studied because of their abundance and our closeness, but contrasting results raise questions. The steepest estimated size distribution is a simple power law ~ 0.9 from the 2015 High cadence Transient Survey (HiTS) campaign (Peña et al., 2020), similar only to the results of Parker et al. (2008), who also use SDSS data. However, the 2014 HiTS campaign reported a slope of ~ 0.76 in the g band for brighter objects and ~ 0.28 for faint objects (Peña et al., 2020), which is closer to more common results like those found by Gladman et al. (2009). According to Peña et al. (2020), this is likely due to an interesting result described by Bhattacharya et al. (2010), who reported that objects at ecliptic latitudes $b \geq 5°$ observed by the Spitzer Space Telescope were 30% fainter than SSOs in the ecliptic plane (the 2015 HiTS campaign observed fields at a higher ecliptic latitude than the 2014 campaign). Additional SSOs must be observed to model a more accurate size distribution, and to provide more insight on its relation to ecliptic latitude.

At the far reaches of our Solar System, Trans-Neptunian Objects (TNOs) are distant enough (semimajor axis $a \gtrsim 30\ AU$) that they do not feel the effects of the main planets as much as objects in the inner Solar System. This means that they are particularly susceptible to external forces like galactic tides, passing stars, or perhaps even a distant unknown planet. These interactions with extrasolar forces provide insight into the dynamics, formation, and history of the Solar System. TNOs, which include Kuiper Belt Objects (KBOs) and Oort Cloud Objects (OCOs), are essentially remnants of the primordial Solar System, and studying their properties will provide stronger constraints on planet formation theories.

The potential presence of an unseen planet or mass has been explored by several authors after the discovery of Neptune and its perturbed orbit. Pluto's discovery in 1930 confirmed the existence of TNOs and alluded to the possibility of another larger object, dubbed "Planet X" by astronomer Percival Lowell. The most recent and promising hypothesis was established when Brown et al. (2004) discovered 90377Sedna (Sedna), the most distant SSO known at the time. Sedna has an unusually eccentric and inclined orbit, and one of the proposed causes of this is the gravitational scattering by an unseen planet.

This hypothesis was further developed when Trujillo and Sheppard (2014) discovered the second Sedna-like body, 2012 VP_{133}, orbiting at the very edge of the Kuiper belt using the Dark Energy Camera (DECam, Flaugher et al. 2015). They found that both Sedna and 2012 VP_{133} showed clustering in the argument of perihelion (ω), the angle between an inclined SSO's perihelion and the point where its orbital plane intersects with the ecliptic plane. The mechanism by which this clustering is thought to be achieved is referred to as "gravitational shepherding", which describes the effect of a large body on the orbits of nearby smaller bodies. As a small body passes by a larger one, the latter's nonzero net gravitational force on the former alters its trajectory and shifts its orbit. To this day, the gravitational shepherding due to a distant massive planet, often referred to as "Planet 9", remains by far the best explanation for the clustering seen in extra-TNOs.

Batygin and Brown (2016) added to this hypothesis by showing a clustering in not only ω of Kuiper Belt orbits, but a physical clustering of their perihelia as well. They also report that the orbits of known KBOs with semimajor axis $a \geq 227\,AU$ all approach perihelion within 94° of longitude of each other, and all lie in an orbital plane $\sim 22°$ from the ecliptic (Brown and Batygin, 2016). These numbers are supported by the recent discovery of 541132 Leleākūhonua (2015 TG387) by Sheppard et al. (2019). Two distinct groups of TNOs with similar ω have allowed astronomers to derive theoretical orbits of Planet 9.

Alternative explanations have been proposed and rejected; Khain et al. (2018) showed that the clustering may be due in part to the primordial state of the Solar System, but would not have produced an effect as substantial as the one observed. Brown (2017) effectively ruled out observational bias as the cause, estimating that the probability that the 10 KBOs known at the time with $a \geq 230\ AU$ were part of a larger population with uniform ω was 1.2%.

A later work (Brown and Batygin, 2019) reported a 0.02% probability that distant KBOs would be clustered as strongly as observed in both ω and in orbital pole position if the sole reason for this clustering was a detection bias.

Constraints on a mass and orbit for Planet 9 have changed over the years, from Hogg et al. (1991) placing a detectable limit on its mass of about 70 $M_{\oplus}$, to Batygin et al. (2019) more recently constricting it to ~5-10 $M_{\oplus}$ thanks to the greater number of known TNOs. Through a numerical simulation, Brown and Batygin (2016) suggested that the perihelion of Planet 9 would be between 150 and 350 AU, with an inclination within 30° of the ecliptic.

Studies of the Kuiper Belt and searches for TNOs have yielded small bodies and dwarf planets, but no body large enough to cause the observed clustering of TNOs has been found. Although the existence of Planet 9 itself remains unconfirmed, the discovery of additional TNOs through the work described in this paper could provide further evidence. Estimations of its parameters require a working knowledge of the most distant SSOs, hence the need to continue the search for them. Similarities between new and known objects may support the evidence of Planet 9 and contribute to estimations of its properties, while differences may lead to new hypotheses for unidentified forces acting on TNOs.

Two common obstacles that surveys face include limitations on the brightness of what can be detected (typical depth ≈ 19–24 mag, Denneau et al. 2013) and the area of the sky covered by observations. SSO-based surveys are often constrained to the ecliptic where the bulk of the solar system's mass is found, meaning more surveys and catalogs with more sky coverage must be searched to detect objects with high orbital inclinations to explore relationships such as the latitude–magnitude dependence shown by Peña et al. (2020) and Bhattacharya et al. (2010). Several wide-field surveys have been used to achieve this, such as CSS, the Near-Earth Asteroid Tracking program (NEAT; Pravdo et al., 1999), CCS, and the the Lincoln near-Earth asteroid program (LINEAR; Stokes et al., 2000), although both NEAT and LINEAR focus mainly on the northern celestial hemisphere due to the location of the telescopes used. The upcoming Legacy Survey of Space and Time (LSST; Ivezić et al., 2019) with the Rubin Observatory will extensively monitor the southern sky and is predicted to increase the known number of all small body populations by 10–100× (Jones et al., 2016), and is expected to be a significant detector of NEOs (Veres and Chesley, 2017). However, much of the northern sky will remain unmonitored at the faint magnitudes.

Independent endeavors to create detection algorithms that can be applied to any astronomical data, for example the NEARBY Platform (Stefanut et al., 2019), the Moving Object Processing System (MOPS) developed for Pan-STARRS, and other methods (e.g. Lieu et al. 2019, Perdelwitz et al. 2018, and Holman et al. 2018) have varying degrees of success and can typically be tuned to find specific families of SSOs with similar orbits. A recent example of this is THOR (Tracklet-less Heliocentric Orbit Recovery), an algorithm developed with detections from the Zwicky Transient Facility to extract SSO detections by applying test orbits to the data (Moeyens and Juric, 2019).

This work describes the background and implementation of the Computationally Automated NSC-tracklet Finder (CANFind), an approach designed to identify SSOs in photometric catalogs with individual-epoch measurements like the NOIRLab Source Catalog (NSC)[2]. The NSC is a crowd-sourced catalog covering 3/4 of the sky, with 34 billion observations, most regions are covered by at least 3 exposures. We test CANFind on the first data release of the NSC, and detect over 500,000 tracklets to magnitudes of 24 mag. 50,222 of these 500,000 tracklets have g-r, r-i color-color information showing a distinct bimodality of two general asteroid types (carbonaceous and silicious). 85.9% of tracklets were found within ±30° of the ecliptic plane, and 60% have more than three measurements.

The paper is organized as follows: Section 3 describes the first data release of the NOIRLab Source Catalog and its benefits for the use of SSO detection. CANFind is explained in Section 3, an overview of the detection efficiency simulation is in Section 3, the results

[2]Formerly known as the NOAO Source Catalog.

are discussed in Section 3, and future work to be done with NSC tracklets is described in Section 3. This introduces a set of planned publications all involving SSO detection in the NSC and subsequent investigation. Upcoming projects will connect tracklets with more spatially disperse measurements, fit NSC tracklets to SSO orbits, and analyze recovered SSO populations, morphology, comet activity, and streaked detections.

NOIRLab Source Catalog

This project uses the first data release of the NOIRLab Source Catalog (NSC, Nidever et al., 2018) to detect SSOs. The NSC is a crowd-sourced catalog using public data from the NOIRLab Science Archive processed in a uniform manner. The NSC has 34 billion individual observations of 2.9 billion distinct objects from 255,000 images spanning five years of observation from 2012–2017. Data come from DECam on CTIO-4m, KPNO-4m+Mosaic-3, and Bok-2.3m+90Prime from the DESI Legacy Survey (Dey et al., 2019). Table 3.1 lists several specifications from the instruments used by the surveys included in the catalog. The NSC contains a large amount of time series information that is useful for searches of moving objects and photometrically variable objects. Table 3.2 lists information from the 11 top-contributing surveys in DR1.

The NSC data are publicly available through the Astro Data Lab[3], and can by accessed via SQL queries. The catalog will be updated periodically, with the second data release containing over 68 billion measurements of 3.9 billion objects (Nidever et al., 2020). Figure 3.1 shows the object density *(left)* and exposure coverage *(right)* of NSC DR1. An overview of NSC DR1 can be found on the Astro Data Lab site[4], and a complete description is available in Nidever et al. (2018).

[3] `https://datalab.noirlab.edu`
[4] `https://datalab.noirlab.edu/nscdr1/index.php`

Table 3.1: Instrument specifications and coverage in NSC DR2

Instrument	Observatory	Coverage (MMYYYY)	N_{exp}	FOV (°)	CCDs	pixel spacing (″)	bands
DECam[5]	CTIO Blanco 4m	092012–112019	340952	3	62	0.26	*ugriz* *Y, VR*
Mosaic-3[6]	KPNO Mayall 4m	012016–082017	41561	3	4	0.26	*z*
90Prime[7]	Steward Bok 2.3m	112015–022019	29603	1	4	0.45	*g,r*

[5]Dark Energy Camera Dey et al. (2019); `http://www.ctio.noao.edu/noao/node/1033`
[6]Mosaic-3 Wide Field Imager Dey et al. (2016b); `https://www.noao.edu/kpno/mosaic/`
[7]Prime Focus CCD Mosiac Camera Zou et al. (2017)

Table 3.2: General information for the 11 top contributing surveys in NSC DR1, expanded from Nidever et al. (2018) Table 1.

Survey Name	Inst./ Imager	PI	N_{exp}	Bands	Depth *(mag)*	PSF FWHM ($''$)
DES[8]	Blanco/ DECam	Friedman	58546	grizY	24.5, 24.3, 23.5, 22.9, 21.7	1.2, 1.1, 1.0, 0.9, 0.9
Legacy Surveys:[9]						
DECaLS[10]	Blanco/ DECam	Schlegel & Dey	17533	grz	24.0, 23.5, 22.5	1.3, 1.2, 1.1
BASS[11]	Bok/ 90Prime	Zou & Fan	19741	gr	23.7, 23.1	1.6, 1.45
MzLS[12]	Mayall/ Mosaic-3	Dey	40224	z	22.6	1.01
NEO[13]	Blanco/ DECam	Allen	11800	VR	23.0	$\sim$1
DECaPS[14]	Blanco/ DECam	Finkbeiner	7590	grizY	23.7, 22.8, 22.2, 21.8, 21.0	$\sim$1
Bulge Surveys:						
BDBS[15]	Blanco/ DECam	Rich	3849	ugrizY	23.5, 23.8, 23.5, 23.1, 22.5, 21.8	$\sim$0.8–1.8
DSSGB[16]	...	Saha	3837	ugriz	...	...

[8]Dark Energy Survey (Dark Energy Survey Collaboration et al., 2016); `https://www.darkenergysurvey.org`.
[9]Dey et al. (2019); `http://legacysurvey.org`.
[10]DECam Legacy Survey; `http://legacysurvey.org/decamls/`.
[11]Beijing-Arizona Sky Survey (Zou et al., 2017).
[12]Mayall z-band Legacy Survey (Dey et al., 2016a).
[13]DECam Near Earth Object survey (Allen et al., 2016).
[14]DECam Plane Survey (Schlafly et al., 2018); `http://decaps.skymaps.info`.
[15]Blanco DECam Galactic Bulge Survey (Rich, 2015), (Johnson et al., 2020).
[16]Deep Synoptic Study of the Galactic Bulge.

Table 3.2: Continued.

Survey Name	Inst./ Imager	PI	N_{exp}	Bands	Depth *(mag)*	PSF FWHM ($''$)
Light Echoes[17]	Blanco/ DECam	Rest	7622	rVR	···	···
SMASH[18]	Blanco/ DECam	Nidever	6645	ugriz	23.9, 24.8, 24.5, 24.2, 23.5	1.2, 1.1, 1.0, 1.0, 0.9
BLISS[19]	Blanco/ DECam	Soares-Santos	3049	griz	···	···
NSC DR1	···	Nidever	255,454	ugrizYVR	23.1, 23.3, 23.2, 22.9, 22.2, 21.0, 23.1	1.4, 1.3, 1.2, 1.0, 1.0, 1.0, 1.2

[17] Light Echoes of Galactic Explosions (Rest et al., 2015).

[18] Survey of the Magellanic Stellar History (Nidever et al., 2017); `http://datalab.noao.edu/smash/smash.php`.

[19] Blanco Imaging of the Southern Sky.

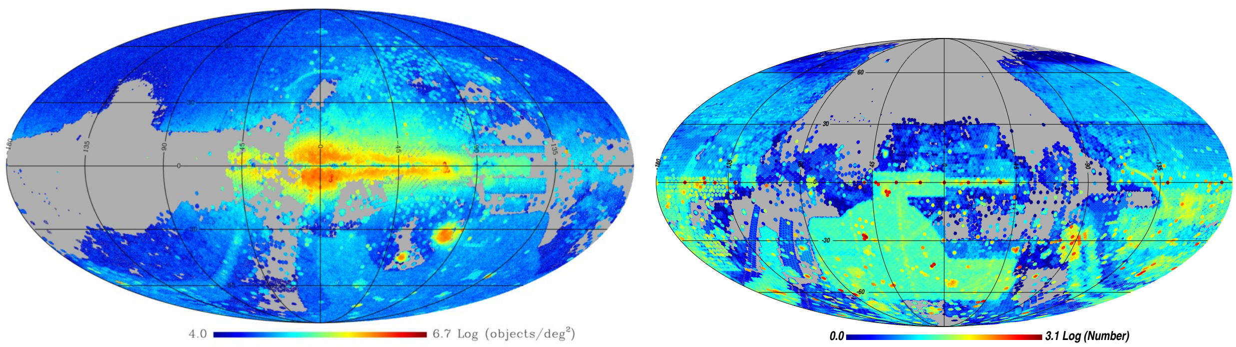

Figure 3.1 *(Left)* Density plot (number of objects per square degree) of the objects in NSC DR1 (Nidever et al., 2018) in galactic coordinates. 3/4 of the sky is covered, primarily the southern celestial hemisphere. *(Right)* Number of exposures overlapping any piece of sky in NSC DR1, on a logarithmic scale and in equatorial coordinates. Most areas have tens of exposures while some have thousands.

From the NSC DR1 exposures table, the average exposure time is 96.28 s, with a minimum of 0.01 s and a maximum of 1300 s. Figure 3.2 shows the number density for the full range of exposure times, broken down by instrument. As described in Section 3, the NSC is only searched for SSOs in areas covered by at least 3 exposures; the difference between the total exposure list and the searched exposure list is also shown in Fig. 3.2. All exposures are run through the NOIRLab Community Pipeline. Flaugher et al. (2015) report a shutter accuracy of $\leq$1ms for DECam, which provides both the largest sample of exposures and the widest range of exposure times. Images with long exposure times may contain detections of faint TNOs detected as point sources as well as streaking from SSOs exhibiting higher proper motion; for an exposure time of 1300 seconds, an object moving μ=20$''$relative to the background would leave a $\backsim$7.2$''$trail, within the $\backsim$1080$''$range of a typical single DECam CCD (2048x4096 pixels with pixel scale 0.26).

The NSC measurements table (`nsc_dr1.meas`) provides the main souce of data for this work. Each source-extracted measurement is represented as a row of data in the table,

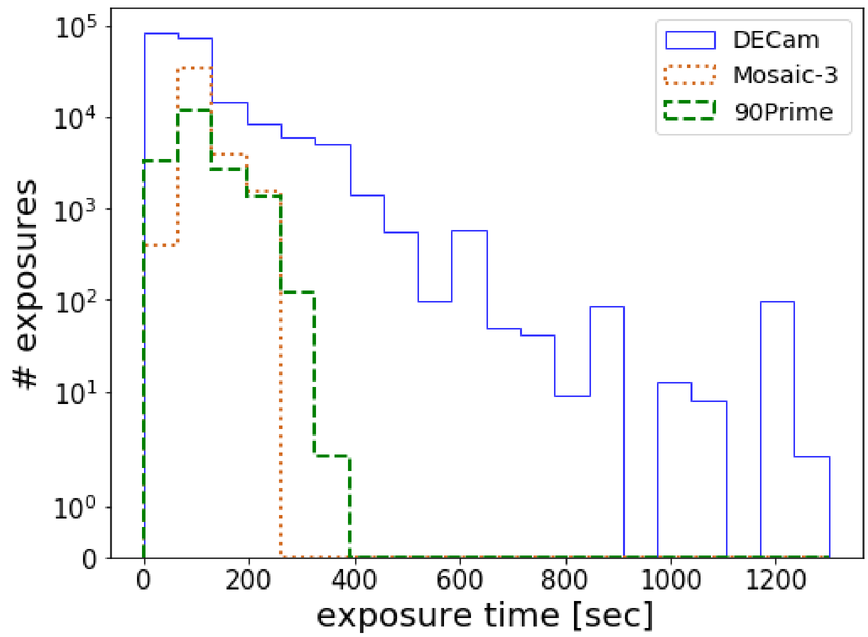

Figure 3.2 Histogram of exposure times for all exposures in the NSC.

with a total of 34,658,213,888 rows. 31 columns of detection parameters include position and positional uncertainty (`RA, Dec`), exposure filter, apparent magnitude (`mag_auto`), photometry information, and the observation Modified Julian Date (`MJD`). An overview of all columns of the measurements table table is also available at Astro Data Lab[20].

Use of the NSC may provide solutions to some of the limitations common to SSO searches described in the previous section. One issue is the potential for observational bias in the regions covered. The focus of surveys is often away from the galactic plane, due to the higher density of objects in that area polluting the recovered SSO population. NSC DR1 covers 3/4 of the sky and approximately half of the galactic plane is included in the observed region, meaning this project searches portions of the sky that are under-examined for SSOs.

A drawback of the NSC is that exposures of the most dense areas are often oversaturated, resulting in a lack of distinction between real sources and image artifacts, and

[20] `https://datalab.noirlab.edu/query.php?name=nsc_dr1.meas`

therefore a higher rate of false positives in SSO searches near the galactic plane ($\delta \leq 15°$) and the Magellanic Clouds (5° around LMC and 3° around SMC). The NOIRLab Community Pipeline used in the NSC calibration process masks saturated stars and their bleed trails, however some effects from bright saturated star still get through including scattered light in the periphery. These generally do not line up in any preferred direction, and their effect must be accounted for in the validation of any tracklets found in the NSC.

The limiting magnitude of a survey is also very important: distant SSOs are quite faint and will be undetectable to most telescopes during the bulk of their orbits due to low albedo or large distance. The depth of most NSC exposures is approximately 23rd mag, an adequate value for detecting TNOs whose magnitudes are typically fainter than 20th mag. The NSC also contains multi-band information that provide colors of objects and will shed further light on their properties. In a study of the colors of almost 100 TNOs, Schwamb et al. (2019) found two taxonomic groups, and the NSC should contain measurements of enough TNOs for a similar investigation (see Sec. 3).

Any newly discovered objects may also clarify the size distribution of solar system bodies. For instance, Sheppard and Trujillo (2010) showed a lack of discovered intermediate and small Neptune Trojans. Missing objects may be uncovered in the NSC after orbit determination, or may otherwise support these missing Trojans. By investigating the range of asteroid sizes, new parameters can be established regarding the accretion and formation history of the solar system.

Finally, the NSC covers much of the southern celestial hemisphere, which has been largely under-searched in SSO surveys. Five years of observations indicates the likelihood of orbiting bodies appearing in the NSC multiple times. An issue is the intermittent observational pattern; certain areas of the NSC have insufficient exposure coverage for SSO detection, as the contributing surveys were designed for various purposes. At least three exposures of a field are required to detect tracklets as defined in this work. Section 3 describes the selection of areas with adequate NSC coverage.

Because of these reasons, the deep, multi-band, time-series NSC information will allow this work to markedly improve the census of solar system bodies and help our understanding of planet formation. Detections of Planet 9 may be hiding in the NSC, and, at the very least, any KBOs found in the catalog will provide further investigation into its proposed existence.

Moving Object Detection Method

Here we describe the CANFind method used to detect SSO moving objects in the NSC catalog. The source code is written in Python and uses the `scikit-learn`[21] (Pedregosa et al., 2011) machine learning package. CANFind relies on two `scikit-learn` algorithms: the Density-Based Spatial Clustering of Applications with Noise (DBSCAN; Ester et al., 1996b) and RANdom SAmple Consensus (RANSAC; Fischler and Bolles, 1981), a linear regressor that is robust to outliers. Beginning with the NSC `meas` table of individual exposure measurements, the main steps are:

1. Initial spatial clustering with DBSCAN (eps = $0.5''$) to detect and remove stationary objects and initial detection of moving objects with moderate angular velocities.

2. Second spatial clustering with DBSCAN (eps = $11''$) to identify detections of SSOs which form tracklets.

3. Validation of tracklets obtained in steps 1 & 2 using robust linear regression (RANSAC) and the Pearson Correlation Coefficient (PCC). Proper motions of valid tracklets are measured.

4. Track formation and validation by linking tracklets and unclustered measurements by using proper motion to predict object position at common epochs.

[21] `https://scikit-learn.org/`

A flowchart outlining the process described in this section can be seen in Fig. 3.3.

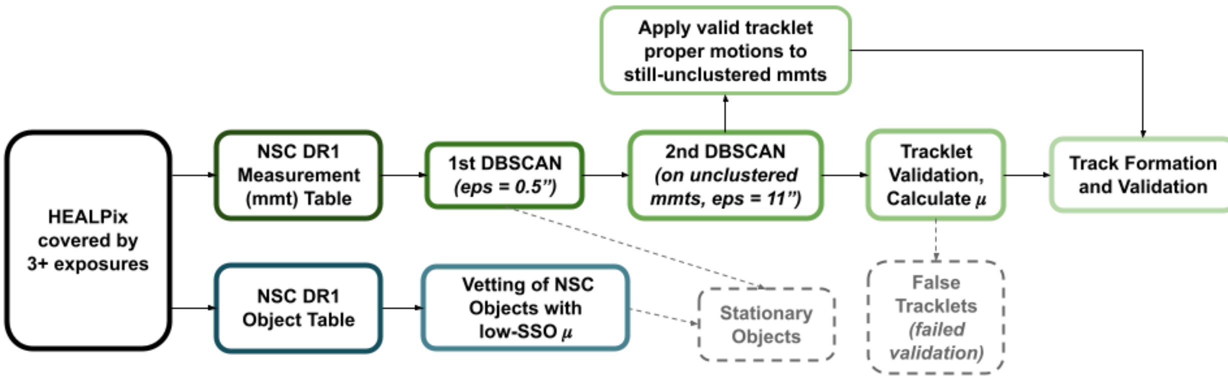

Figure 3.3 CANFind flowchart, beginning with HEALPix covered by 3+ exposures *(left)*. The top row follows the main CANFind process from the NSC Measurement Table to Track Formation & Vaidation. The bottom row indicates the NSC objects that were analyzed as potential SSOs, referred to as "Vetting NSC Objects".

Spatial Clustering with DBSCAN on Hyalite

DBSCAN is used in an iterative process to assign measurements to unique objects, both stationary and moving. DBSCAN clusters data in areas of high density, and was developed in order to categorize the objects of a database into relevant groups.

This particular algorithm was selected for a number of reasons, the most important being that minimal knowledge of the data set is required to establish the two DBSCAN input parameters set for this project; the eps-neighborhood (`eps`) of a point, which is the maximum distance between two points for one to be considered as in the neighborhood of the other, and $\texttt{n}_{points}$, the minimum number of points required to define a cluster. In the case of this work, DBSCAN is applied to measurements using only the information of spatial location, and `eps` and $\texttt{n}_{points}$ are determined based on the type of object being clustered. DBSCAN also does not require a set number of priors, which is advantageous as there is no way of knowing how many objects, stationary or otherwise, will be in any area of the sky. One caveat is that DBSCAN does not take into account the positional uncertainties of measurements; they are, however, included in the calculation of tracklet proper motion.

The second reason for the selection of DBSCAN is its ability to identify clusters with arbitrary shape. This allows one clustering method to be applied to all types of objects in the NSC identified in this work. It can cluster the measurements of both stationary objects (SOs), which lie in close proximity to each other in a roughly spherical pattern, as well as the more linearly-distributed measurements of moving objects. As DBSCAN is only used to connect intra-night detections, more complex SSO motion can be ignored for the extent of its use. Furthermore, the capability of DBSCAN to identify outlier points is essential to the method of application, as described in the following sections. Some of `scikit-learn`'s other clustering algorithms offer this feature; for example the Variational Bayesian Gaussian Mixture Model (VBGMM) was also considered as it can identify clusters with both strong and weak linear correlations. Ultimately, the number of necessary parameters and the slow computation speeds (this algorithm is not good for very large datasets) eliminated VBGMM in favor of DBSCAN.

Lastly, DBSCAN is very efficient for large databases with significantly more than several thousand objects (Ester et al., 1996b). As we analyze billions of measurements, it is essential that CANFind is as efficient as possible to maintain reasonable computation times. This is aided by Montana State University's Hyalite computer cluster, enabling the application of these methods on the vast extent of the NSC through a parallelized framework. Hyalite has 1,300 cores and 77 computing nodes with either 64 or 256 GB of RAM. By running CANFind on the Hyalite cluster, many areas of the sky can be searched simultaneously and the computation time is dramatically reduced.

We take advantage of the NSC coming pre-divided into HEALPix[22] (sections of equal area, Górski et al., 2005) with NSIDE=265 indexed in the `ring265` column of the object

[22]`https://HEALPix.jpl.nasa.gov/`

table, and query 4 neighboring HEALPix at a time to combine them into an area that takes CANFind an average of 5 seconds to analyze, depending on the number of sources and measurements present in the field. The resulting combined HEALPix, with NSIDE=128 for a resolution of approximately 0.5°, is run through the CANFind process with several of its neighboring HEALPix as a job on Hyalite's `slurm` queue. Although Hyalite allows several HEALPix to be processed simultaneously, computation speed is hampered slightly by PostgreSQL query limitations. Fewer HEALPix can be analyzed per job in fields with high object density, as this increases the query processing time and slows down the job's progression. Additionally, jobs had to be submitted in incremental batches as the database can only handle a limited amount of queries at a time. Depending on the field density, 1–10 jobs were submitted every 10–60 minutes for 1–5 HEALPix per job. Using roughly 10 nodes at a time with 32 or 40 CPU/node, the NSC took approximately one week to analyze on Hyalite.

The rest of this section describes how DBSCAN is used to assign NSC measurements to unique objects, visualized Figure 3.4. The first iteration of DBSCAN identifies and removes stationary objects moving less than $2.5''\text{hr}^{-1}(0.017°\text{day}^{-1})$ for a separate vetting process, leaving remaining measurements to be clustered into distinct moving objects during the second iteration. These data will be fit to solar system orbits to create object candidates, and the properties of these candidates will be derived and analyzed.

<u>Selecting Areas of the Kky for Initial Tracklet Search</u>

The NSC has a very high object density within the Galactic plane of the Milky Way. Exposures from the galactic plane also contain a high number of very bright and saturated stars which can cause various artifacts in the source catalog. Because these artifacts heavily impair the performance of the DBSCAN detection method, fewer objects are expected to be extracted within ±15° of the galactic plane. This is exacerbated by the high density of background objects in both the galactic plane and the Magellanic Clouds, as crowding hampers the ability of DBSCAN to differentiate unique sources. A sample of tracklets extracted from these areas by CANFind is examined in finer detail in Section 3.

We used the HEALPix scheme with nside=128 to break up the sky into smaller chunks to be analyzed separately. For the initial search, only areas of sky with adequate cadence to capture sequential displacements of the faster-moving SSOs were used. The selection criteria was that the HEALPix must have coverage from at least three or more exposures taken within roughly 20 minutes of each other. This reduced the 153,472 HEALPix covered by the NSC to 132,884 to be studied with CANFind.

Vetting NSC Objects

Because some SSOs have proper motions low enough to be represented in the NSC object table, we run an additional test on all NSC objects with at least 3 detections and a recorded NSC proper motion above $0.0041''\text{hr}^{-1}$($2.7\text{e-}5°\text{day}^{-1}$). This value corresponds to the average proper motion of 2015 TG387, a TNO with the second-largest semimajor axis known to date (1085 AU) and an orbit stable over the history of the solar system (Sheppard et al., 2019).

Every object above the minimum proper motion is analyzed to estimate the likelihood that it is an SSO. With a set residual threshold of 0.001°, RANSAC is applied to the spacial and temporal object data to remove galaxies with several NSC detections over multiple years. The `curve_fit` function from `scipy.optimize` is applied to the measurements of each object to calculate proper motion in RA and Dec [$''\text{hr}^{-1}$].

A signal to noise cut of S/N$\geq$4 was made on net proper motion in order to reduce the contamination of stars and galaxies among true detections of SSOs. To further reduce this contamination, a cut on the reduced chi squared value was made, keeping all objects with $\chi^2_\nu \leq 1.5$. Despite quality cuts, it is expected that a greater number of false tracklets are present in the 2095 objects that passed this validation step. Nonetheless, they are considered to be tracks or tracklets, and therefore will be tested as SSO candidates with the rest of the tracklets detected by CANFind.

Stationary Object Identification

DBSCAN is first used to identify measurements belonging to slow-moving or stationary objects using a relatively small `eps` $= 0.5''$and $\texttt{n}_{points} = 2$. The `eps` value was selected to reflect the original object identification of the NSC. The NSC `object` table was created by associating points within $0.5''$of each other, but this did not account for the faster proper motion (μ) of most SSOs. For this reason, only the NSC measurement table was used for this step. Panels *a* and *b* of Figure 3.4 demonstrate the application of DBSCAN on 2,928 measurements from the NSC in HEALPix pixel 124958 positioned a few degrees from the ecliptic plane, forming 48 clusters (SOs) and leaving 38 outliers. The proper motions of many of these objects are already given by the NSC catalog and were referenced in the analysis for objects exhibiting Solar System-like motions. The DBSCAN outliers are retained to be assigned to faster-moving objects in the next step. Because the source-extracted measurements of resolved galaxies may be more than $0.5''$apart, nearby galaxies are often not identified in this first step, and must be removed later during the validation process.

Identifying Tracklets and Tracks

The identification of tracklets and tracks is performed in three steps:

Linking Measurements into Tracklets: Once measurements of SOs are identified and removed, the remaining measurements are assigned to unique moving objects by the second iteration of DBSCAN. When closely-spaced exposures (∼20 minutes apart in this example) are analyzed, measurements of fast moving objects form spatially linear structures called "tracklets". Because these measurements are farther apart from each other than those belonging to SOs, a new `eps` of $11''$is used, as seen in panel *d* of Figure 3.4. Each DBSCAN

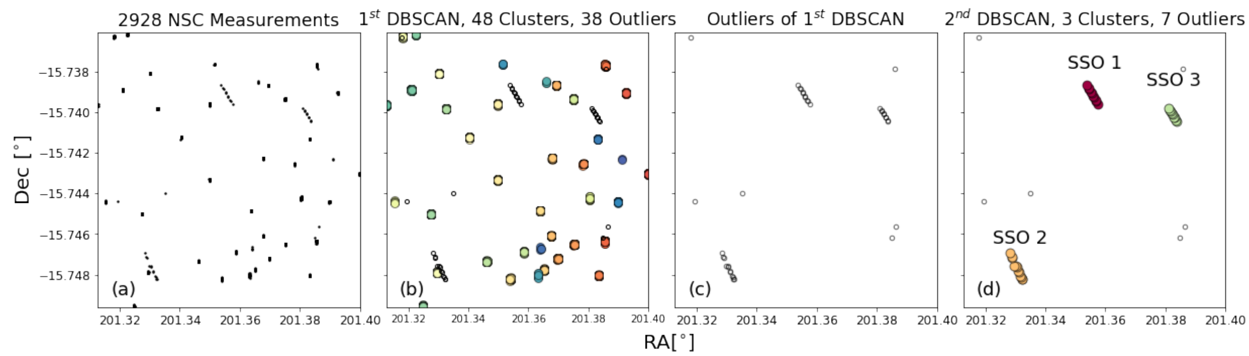

Figure 3.4 An example spatial map of NSC measurements showing clear detections of three Solar System Objects (SSO). The SSOs move rapidly ($\sim 40'' \mathrm{hr}^{-1}$or $0.27° \mathrm{day}^{-1}$) and show a "tracklet" while background objects keep a fixed position (*panel a*). Measurements belonging to fixed objects are clustered (*panel b*) and removed, leaving behind outlier measurements (*panel c*) to be assigned to moving objects. A second iteration of clustering identifies the SSO tracklets (*panel d*).

cluster must now contain $\mathtt{n}_{points} \geq 3$ detections, according to our definition of a tracklet as a collection of at least three displaced detections of a unique object. Therefore, each cluster is a tracklet that may represent the detections of an SSO, and are referred to as *"CANFind tracklets"*.

Tracklet Validation: Each clustered tracklet undergoes a validation process to ensure that its measurements are consistently linear in space and time, and to eliminate any falsely clustered data. Some nearby, spatially-resolved galaxies with a roughly linear distribution of measurements are mistakenly clustered as tracklets in this step, as DBSCAN often fails to identify them as stationary objects if that distribution is too large. However, they are easily identified through examination of their temporal information. In the creation of the NSC, multiple source detections from a single galaxy were sometimes extracted from one exposure, so resulting DBSCAN clusters do not produce a realistic trajectory for an SSO.

To test each tracklet, its measurements are analyzed using RANSAC on both the spatial coordinates and the tracklet's normalized (*position,time*) information. Any outlier found by RANSAC is likely an incorrectly clustered measurement, and is eliminated from the

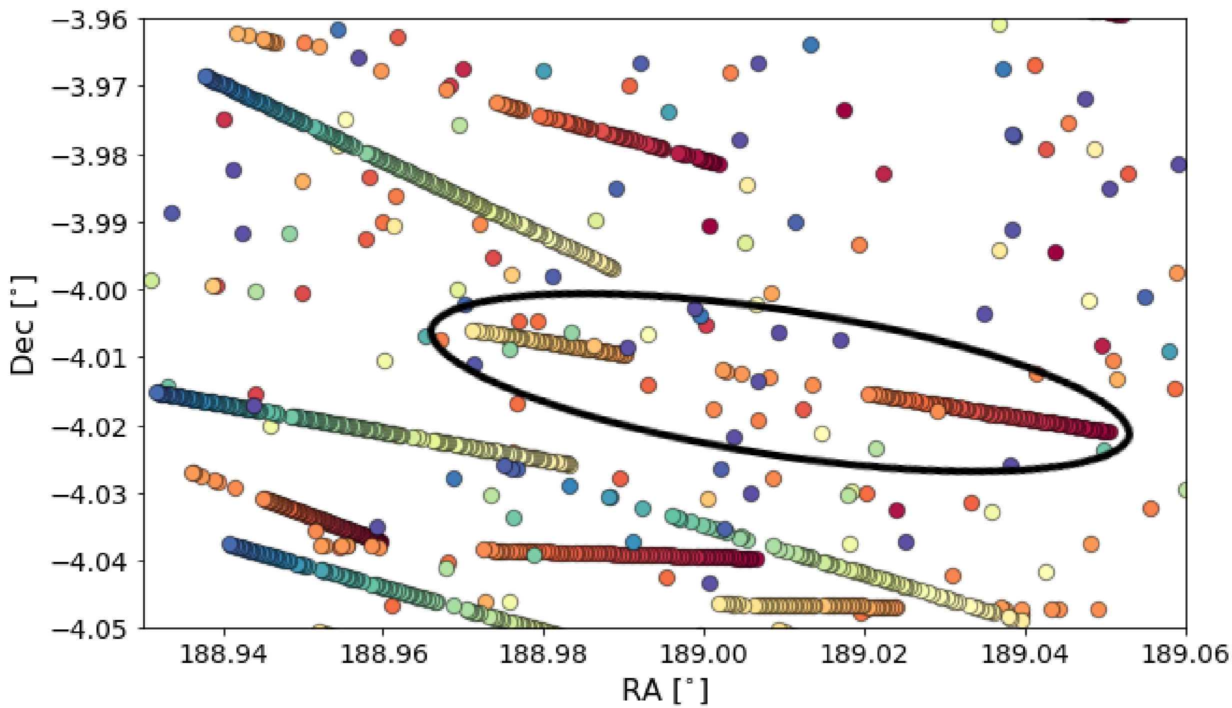

Figure 3.5 An example of track formation, with color as time of observation (over two nights, MJD=56746-56747). The two circled tracklets, along with various unclustered measurements between them, are linked together to form a track using the position prediction method described in subsection 3.

tracklet. As an additional step, the Pearson Correlation Coefficient (PCC) is calculated for each tracklet. The assumption that a true tracklet has measurements that fall into a straight line motivates the PCC cutoff value of $\geq |0.9|$ used by CANFind. If the spread of tracklet measurements is too large, then the cluster likely only contains measurements of a galaxy, not an SSO. This validation process disposes of many erroneous tracklets, making the next step of linking tracklets together a less computationally expensive process.

Linking Measurements and Tracklets into Tracks: Track formation in CANFind is meant to associate tracklets with both other tracklets and unclustered measurements left from the previous clustering steps. After a tracklet is verified, the slope values determined by RANSAC are saved as the proper motion in RA and Dec [$^\circ$day^{-1}]. Using these values, a position-prediction method is applied to the tracklets and remaining unclustered measurements within the HEALPix, allowing them to be connected into longer "tracks", which consist of at least two tracklets and typically contain detections from multiple nights. As the assumption of linear motion starts to fail for trajectories spanning so much time, the track validation step is less restrictive than tracklet validation; that is to say, the positional uncertainty allowed for predicted positions of tracklet measurements is large (0.005°) compared to measurement uncertainty to account for the deviation from linearity that SSOs display over multiple nights.

The proper motion of a tracklet is used to project its position to the observation time of other tracklets and unclustered measurements. This is done twice - first, the calculated proper motion of a single tracklet is applied to all other tracklets and unclustered measurements in the healpix, and all points are moved to the location they would hypothetically be at a common time. If the positions coincide within a few times their measurement uncertainties, then the tracklets and unassigned measurements are linked together into tracks. This is repeated for every tracklet in the healpix. A second "projection" process is applied for comparison, this time with each tracklet moving at its own calculated velocity to a common epoch. An example of track formation is shown in Figure 3.5.

To demonstrate the typical distribution of tracklets within the ecliptic plane, Figure 3.6 roughly covers the area of one DECam field, with color as detection time.

Efficiency Simulations

To test the efficiency and completeness of CANFind and the NSC Object Vetting process to detect moving objects, a simulation was created that generated synthetic tracklets with linear trajectories and a range of proper motions that are characteristic of SSOs. These tracklets had between 3 and 10 measurements, and the average tracklet cadence was between 20 minutes (CANFind) up to several hours (NSC Object Vetting). Measurements were

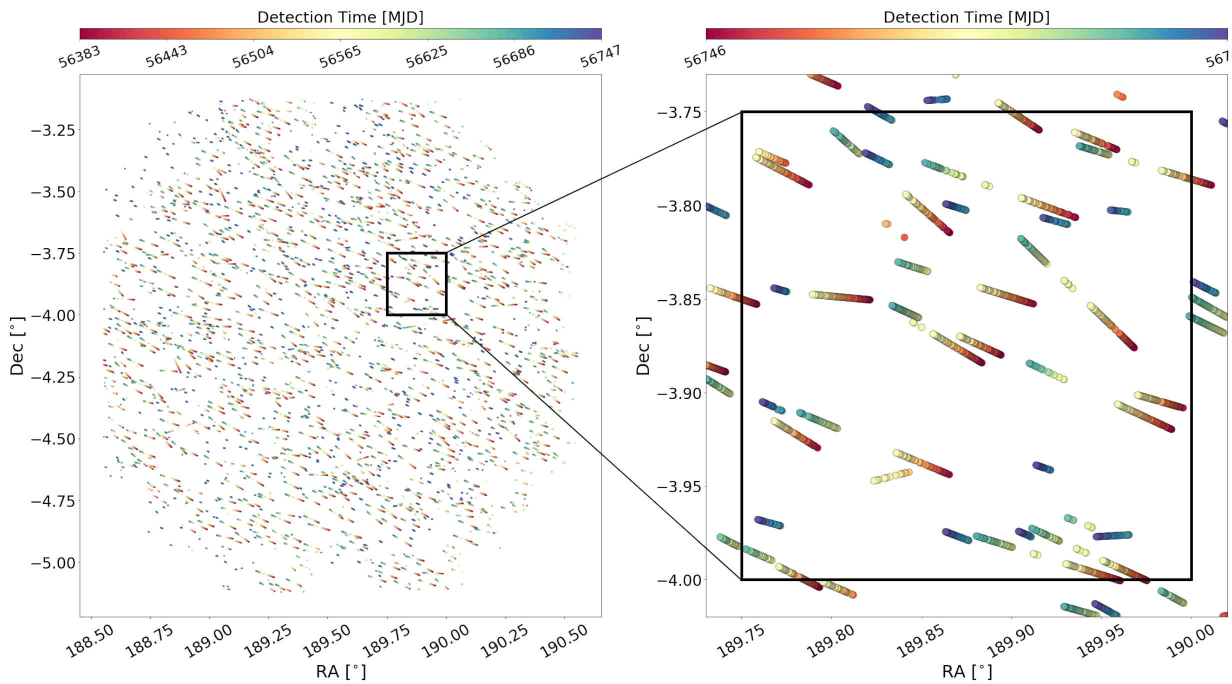

Figure 3.6 2,941 tracklets, color-coded by measurement detection time, in one DECam field in the ecliptic plane. Field depth goes to 25.7 mag.

given equatorial coordinates, an observation date, and a magnitude between 14–25 with an uncertainty (`magerr_auto`) that was then used to calculate the positional error in (RA,Dec). These generated tracklets were separately added to un-analyzed NSC measurements from a HEALPix (nside=128) in a field of average object density.

The first set of tests varied the range of input tracklet proper motion with the goal of determining biases set by CANFind's use of DBSCAN. Simulations of 100,000 tracklets each were run for different ranges of μ to explore the upper and lower limits of CANFind's range. Results for $0 \leq \mu \leq 100''\text{hr}^{-1}(0.67°\text{day}^{-1})$, $0 \leq \mu \leq 15''\text{hr}^{-1}(0.1°\text{day}^{-1})$, and $0 \leq \mu \leq 8''\text{hr}^{-1}(0.053°\text{day}^{-1})$ are shown in Figure 3.7.

The performance of CANFind for a range of magnitude uncertainties was explored in a second set of tests using an average FWHM value = 1.18 from the NSC exposure table. The range of `magerr_auto` was sampled from several areas including the galactic plane, ecliptic

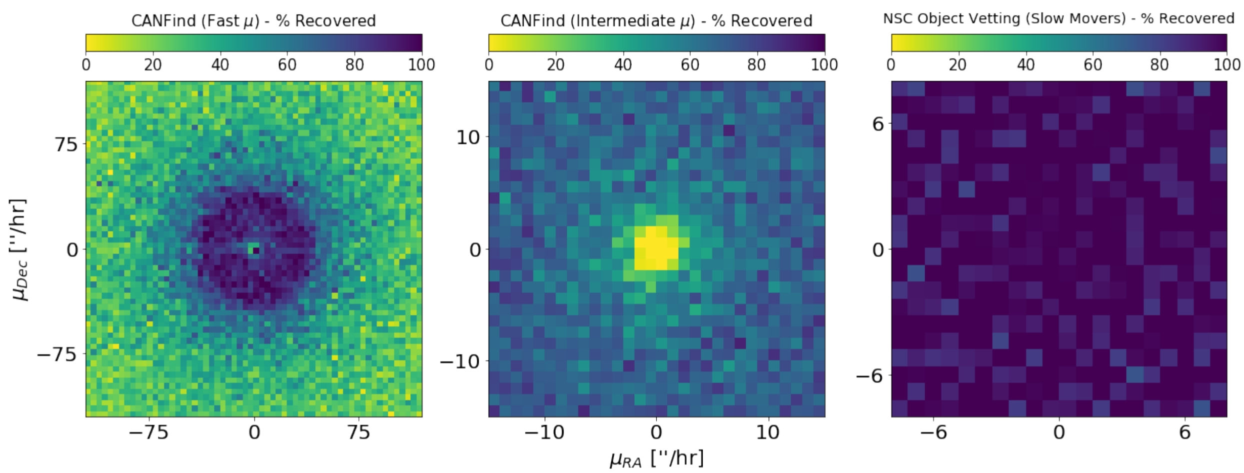

Figure 3.7 Density plots from the simulation showing 3 general ranges of tracklet proper motion μ [$''\mathrm{hr}^{-1}$]. CANFind results show the algorithm's upper *(left)* and lower *(center)* limits set by the parameters used for DBSCAN. CANFind leaves a gap around μ=0 of about 2.5$''\mathrm{hr}^{-1}$(0.017°day^{-1}) in radius, which is filled in by the NSC object vetting process *(right)* described in Sec 3.

plane, and in a field away from both planes. Between simulations of 100,000 tracklets each for three ranges of magnitude uncertainties (0.0002–0.002 mag, 0.002–0.02 mag, and 0.02–0.2 mag) CANFind's detection efficiency only changed slightly (97.6%, 97.2%, and 95.5% for the three ranges, respectively).

In addition to the 600,000 tracklets tested over varying μ and `magerr_auto`, a cumulative 200,000 tracklet test over full proper motion and uncertainty ranges found that CANFind recovered 96.5% of synthetic tracklets with average measurement spacing (Δs) between 0.5–10.9$''$for proper motions less than 1.4°day^{-1}(209$''\mathrm{hr}^{-1}$) to within 1$''\mathrm{hr}^{-1}$of their input proper motion. The limits of CANFind are a result of the parameters used in both instances of DBSCAN. The first iteration (`eps`=0.5$''$) to dispose of stationary objects sets the lower limit, (center panel of Fig 3.7), and the upper limit (left panel of Fig. 3.7) is set by the second iteration (`eps`=11$''$). As a result, this search optimizes CANFind to detect tracklets with cadences between 0.5–11$''$(0.00012–0.003°).

CANFind's false positive rate was also tested in fields of varying object density. Fake, linear sky-plane tracklets were created with measurements spanning one night or less, and given random, realistic positional uncertainties and observation times. One set of 1000,000 synthetic "fake" tracklets was analyzed in a HEALPix 5° above the galactic plane (35,993 objects, 159,191 exposures) and in a HEALPix 6° above the ecliptic (7,990 objects, 248,004 measurements). The fake tracklets, like the "true" tracklets created for previous simulations, consisted of 3 to 10 measurements spaced less than 0.003° (10.8″) from each other. In both fields, 3% of fake tracklets were falsely recovered by CANFind.

Finally, the efficiency of the track linking process was tested at a range of velocities between $0 \leq \mu \leq 60''\text{hr}^{-1}(0.4^\circ\text{day}^{-1})$. 100,000 tracks were created for this test by extending a synthetic tracklet beyond the timeframe of one night, either creating a new tracklet or adding unlinked "detections" of the object "observed" at a later time. Track measurements were given the same information given in tracklet simulations, and all complete tracklets created to form tracks were correctly recovered by CANFind. 80% of the synthetic tracks were completely identified by CANFind.

Results

The CANFind search for SSOs yielded 527,055 tracklets in 35,710 HEALPix of nside=128 covering 29,971 square degrees of the sky. The density of tracklets in ecliptic proper motion can be seen in Figure 3.8. The 2,094 tracklets detected by the NSC object vetting process fill the range between $0 \leq \mu \leq 2.5''\text{hr}^{-1}(0.017^\circ\text{day}^{-1})$ left by CANFind (Figure 3.9). The distribution of tracklets in ecliptic coordinates is shown in Figure 3.10. 177,949 tracklets (40%) contain only three detections. 170,584 tracklets were detected within 5% of the ecliptic, and 380,189 have negative ecliptic longitudinal proper motions. Tracklets detected at high ecliptic latitudes tend to be high in proper motion ($\backsim 100''\text{hr}^{-1}$, or $0.67^\circ\text{day}^{-1}$, and above). Figure 3.11 shows these objects following a color profile similar to stars and galaxies, suggesting a higher rate of false tracklets in regions further from the ecliptic.

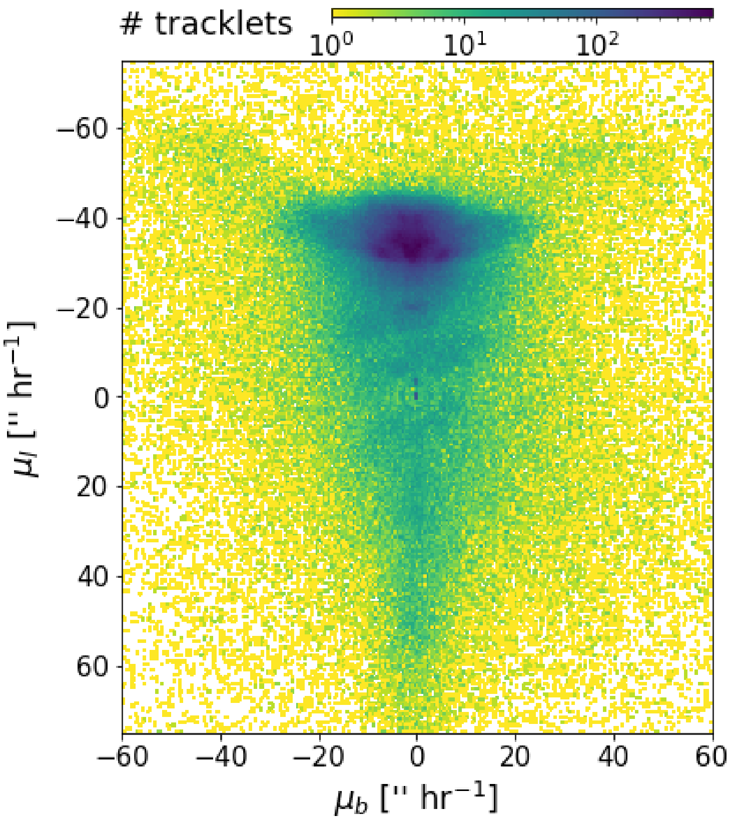

Figure 3.8 Density plot of the proper motions [$''$hr^{-1}] in ecliptic coordinates of tracklets found in the NSC using CANFind. Distinct groups of families are present, most distinctly the main belt group (μ_l ∼-40$''$hr^{-1}or -0.27°day^{-1}), Jupiter Trojans (∼-20$''$hr^{-1}or -0.13°day^{-1}), and some Kuiper Belt Objects (∼-3$''$hr^{-1}or 0.02°day^{-1}).

Samples of tracklets from high-density areas (galactic latitude ≤ 15°, 5° around LMC, 3° around SMC) were examined in more detail. Despite greater NSC exposure coverage in the galactic plane, CANFind detected more tracklets near the Magellanic Clouds. A visual inspection of tracklets pulled from this area revealed a higher number of false positives detected near the MCs. It is likely that fewer tracklets were found in the galactic plane due to the crowding of sources and the optimal spacing between exposures in the MCs.

Several clear structures in proper motion space can be seen in Fig. 3.8, reflecting different groups of SSOs. Most tracklets have proper motions that indicate main-belt orbits with several other general asteroid groups represented as well. Most prominent, centered at roughly μ_l=$-40''$hr^{-1}(-0.27°day^{-1}), μ_b=0$''$hr^{-1}in μ-space is a group of tracklets consistent with MBA proper motion. The presence of Jupiter Trojans and Trans-Neptunian objects are evident at μ_l=$-20''$hr^{-1}(-0.13°day^{-1}) and μ_b=3$''$hr^{-1}(0.02°day^{-1}). A noticeable feature of proper motion distribution are the "wings", which extend from the MBA group. Terai et al. (2013) describe these structures as a result of the variety of inclination and semimajor axes values of MBAs. A more detailed analysis of each group will require orbital fitting (see Sec. 3).

Tracklets were detected in all photometric bands included in the NSC (*ugrizY* and *VR*). If a single tracklet contained multiple detections in the same band, their mean value was recorded as the tracklet's magnitude in that band. Figure 3.12 shows the normalized distribution of magnitudes for the *ugr* bands extending to $\sim$ 24 mag. Table 3.3 gives the number of tracklets with data in each band. This overall distribution of tracklet detections in the various bands largely reflects the underlying distribution of exposures in the NSC, but may also be affected by the asteroid compositions.

Table 3.4 lists the six most populous colors represented in the tracklet information. Interestingly, NSC tracklets show a bimodality in color identified in Ivezić et al. (2001), most notably in *g*-*r* vs *r*-*i* (see Figure 3.13). Objects which fall in the redder group are mainly S-type rocky (siliceous) asteroids, while those in the bluer group are C-type (carbonaceous) asteroids. 45.5% of tracklets fall roughly into the C-type group, with the remaining fraction closer to S-type.

Table 3.3: Number of NSC tracklets with at least one detection in a photometric band.

band	# tracklets
u	8,968
g	246,501
r	272,184
i	245,369
z	84,583
Y	26,791
VR	210,993

Table 3.4: Six most populous colors, "multicolor" groups

color	# tracklets	multicolor	# tracklets
g-r	195,762	g+r+i	117,202
r-i	147,372	r+i+z	26,543
g-i	144,447	g+r+z	16,826
i-z	54,287	i+z+Y	14,875
r-z	35,988	g+i+z	14,867
g-z	22,760	r+i+Y	4,581

A fraction of the tracklet measurements were found in images with exposure times long enough to produce a trailing effect, as no morphology cuts are made on tracklet measurements to remove elongated detections. NSC measurements are found with Source Extractor (Bertin and Arnouts, 1996), which can identify objects of various shapes including stars, elongated galaxies, and streaked SSOs. As a result, some trailed measurements of SSOs are identified and present in the NSC measurements table. Figure 3.14 gives an example of trails left by a tracklet detected by CANFind. For reference, 119 of the 255,454 NSC DR1 images have exposure times $\geq$ 1000 seconds, and 881 have exposure times $\geq$ 600 sec. We find an approximate upper limit on the proper motion of CANFind tracklets containing measurements from these images, proportional to exposure time. This corresponds a the limit on trailed detections represented as single source detections in the NSC. Trails longer

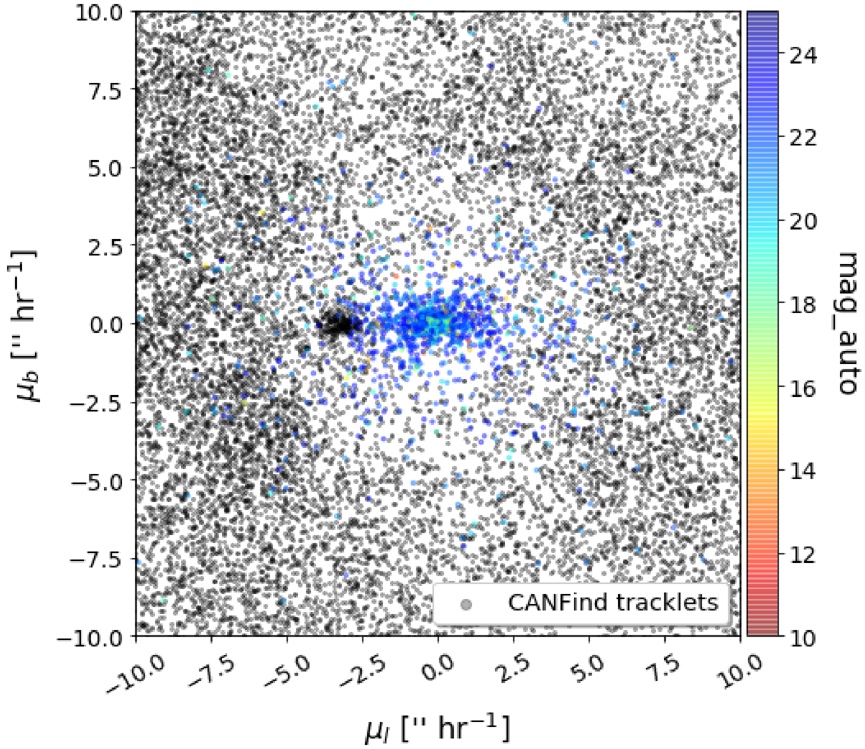

Figure 3.9 Proper motions of tracklets detected with the main CANFind algorithm (gray), and objects identified by the vetting process (sec. 3) with color as apparent magnitude. The gap around μ=0 left by CANFind (see center panel of Fig. 3.7) is filled in by this extra step.

than ∽13" are not identified by CANFind as the source extraction process will incorrectly identify multiple sources from a single streak, all with the same observation date. Future analysis will properly identify longer trails.

Future Work

Recovered tracklet measurements, along with measurements not associated with stationary objects, are stored in a PostgreSQL database at MSU for ease of access, similar to the one used to house the NSC in the Astro Data Lab. In the future, we plan to run CANFind on the second data release of the NSC and the same techniques described in this paper will be applied to the new data.

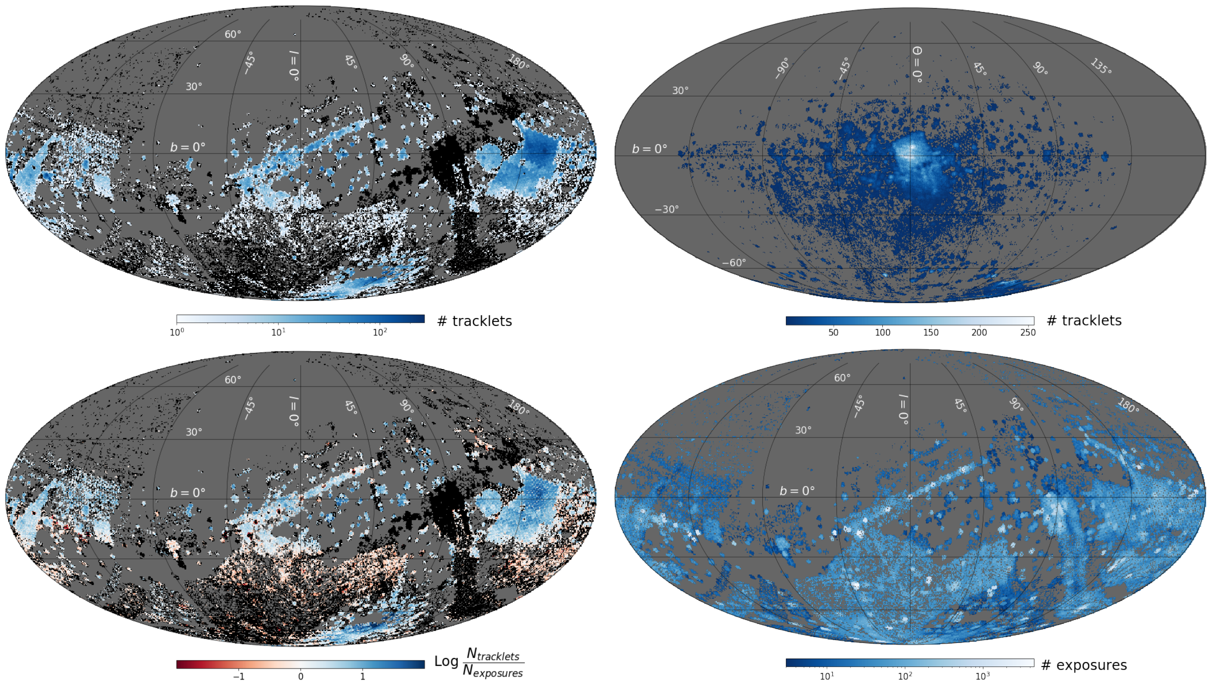

Figure 3.10 *(upper left)* tracklet density (number of tracklets per HEALPix, NSIDE=128) of NSC DR1 in ecliptic coordinates; grey areas had insufficient coverage to be searched, black areas were searched but contained no tracklets. *(upper right)* tracklet density in opposition-centric ecliptic coordinates. In place of ecliptic longitude, the x-axis represents Θ = angular separation from opposition, which is 180° from the apparent ecliptic longitude of the sun at the time of tracklet observation. Tracklets found at high ecliptic latitudes (i.e. LMC, SMC) are more likely to be false positives (see Sec. 3). *(lower right)* tracklet exposure density in ecliptic coordinates *(lower left)* density of the normalized tracklet/exposure ratio in ecliptic coordinates compares the relative amount of tracklet detection in an area to the amount of exposure coverage.

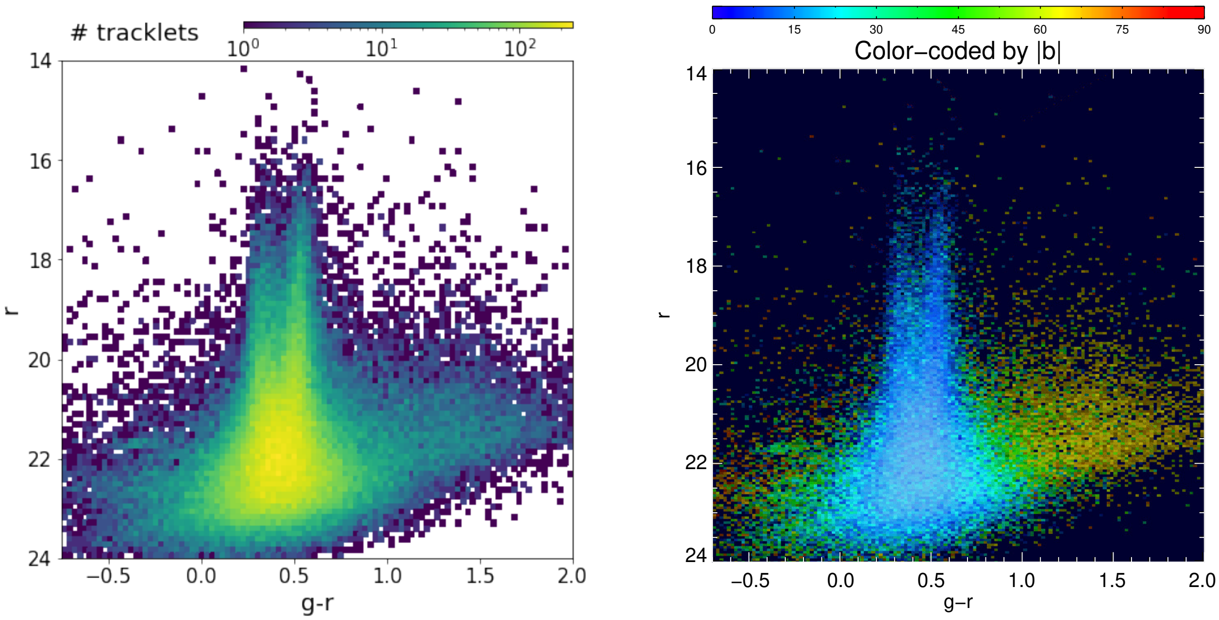

Figure 3.11 Color magnitude diagrams of the 107,604 tracklets found by CANFind with g and r band photometric data. *(left)* shows color as density, and *(right)* shows saturation as density and color as angular distance from the ecliptic (—b—, [°]). Tracklets that are far from the ecliptic tend to be high in proper motion and do not follow the bimodal color profile characteristic of most SSOs.

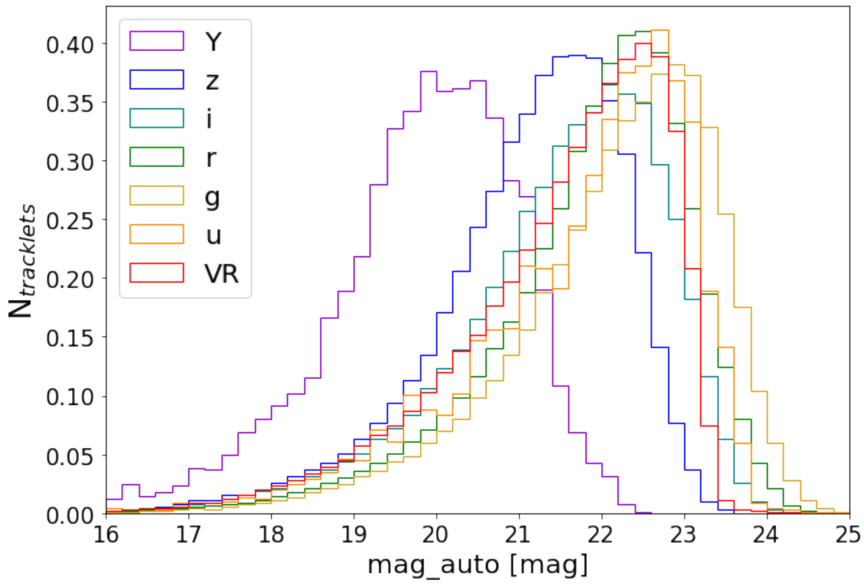

Figure 3.12 Normalized histogram of the apparent magnitudes of NSC tracklets extracted by CANFind.

According to Weryk et al. (2020), the Isolated Tracklet File (ITF) of the Minor Planet Center, the organization responsible for the designation of all minor SSOs, holds over 16.6 billion unlinked measurements. Once further developed, CANFind may be applied to the ITF in hopes of reducing its volume.

The following steps will be taken next:

- *Linking Dispersed Measurements of Moving Objects with the Hough Transform:* While DBSCAN effectively extracts tracklets with closely-spaced measurements, it does not identify those with a more disperse layout. These detections will be connected via the Hough Transform approach, a feature extraction technique traditionally used to isolate features in an image (Duda and Hart, 1972), often straight lines or simple shapes. The process is related to the Radon Transform (Radon, 1917) and works roughly as follows: Every NSC measurement will cast votes for all trajectory parameters (ρ, θ) consistent with that measurement and the votes from other measurements accumulated in a 2-D

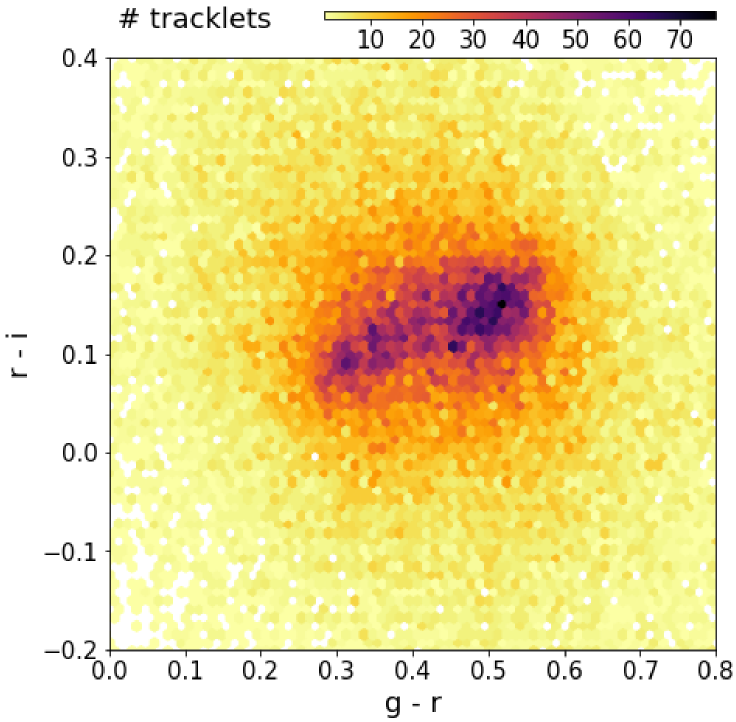

Figure 3.13 Color-color density plot of the 50,222 tracklets found by CANFind with g, r, and i band measurements. In particular, two distinct groups (bluer carbonaceous, left and redder siliceous, right) are visible.

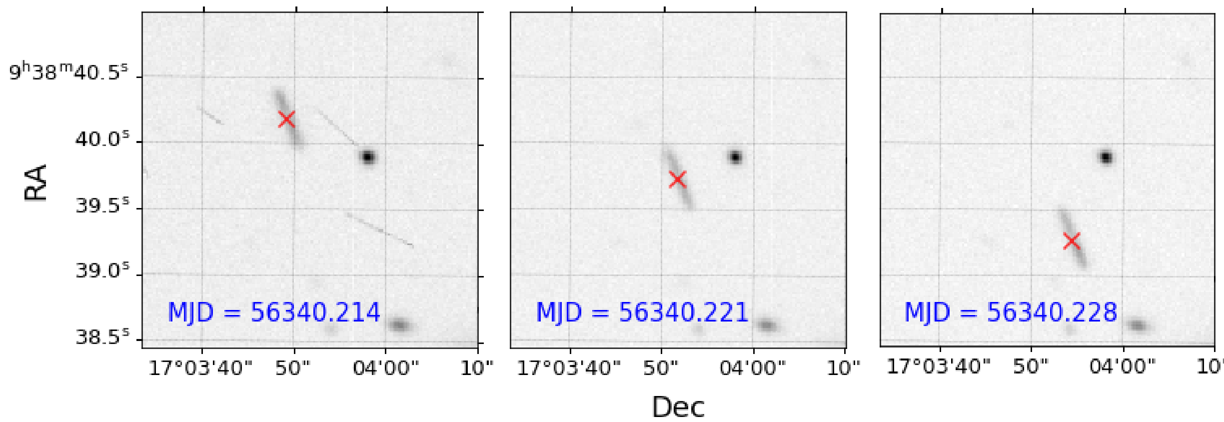

Figure 3.14 An example of a tracklet moving fast enough to leave streaked measurements in each 600-sec. exposure above. These CP-processed DECam exposures from NSC DR1 show 7″trails with their Source-Extracted measurements over-plotted in red crosses. The trail length for the exposure time matches the proper motion predicted by CANFind from the tracklet's trajectory, $\mu = 42''\text{hr}^{-1}$. *Note: For those interested, the "stationary" object behind the tracklet is white dwarf SDSS J093839.94+170357.7*

parameter/accumulator array. Multiple measurements voting for the same line will suggest a candidate trajectory, identified by peaks in the accumulator array.

The development of a modified version of the Hough Transform designed to work on data points rather than images is the subject of ongoing work.

- *Analysis of Trailed Detections:* We plan to identify and analyze streaked detections in NSC exposures to determine further SSO candidates in NSD DR1. While several tracklets detected by CANFind contain trailed measurements, individual streaks remain unidentified. These will be identified using new or existing software on exposures and analyzed using PSF fitting.

- *Orbit Determination:* Due to retrograde motion, linking tracks, tracklets, and unclustered measurements to form potential solar system orbits requires the use of an orbit fitting program designed to account for the effects of the Earth's motion on the apparent trajectories of other moving objects. Groups of measurements connected by a possible solar system orbit will be designated as a solar system object candidate, and will be studied and reported to the Minor Planet Center.

Properties of derived orbits will be analyzed against known objects. Many science questions can be addressed, especially considering the great quantity of observations available in the NSC. Once all tracks and tracklets in NSC DR1 have been identified using CANFind and the Hough Transform approach, they will be fit to possible SSO orbits. We hold off on this step until as many tracklets as possible can be identified in the NSC for the purpose of increasing the likelihood of correctly matching tracklets corresponding to unique objects.

- *Comparison of Efficiency with THOR:* The effectiveness of these detection methods will be tested against the results of Tracklet-less Heliocentric Object Recovery (THOR; Moeyens and Juric, 2019), which recovers known solar system objects by applying test orbits to object detections. THOR applies several orbits that are characteristic of distinct types of solar system objects to detections in a region of the sky, and objects placed in very similar orbits are evaluated and connected. When tested on data from the Zwicky Transient Facility, THOR recovered 97.4% of known asteroids (Moeyens and Juric, 2019). However, THOR has not yet been tested or optimized for NEOs and cannot generate initial orbits. We will run THOR on the NSC and compare the resulting set of solar system objects to those detected by the methods described above.

Summary

We describe CANFind, a new Solar System object detection algorithm which we have applied on DR1 of the NOIRLab Source Catalog. We detected 524,501 tracklets in 35,644 HEALPix of nside-128, covering 19% of the sky. The majority of tracklets have photometric data in the g, r, VR, and i bands, with fewer detections in u, z, and y. The 50,000 tracklets with measurements in the g, r, and i bands show a bimodality of siliceous and carbonaceous objects, supporting the results of prior studies. In proper motion space, tracklets fall into groups with motion indicating the presence of Main Belt objects, Jupiter Trojans, Hilda asteroids, and Trans-Neptunian objects. Roughly one third of all tracklets were detected within 5° of the ecliptic.

In the near future, CANFind will be run on NSC DR2 which contains 68 billion measurements of 3.9 billion unique objects (Nidever et al., 2020). The data will also be searched using a modified Hough Transform approach in order to link tracklets with detections that are farther spaced-out. Tracklets found will be fit to potential solar system orbits and submitted to the Minor Planet Center.

The CANFind source code and a complete catalog of the tracklets detected in the NSC DR1 are publicly available at `https://github.com/katiefasbender/CANFind`. The tracklet catalog includes information about each tracklet's mean (*RA,Dec*) position, date of first observation, average magnitude in each of the NSC's filters, proper motion in both equatorial and ecliptic coordinates [$^\circ$day^{-1}], in FITS format.

Software: *Astropy* (The Astropy Collaboration et al., 2018), *IPython* (Pérez and Granger, 2007), *matplotlib* (Hunter, 2007), *numpy* (Walt et al., 2011), *scipy* (Jones et al., 2001–), *healpy* (Zonca et al., 2019), *scikit-learn* (Pedregosa et al., 2011)

Facilities: CTIO:Blanco (DECam), KPNO:Mayall (Mosaic-3), Steward:Bok (90Prime), Astro Data Lab

EXPLORING THE SOLAR SYSTEM WITH THE NOIRLAB SOURCE CATALOG II: MAGNITUDE AND COLOR IN THE MAIN BELT

Contribution of Authors and Co-Authors

Manuscript in Chapter 4

Author: Katie M. Fasbender

Contributions: Lead Author, developed code and performed analysis.

Author: David L. Nidever

Contributions: Second author, guided analysis and methodology.

Manuscript Information

Katie M. Fasbender and David L. Nidever

Astrophysical Journal

Status of Manuscript:
_X_ Prepared for submission to a peer-reviewed journal
____ Officially submitted to a peer-reviewed journal
____ Accepted by a peer-reviewed journal
____ Published in a peer-reviewed journal

Institute of Physics Publishing

Abstract

Large surveys in astronomy are becoming vastly more tenable, however, data collection not only remains a steep financial cost but continues to require extensive labor and time. As a result, it is important to continue to use archival data for new science uses. The NSF's Optical-Infrared Astronomy Research Laboratory (NOIRLab) maintains a collection of deep photometric data in the optical/infrared regime, collected with ground-based telescopes. All publicly available data is incorporated into the NOIRLab Source Catalog (NSC), a multi-billion row collection of sources covering over 80 percent of the sky with nine years of observations. Four million measurements of Solar System OBjects (SSOs) were identified in the second data release of the NSC using the Computationally Automated NSC tracklet Finder (CANFind) and the Tough Transform. Of the SSOs detected in the NSC, 27,000 were known, Numbered Minor Planets with well-determined ephemerides; a definite majority are Main Belt Asteroids (MBAs). We present an overview of the solar system objects detected in the second data release of the NSC, and an analysis of the color and size distribution of collisional families in the main belt.

Introduction

The quantity and quality of data available from increasingly large astronomical surveys, catalogs, and simulations is rapidly changing how the solar system can be studied, from the analysis of single objects in great detail to the investigation of the system's overall structure and evolution through simulation, modeling, and comparison of object populations. Whether initially intended for solar system science, objects are routinely identified in large datasets in large numbers. Such catalogs of solar system objects (SSOs) reveal millions of objects at all distances from the sun with variations in surface features, composition, shape, size, rotation, dynamical history, and possible location of origin.

For example in the Sloan Digital Sky Survey (SDSS) commissioning data, Ivezić et al. (2001) identified a dichotomy of blue and red main belt asteroids in the optical g^*, r^*, i^* bands and an increase in blueness with helocentric distance, two phenomena that have appeared multiple times in literature since (e.g. Nesvorný et al. (2005); Peña et al. (2020)). Although the survey is not designed specifically for SSO detection or study, the SDSS Moving Object Catalog (Jurić et al., 2002) is on its fourth data release (Juric et al., 2007) and has yielded revelations about SSO sizes, dynamics, ages, and colors. The Panoramic Survey Telescope and Rapid Response System (Pan-STARRS, Chambers et al., 2016) has also been searched for objects, despite dedicating only 5% of its runtime to solar system science. Detections of SSOs found with the Pan-STARRS Moving Object Processing System (MOPS, Jedicke et al., 2005) have contributed to, among other results, the identification of asteroid families in the main belt (Bolin et al., 2017) and the derivation phase function parameters G, H for hundreds of thousands asteroids (Vereš et al., 2015).

The Gaia Space mission Gaia DR3 Solar System Survey (Tanga et al., 2023) is a subset of the greater Gaia mission to obtain a precise three-dimensional map of the sky. DR3 included mean reflectance spectra of 60,518 SSOs, which were compared by phase angle to reveal a increase in spectral slope and a decrease in the depth of the 1 μm absorption band with increasing ages of S-type asteroid families (Gaia Collaboration et al., 2023a), a possible indication of the aging of asteroid surfaces due to space weathering effects. Additionally, the Legacy Survey of Space and Time (LSST) is expected to observe approximately five million SSOs upon its in 2025 (Schwamb et al., 2023).

As early as the extensive Yerkes-McDonald Survey (Groeneveld and Kuiper (1954), Kuiper et al. (1958)) specialized searches for asteroid, often aimed at the ecliptic plane, have unearthed the distribution of matter in the solar system with photometric observations identifying colors and sizes among different populations. The Catalina Sky Survey (Larson et al., 1998) has been detecting Near Earth Object (NEOS) for decades, increasing discoveries yearly and contributing a number comparable to PanSTARRs NEO discoveries. The smaller Subaru Main Belt Asteroid Survey (SMBAS, Yoshida and Nakamura, 2007) detected nearly 2,000 sub-kilometer objects to study MBA by color and size, also identifying two groups of asteroids as S-like or C-like from their color indices.

Improvements to telescopes bring the search further away from the sun to the Trans-Neptunian region. For instance, the Colours of the Outer Solar System Origins Survey (COLOSSOS, Fraser et al., 2015) uses the Gemini North Telescope to study the surfaces of Trans-Neptunian objects (TNOS); Schwamb et al. (2019) presented the optical-infrared colors of 35 TNOS, showing a divide in g, r, J color space between red and neutral dynamically-excited populations.

As instruments and observatories age, the use of archival data should be a prevalent practice in astronomy. New observations are constantly incoming but are expensive to obtain. The same is true of all past data; as long as it has already been collected, it should be used for as many purposes as possible, scientific and technical. Catalogs which combine datasets have proven to be of much use in regards to solar system study. In particular, providing scientists with large catalogs of sources observed with the same photometric system that are measured and calibrated using the same method can help to remedy an issue regarding reporting SSO measurements: (Vereš et al., 2015) explains that asteroid magnitudes are reported by numerous observers and observatories over the past several decades, in random photometric systems with "varying concern for ensuring accuracy and precision."

An excellent example of archival data catalogued in practice is the Canadian Astronomy Data Centre's Solar System Object Search (CADC SSOS, Gwyn et al., 2012) which provides a search platform for SSOs in images taken by a number of instruments within and external to the CADC, including but not limited to the Canada-France-Hawaii Telescope's MegaCam, WIRCam, and CFH12K, the Hubble Space Telescope's WFPC, ACS, and WFC3, the Gemini GMOS, the Subaru Telescope's Suprime-Cam, and the entire SDSS DR8 catalog.

Multiple studies have used SSOS as a precovery tool to significant success. (Alexandersen et al., 2012) identified two new Jovian moons and found through SSOS images dating back to 2003 that had captured them before they were known. (Saifollahi et al., 2023) utilized SSOS in the recovery and characterization of NEOs, showing that objects with a high risk of impacting the Earth could have been found earlier than they had been discovered had the archival data been fully searched. Another search that found five new Neptunian trojans in the PS1 survey (Lin et al., 2016) consulted SSOS to find previous observations of candidates from the Dark Energy Survey and the Canada–France–Hawaii Telescope. These examples all show the need for organized and easily searchable collections of photometric data.

As more measurements of SSOs are gathered, constraints are placed on the Solar System's formation and evolution, as well as on the nature of the objects themselves. It is necessary to improve the completeness of our knowledge of its current matter distribution, the orbital dynamics, and object composition in each region of the solar system to determine similarities and differences. To do this, both details of the composition and surface features of single asteroids as well as a full-view comparison of the solar system's various structures must be investigated further. It will require an increase in the number of observations of known and unknown objects to (a) improve ephemeris calculation for better object recovery and precovery, (b) fill out light curves to better estimate object shape, rotation period, etc., and (c) gather spectral or color information, which tells us about composition of asteroid surfaces.

The millions of bodies orbiting the sun interact enough to affect each other's trajectories so the orbital elements of an asteroid change slightly with pertubations to their motion from their companions - the asteroid does not follow a fixed orbit, but a constantly adjusted path around the sun. To an observer on the Earth, the path an asteroid will follow as it moves around the sun with its perturbers appears as an ephemeris, a list recording the asteroid's position in the sky over some length of time. Several months of observations are needed to accurately calculate the ephemeris of an object, and to predict the object's past and future motion. Once the ephemeris of an SSO is determined, its physical properties can be estimated with better precision. Relevant to this work, the observed distribution of Main Belt asteroids in orbital element space shows traces of past interactions. Such a distribution may have been caused by by interactions with the existing giant planets or through gravitational self-stirring (Ida and Makino, 1992; Kokubo and Ida, 2000; Wetherill and Stewart, 1989), but not enough objects have well-defined ephemerides to confirm any one theory. Furthermore, the number of asteroids detected in groups of similar radii does not match predictions, especially in the outer solar system (Sheppard and Trujillo, 2010). Searches of deep, full-sky catalogs help to rule out observational bias in these cases.

As an asteroid travels relative to the earth, its apparent brightness increases and fades with the changing distance. The observed magnitude of an asteroid depends not only on the observing conditions but the asteroid's albedo, shape, rotation phase, surface features, and absence of an atmosphere (Vereš et al., 2015). Rotation periods can be derived from sparse photometric light curves for better calculation of its size, color, and shape, such as the relationship found between absolute magnitude and rotation by collecting data in the Asteroid Light Curve Database (Warner et al., 2009).

A basic estimate of an asteroid's diameter can be obtained through knowledge of its absolute magnitude. Mass distributions of interplanetary particles are typically described by power-law functions (Dohnanyi, 1969; Parker et al., 2008; Peña et al., 2020). Regarding main belt families, the sizes of family members can indicate the collisional history; a break in the cumulative size distribution of a family of objects indicates that the family's members are collisional fragments of a parent body (Kuiper et al., 1958; Novaković et al., 2022). Any newly discovered objects may also clarify the size distribution of sso groups and families.

From spectra or photometric color indices, the surface composition and morphology of an asteroid can be inferred, and from large datasets, a The current layout of matter the solar system depends on its dynamical history; there is much evidence of mass migration during and after the gaseous disk phase, especially within the main belt region. Since Ivezić et al. (2001), Trinquier et al. (2007) also found a color dichotomy between carbonaceous and non-carbonaceous asteroids and suggested either that they formed in two distinct reservoirs in the early Solar System (supported by isotopic analysis of meteorites, Kruijer et al. (2017)), or that they formed during two distinct periods (Warren, 2011).

When the planet cores were forming during this time, it is theorized that the orbital migration of giant planets Jupiter and Saturn disturbed objects from the orbits in which they formed, and shaped the inner solar system in the process. The theories regarding main belt evolution involve patterns of giant planet migration, different initial conditions of matter distribution, (Clement et al., 2018; Hansen, 2009; Walsh et al., 2011), but all must result in the main belt of the present day. Mainly, the second-most common S-type asteroids are dominantly observed in the interior belt, the most-common C-types are seen to populate the outer belt, and dark D-types typically orbit in outer main belt and in Jupiter's Trojan swarms with overlap between the populations (Raymond and Nesvorný, 2022). Starting as a classification between "red" silicate-type objects and "blue" carbonaceous objects, additional spectral and photometric observations have repeatedly transformed and expanded asteroid taxonomic systems throughout the years (Bus and Binzel, 2002; DeMeo et al., 2009; Tholen and Barucci, 1989). The bimodality in color observed in the main belt is also prevalent among Jupiter Trojans (Emery et al., 2024; McNeill et al., 2021) and in TNO observations (Schwamb et al., 2019), further indicating a disturbance of objects from their orbits of origin.

Ultimately, the surface color of asteroids is not only dependent on an object's composition. It was found that asteroid colors also depend on their family's age, partially due to space weathering of asteroid surfaces which reddens the surfaces of silicate-type objects but may have the opposite effect on carbonaceous surfaces (Nesvorný et al., 2005). This result is corroborated by spectral observation (Hasegawa et al., 2022). The question of whether the current knowledge of the main belt's color and size distributions is complete can only be answered through continued searches for objects in all areas of the solar system.

In the previous paper in this series (Exploring the Solar System with the NOIRLab Source Catalog I Fasbender and Nidever, 2021), we described the detection of SSO measurements in the NSC with the Computationally Automated NSC tracklet Finder (CANFind), and review the variety of moving objects identified with CANFind in the first data release of the NSC. Since then, THOR (Moeyens et al., 2021) at the Asteroid Institute has identified and submitted 27,000 previously unknown asteroids identified in the NSC to the Minor Planet Center. These objects were also identified in our previous paper; their measured coordinates and photometry are analyzed in this work.

This paper is organized as follows: Section 4 is an overview of the NOIRLab Source Catalog and its benefits for SSO science. Section 4 describes the two detection methods used to identify measurements of SSOs in NSC DR2 (4 CANFind and 4 The Tough Transform); Section 4 describes the process of initial orbit determination; Section 4 summarizes the results of crossmatching detections with the Minor Planet Center's observation database. In Section 4, the colors of known and unknown objects represented in the NSC are discussed, and conclusions are drawn in section 4.

NOIRLab Source Catalog

First released in 2017 (Nidever et al., 2018), the all-sky NOIRLab Source Catalog (NSC) combines years of archival optical-infrared photometric data collected by a range of observers from ground-based instruments in North and South America. The second data release (DR2) was created from 412,116 publicly available exposures from the Astro Data Archive[1] and presents over 68 billion individual observations of 3.9 billion distinct objects

[1]https://astroarchive.noirlab.edu

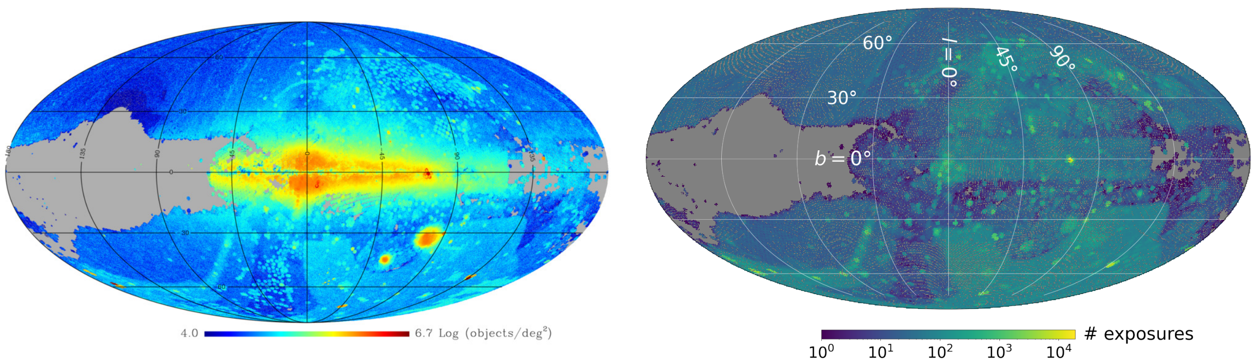

Figure 4.1 Density plots of NSC DR2. *(Left)* Object density plot of in galactic coordinates (figure from Nidever et al. (2021)). *(Right)* Number of exposures overlapping any piece of sky, on a logarithmic scale and in ecliptic coordinates.

(Nidever et al., 2021), shown in Figure 4.1.

83% of NSC DR2 exposures come from Dark Energy Camera on the Victor M. Blanco 4-meter Telescope at Cerro Tololo Inter-American Observatory in Chile, spanning from September 2012 to November 2019. The remaining were taken at the Kitt Peak National Observatory in the United States, with the Mosaic-3 imager on the Nicholas U. Mayall 4-meter Telescope from January 2016 to August 2017, and 90Prime wide-field imager on the 2.3-m Bok Telescope from November 2015 to February 2019 (Nidever et al., 2018).

Table 1 from Fasbender and Nidever (2021) lists the DR1 coverage timespan, field of view, number of CCDs, and pixel spacing for each instrument. Most exposure times are under five minutes with the average at 97 seconds, a minimum of 0.01 sec, and a maximum duration of 1600 sec. The NSC reports observation MJD for the start of each exposure, regardless of its duration. Figure 4.2 gives the full range of exposure times for each instrument.

Every exposure is processed with Source Extractor (Bertin and Arnouts, 1996) to measure the coordinates and brightness of each source via aperture photometry. Sources are then calibrated using astrometry from Gaia DR2 (Gaia Collaboration et al. (2016c), Gaia Collaboration et al. (2018b)) and photometry from the Pan-STARRS1 Survey (Chambers

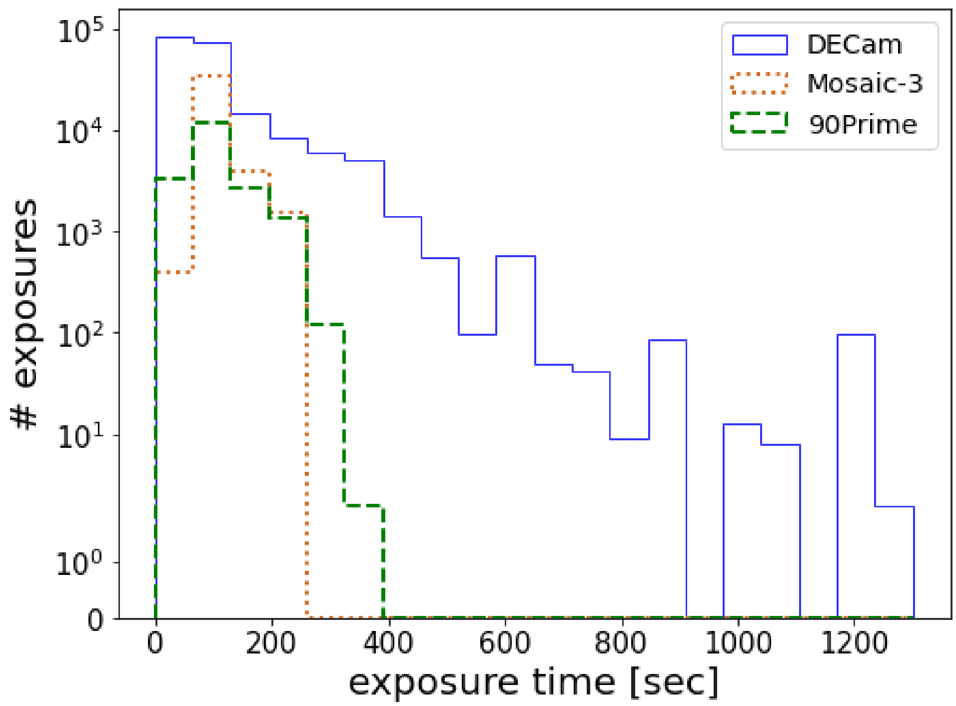

Figure 4.2 Histogram of exposure times corresponding to each instrument that provided data for the NSC: DECam (blue, solid), Mosaic-3 (orange, dotted), and 90Prime (green, dashed).

et al., 2016) in the northern hemisphere, and "model magnitudes" (generated from several public catalogs) for regions below δ = -29° (a complete description is found in Nidever et al. (2018)). Finally, source measurements are associated with each other to discern unique objects which were captured in multiple exposures. Measurements in the NSC are assigned to the same object only if they are successfully combined using the DBSCAN spacial clustering method described in Nidever et al. (2021). In general, detections that are within 0.5″of each other are combined in the assumption that they represent the same object observed at different times, as their proximity indicates the object is relatively stationary and has experienced little apparent motion between exposures. This process does not identify objects proper motion high enough to leave more than 0.5″between observations.

A full characterisation of the NSC in relation to SSOs is described in Fasbender and Nidever (2021); we provide a summary here.

Foremost, NSC DR2 is comprised of 357 independent proposals, most of which were not originally meant for the search for or study of SSOs. A number of these datasets have already been searched for new and known moving objects, so many observations are already reported. The rest observed at whatever time in whatever cadence, have within them millions of SSO measurements with important photometric information that has yet to be fully explored. The NSC records this information for all exposures released to the public, providing a way to search them simultaneously. Furthermore, sources from all exposures are measured and calibrated in the same process across the entire sky.

As seen in the left panel of Figure 4.1, a majority of the sky within ±30° of the ecliptic plane is covered by DR2 exposures. In this region, 124,110 exposures provide 1,259 nights of coverage for ∼60% of the sky. In total, the NSC covers 85% of the sky and approximately half of the galactic plane is included in the observed region (Nidever et al., 2021). Because the focus of SSO-specific surveys is often focused away from the galactic plane due to the higher density of objects in that area, and within the ecliptic plane of the solar system, the

NSC offers photometry over portions of the sky that have been previously under-examined.

Although the NSC is archival and there is no constant or uniform observing cadence, it has been shown that sparse, wide-field photometric data is still useful in many ways. Examples include comparisons of surface color among different SSO populations and the determination of an object's rotation period via photometric inversion (Carry et al., 2024; Vereš et al., 2015).

Enough measuremets of an SSO should be captured to determine its rotation period and to achieve long observational arcs before precise analysis is carried out. The chaotic nature of our object-filled solar system means the orbital elements of any object are not static. Several of an object's measurements must be connected to form its ephemeris, or the apparent path that the object traces across the sky as it orbits the sun and is affected by the other SSOs orbiting with it.

NSC exposures are each measured in one of seven photometric bands, $ugrizY$ and VR. As shown in Fasbender and Nidever (2021), thousands of moving objects have observations in multiple bands, providing color indices when corrected for each object's phase/rotation which will shed light on their surface properties. Each of the NSC's seven photometric bands has a median depth of 21 *mag* (Nidever et al., 2018), an adequate value for detecting TNOs whose magnitudes are typically less than 20 *mag*.

DR1 and DR2 were both subject to blending and overlapping issues in the most crowded areas of the sky, particularly in some regions within the galactic plane and the Magellanic Clouds. A third data release, which will include over 500,000 exposures, is expected in 2024. Updates to the data extraction method will include iterative source measurement with PSF-modeling to improve accuracy in crowded areas, a more uniform calibration method across the sky using PS1 and SkyMapper Catalogs, and a new combination technique `yente` which can identify objects with high proper motion that results in spatially separated measurements.

Most of the objects listed in the NSC are external to our solar system; their measurements are typically combined in the final NSC processing step with a $0.''5$ search radius. Leftover measurements may still belong to common objects, but their displacement between exposures renders them harder to link together into unique moving objects.

SSO Detection in the NSC

We classify objects in the NSC as either "stationary" (stars and galaxies) or "moving" (SSOs) according to the spacing of their individual measurements. As in the previous work, we continue to use the classic "tracklet approach" of identifying at least three detections of a unique moving object that make a relatively linear path over the course of <1 night; an assumption that can usually only be made over such short periods of time due to the complex motion of SSOs. The NSC DR2 was searched for tracklets using two methods: (1) the Computationally Automated NSC tracklet Finder (CANFind), and (2) an adapted form of the Hough Transform (Tough Transform).

Because of the high proper motion characteristic of most SSOs, they often appear as streaked trails in images with longer exposure times. NSC source measurement identifies these streaked sources at their center, where they would be midway through the exposure. However, the NSC reports observation time at the start of a source's exposure. While a typically small offset, this cannot be ignored. To account for this, SSO measurements identified in the NSC are offset by half of their corresponding exposure time for all analyses.

Detection Requirements in NSC Fields

A tracklet is defined as a linkage of at least three measurements, therefore we only consider an area of the NSC as "searchable" if it is covered by a minimum of three exposures. This is not restricted to a coverage of three exposures over one evening, although when using the tracklet approach, moving objects are most likely to be identified in areas which do have such coverage.

The hardest areas of the sky to search are those that suffer from source crowding, mainly within about 15° of the galactic plane and within 3 and 5° of the Small and Large Magellanic Clouds, respectively. Overlapping and blending of source measurements prevents objects from being distinguished or correctly extracted in the creation of the catalog and therefore may prevent SSO detections from being identified. This is taken into account only for the second detection method (the Tough Transform), as it searches for tracklets with measuement separations greater than 11″. An object with more closely-spaced measurements is far more likely to be identifiable in such areas, so the first detection method (CANFind) is run on NSC HEALPix regardless of source density.

CANFind

Initially developed to gauge the representation of tracklets in the NSC, the Computationally Automated NSC tracklet Finder (CANFind, Fasbender and Nidever, 2021) identifies both stationary and moving objects from their NSC measurements.

CANFind uses the Density-based Spacial Clustering of Applications with Noise (DBSCAN, Ester et al., 1996a) from `scikit-learn` (Pedregosa et al., 2011) to identify both distant "stationary" objects. DBSCAN easily clusters tracklets with measurements that are within ∼11″of each other. A validation step is included to ensure that the tracklet trajectories make physical sense. From the previous work, 96.5% of synthetic tracklets with average measurement spacing (Δs) between 0.5–10.9″ for proper motions between 2″$\mathrm{hr}^{-1}$and 209″hr^{-1} are recovered by CANFind to within 1″hr^{-1} of their input proper motion.

However, DBSCAN cannot cluster objects that leave more spaced-out measurements in the NSC, so their tracklets must be identified using a different method. This project develops create an adapted version of the Hough Transform in Python to identify moving objects in the NSC, which we call the "Tracklet Hough Transform" or "Tough Transform". Typically

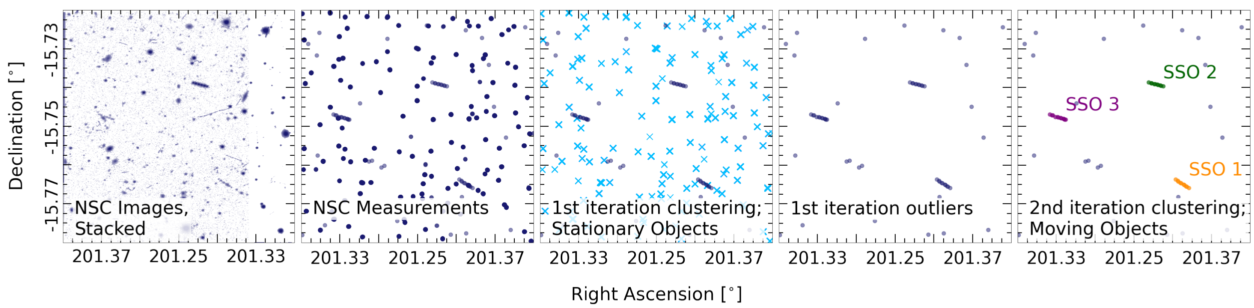

Figure 4.3 An example showing tracklets of three Solar System Objects (SSO) identified by CANFind from the NSC measurements table. The SSOs move rapidly ($\sim 40''$/hr) and show a "tracklet" while background objects keep a fixed position (*panel 2*). Measurements belonging to fixed objects are clustered (*panel 3*) and removed, leaving behind outlier measurements (*panel 4*) to be assigned to moving objects. A second iteration of clustering identifies the SSO tracklets (*panel 5*).

used to distinguish features in images, the Hough Transform can extract linear tracklets from the NSC if altered to accept data in the form of astronomical detections instead of pixels. The T-Hough Transform uses data from the NSC that was not categorized as "stationary" or "moving" by the CANFind method.

The CANFind process is outlined in Figure 4.3 and is explained in detail in (Fasbender and Nidever, 2021). Applied to the 34 billion measurements in NSC DR1, CANFind found 527,055 tracklets in 29,971 square degrees of the sky. CANFind is applied to all areas of NSC DR2 which meet the three-exposure requirement, regardless of source density.

The Tough Transform

The widely-used Hough Transform is a method used to extract features from images, often to identify straight lines or simple shapes. Developed in 1962 (Hough V, 1962), the process is related to the Radon Transform (Radon, 1917), which in turn is similar to the Fourier Transform. In its usual application to images, it transforms nonzero pixels in an image array into sinusoidal curves in Hough space, indicating a line or shape in the image as an intersection of these curves in Hough space.

Parameterization of Hough space with ρ, θ values was introduced by Duda and Hart (1972). The Tracklet Hough Transform (Tough Transform) applies the same parameterization to a quantized section of the sky, working on measured and calibrated source coordinates rather than image pixels. A brief overview of the Hough Transform as defined by these parameters is as follows:

On each nonzero pixel in the image, a "test line" is centered and incrementally rotated through 180°. For every angular increment, the configuration of the test line is recorded in the two parameters: ρ, the shortest distance from the image center to the test line, and θ, the line's angular orientation. The values of θ and ρ cast a "vote" in a corresponding element of an accumulator array, the size of which is determined by the number of possible values of θ and ρ. There is one row in the array for every angle tested, and one column for every possible discrete value of ρ, so each element of the accumulator array is represented by a specific combination of θ and ρ.

$$\begin{array}{ccccc} \rho_1 & \rho_2 & \rho_3 & \rho_4 & \ldots \end{array}$$
$$\begin{pmatrix} 0 & 0 & 0 & 0 & 0 \\ 0 & 1 & 0 & 0 & 0 \\ 0 & 1 & 4 & 0 & 1 \\ 0 & 0 & 0 & 1 & 3 \\ 0 & 0 & 0 & 0 & 1 \end{pmatrix} \begin{array}{c} \theta_1 \\ \theta_2 \\ \theta_3 \\ \theta_4 \\ \ldots \end{array}$$

For every orientation of the test line, the corresponding array element value is incremented by 1, signifying a vote for this test line configuration. As the angle progresses the votes forms a sinusoidal curve in Hough space, transforming the pixel from image space. If a group of data points form a line in the image, they will all generate test lines with very similar parameters and their curves in Hough space will all simultaneously intersect, indicated by a "peak" in the accumulator array. As every vote in the accumulator array represents a nonzero pixel in the image, and the number value of each array element represents the number of pixels which fall on that element's corresponding test line, i.e. the number of "votes" given to the test line. A threshold can be set for the minimum number of votes required to constitute a line that the Hough Transform has detected in the image.

Rather than apply a transformation to pixels in an image, the Tracklet Hough Transform (Tough Transform) uses this same process to identify lines of measurements of a moving object captured over an evening. For NSC measurements in an individual HEALPix (NSIDE=256, resolution $\sim$0.5°), the Tough transform identifies tracklets with more than 11″of separation between detections, which CANFind misses.

For every HEALPix, first a new coordinate system (x' and y') is established with its origin at the HEALPix center. This coordinate space is divided into discrete sections in x' and y', producing a grid of quantized coordinate values, reminiscent of an image's pixel array. Each measurement falls into one of the boxes, or cells, of this grid; that quantized location is used to calculate a corresponding ρ value for every increment of θ. The resolution of this grid determines the precision of the (θ, ρ) parameters calculated for each measurement, and therefore the size of the accumulator array. In order to avoid any one cell being occupied by multiple measurements, which would cause them to both produce the same line in Hough space, the resolution must be sufficiently small. If the cell size is too large, the resulting small amount of possible ρ values ends up preventing curves from intersecting when they should in the accumulator array. If the cell size is too small and there are too many possible ρ values, array elements that neighbor the correct one will receive excess votes and a "blurring" effect occurs where curves again fail to simultaneously intersect.

To determine the best way to divide each HEALPix (NSIDE=256) into cells, the number of detected lines and average percent error between detected line parameters and true parameters was obtained for a range of grid dimensions, from 50x50 to 5000x5000 cells (corresponding to 0″.3 and 0″.32, respectively) applied to data in pix 784814. The two things were important to consider in making a selection of cell size: (a) the number of peaks

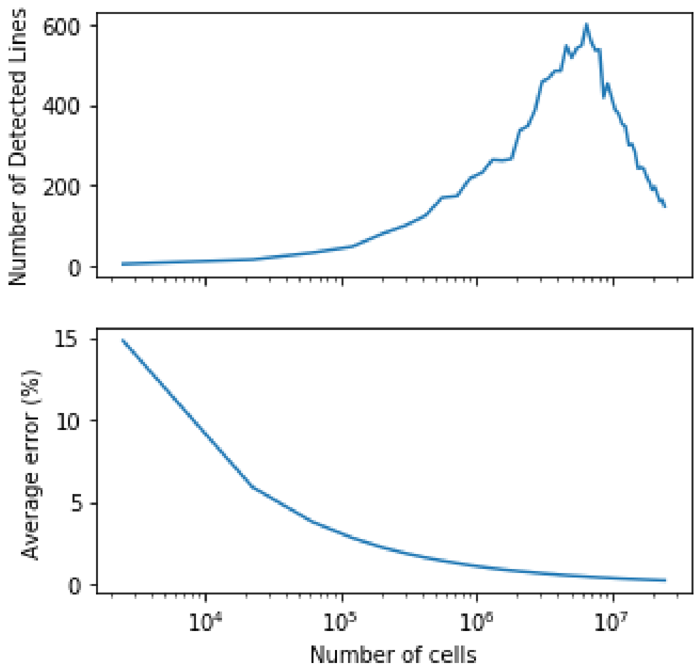

Figure 4.4 Comparison of the number of peaks detected in an accumulator array and fractional error in ρ vs. number of grid cells.

detected in an accumulator array (the number of lines detected in the data), and (b) the fractional error in the ρ values. If too many peaks are detected in the accumulator array, the computation time to test all each identified line for every HEALPix the entire catalog becomes unreasonable. On the other hand, the value of ρ obtained for every test line is rounded off by some amount in order to fit into the closest allowed array element every time a vote for that ρ value is recorded. If there aren't enough cells, the ρ values Tough Transform needs to detect the correct lines in the data are lost. Figure 4.4 compares the two factors as a function of (number of grid cells), and from this the best-case scenario is a cell count between 10^4 and 10^6. Reflecting the search radius commonly used to crossmatch object measurements, a cell width of $0''.5$ should assure that individual points are assigned to their own cell.

A large search area and a large number of measurements included in the search results in a corresponding large number of curves in Hough space. The prominent obstacle of noise from "background measurements" in both data and Hough space, which prevents the formation of clear peaks in the accumulator array and increases the total number of curve intersections. The area of sky that can be searched by the Tough Transform at once is restricted by the number of measurements, which increases with area, and by the angular distance over which an SSO could possibly during the course of one evening's worth of observations. Specifically, the assumption of a linear trajectory will only work for limited angular separations ($\sim 3^\circ$ on average for moderately distant objects, corresponding to about 14 days of motion), as the ephemeris of solar system objects traces out retrograde on the sky over longer periods of time as the Earth and observed objects orbit the sun. These two factors result in the selection of NSIDE=256.

As mentioned, this method was only used in areas at least 15° away from the galactic plane, and 3 and 5° away from the center of the Small and Large Magellanic Clouds, respectively. Additionally, the Tough Transform is applied only to the measurements that were not classified as CANFind as belonging to a stationary or moving object.

Another way noise was eliminated was through the use of the `photutils` function `Background2D` to estimate and subtract the background and RMS background noise of the accumulator array. In a sense, this step normalizes the background to reduce the difficulty of extracting peaks in noisier areas. `Background2D` estimates the sigma-clipped median background of sections of elements in an array, with noisier sections yielding higher median backgrounds. Figure 4.5 demonstrates the process, and the center panel shows the various median values that were detected. Subtracting the background leaves us with an array that has more clearly-defined peaks. Figure 4.6 finally gives us the resulting set of lines found in the array both before and after background subtraction. The number of detected lines is virtually cut in half, thanks to this step.

With this grid setup, we now proceed with the transformation. For each measurement,

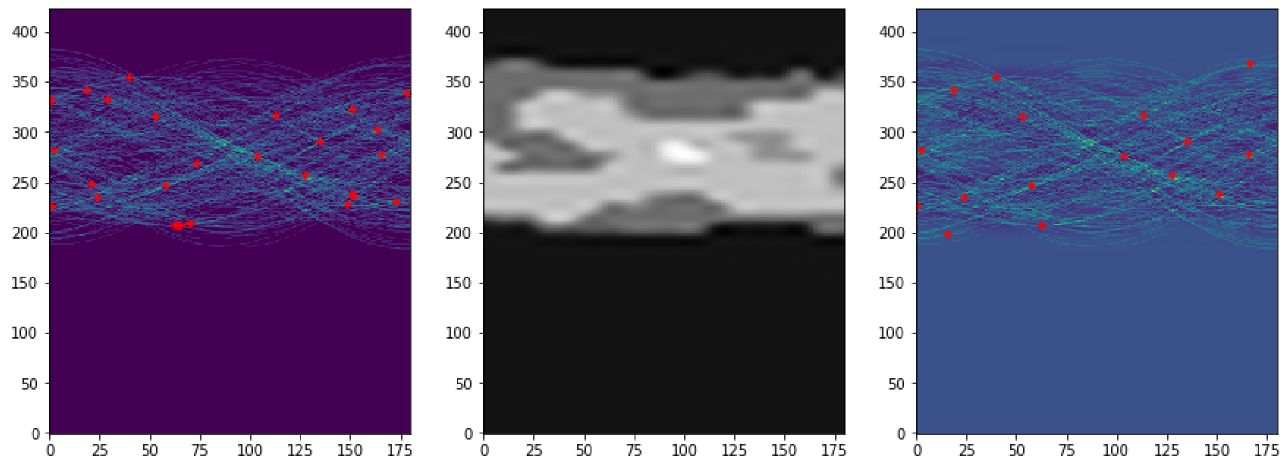

Figure 4.5 **Background Subtraction.** The process of background subtraction begins with the accumulator array *(left)*. Its median background *(center)* is detected and subtracted, leaving an array which yields a better selection of peaks *(right)*.

a test line is centered and rotated in 0.1° increments between ±90°.

To detect peaks in Hough Space, the `find_peak` function of the `photutils` package is applied to the background-subtracted accumulator array. It allows the user to set a threshold (which will correspond to the number of votes required to form a peak, 3) and to define a local region to search for peaks around every point or array element.

Every NSC measurement will cast votes for all trajectory parameters (ρ, θ) consistent with that measurement and the votes from other measurements accumulated in a 2-D parameter/accumulator array. Multiple measurements voting for the same line indicates a candidate ephemeris, identified by peaks in the accumulator array.

For every detected line, all points which voted for the line's parameters form a tracklet candidate. Due to the unavoidable noise from background objects, tracklets are often polluted with extra measurements that are eliminated with the same validation process used in CANFind. RANSAC, a linear regression algorithm that is robust to outliers, is applied to all measurements that voted for a certain line and iterates through subsets of members that

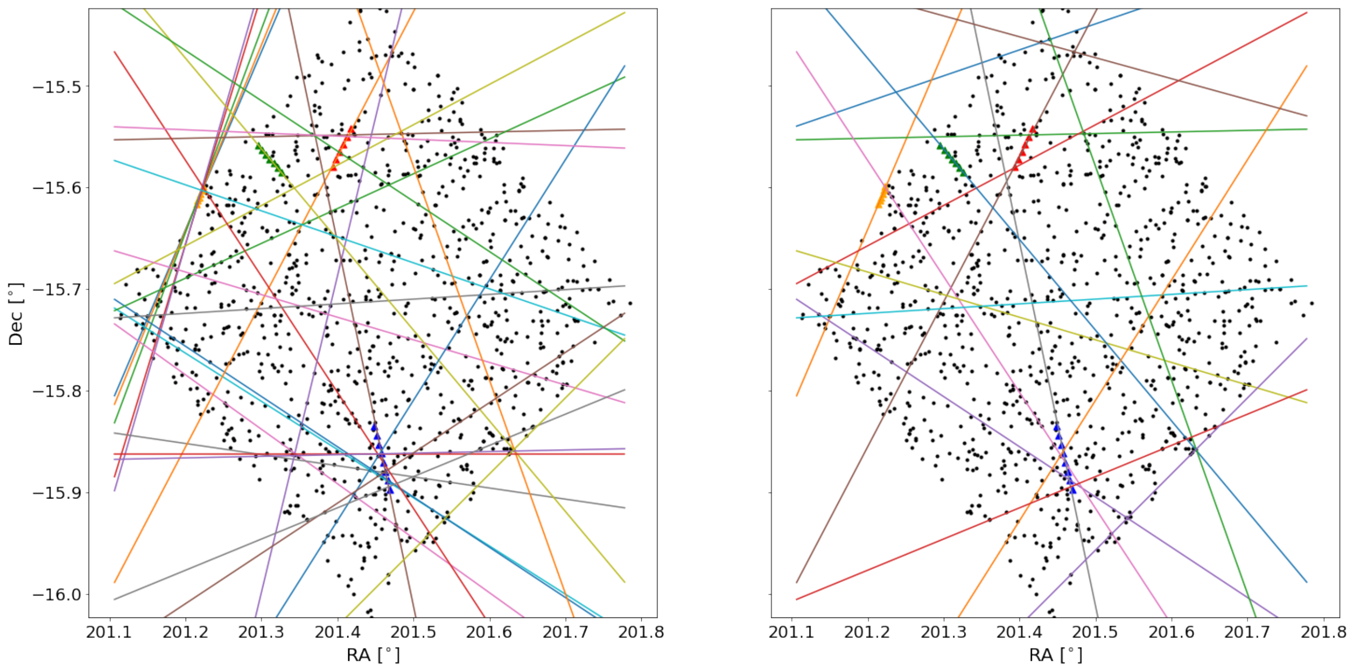

Figure 4.6 **Lines detected by THT:** Before background subtraction, the THT detects many false lines due to noise *(left)*. After background subtraction, most of the detected lines actually identify tracklets *(right)*. For example, the colorful triangles show four simulated tracklets that were correctly identified.

it tests as "inliers", fitting a line to them and comparing the residuals (only of the inlier set) between those subsets. RANSAC chooses the model with the lowest residuals, and identifies members which are the most likely to be outliers. The proper motion of valid tracklets is simply calculated from the inliers.

Initial Orbit Determination of Unmatched Objects and Isolated Tracklets

3,052,548 measurements of 662,320 tracklets were identified in NSC DR2, and an additional 1,628,911 measurements are classified as neither associated with a stationary object nor with a tracklet. Though some of these detections represent known objects, an initial determination of the orbit of each tracklet is determined. Orbital elements and ephemerides for each tracklet were calculated with the orbit-fitting program `Find_Orb`[2] (Gray, 2022).

The measurements of each tracklet are given to `Find_Orb` as one object, and the orbital elements are estimated with the method of Herget (Herget, 1935). These orbits are compared with the well-calculated orbits of Numbered Minor Planets in Section 4 to estimate their validity and usefulness.

The measurements of tracklets not associated with any known object are used to calculate an initial guess of the ephemeris to identify any further connections beyond one evening of observations. They are also used to estimate the distribution of colors of unidentified Main Belt objects in Section 4.

Because the assumption of linearity in motion is only applicable over short angular separations, the process of linking measurements over time periods longer than a few days must account for the effects of the Earth's motion on the apparent trajectories of other moving objects. `Find_Orb` determines an ephemeris for a moving object using

[2]https://www.projectpluto.com/find_orb.htm

given observations, regardless of whether the resulting orbit is physically possible. This functionality is the basis for tracklet linking in the NSC. The parameters of a generated ephemeris from any combination of tracklets indicate whether the combination's members belong to a unique object in a Solar System orbit.

Ephemeris generation begins with a group of tracklets residing within a short time and distance from each other. For each HEALPix of NSIDE=32 (resolution 1.8°) in which at least two tracklets were detected, a list of tracklet pairs is generated from exposures taken within 15 days of each other. All tracklets measured within this HEALPix and observed <15 days apart are compared. If the orbital elements calculated with the combined measurements of the tracklets have lower residuals than the elements calculated for the tracklets separately, and if the calculated object positions are within 10″of each other, the tracklets are considered to represent the same object. 409,267 tracklets were linked in this manner.

The longest ephemeris identified within the NSC by this work covers 2238 days with 5 measurements. Interestingly, the object with the most associated NSC detections, 173, was observed in the timespan of one evening. Details of calculated orbital elements of CANFind objects are elaborated upon in the following sections.

Crossmatching with Minor Planet Center Observations

In NSC DR2, 3,052,548 measurements are linked into 662,320 tracklets. An additional 1,628,911 measurements were not associated with any tracklet but were also not associated with any "stationary" object. All 4 million measurements of SSOs identified in the NSC were checked against the Minor Planet Center's database of optical, ground-based observations with a search radius of 0″.5. Although observation times are adjusted to reflect the time at the midpoint of a measurement's exposure, a difference in observation time no greater than 30 minutes between any two crossmatched measurements was allowed in order to account for potential discrepancies in the times reported to the MPC. Of the 4 million, 730,999 of

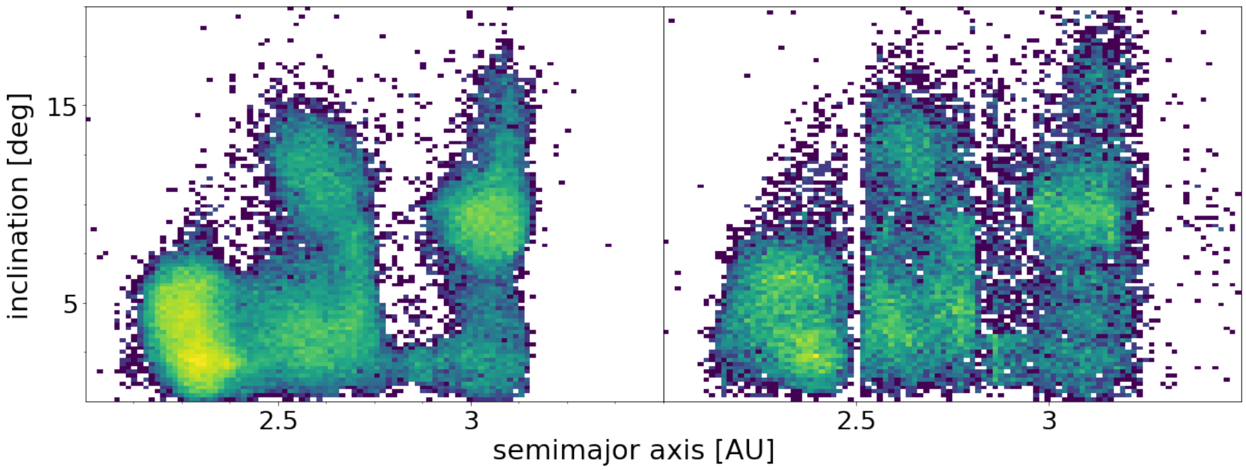

Figure 4.7 *(left)* Estimates of orbital parameters for NSC tracklets representing Numbered Minor Planets. *(right)* Calculated orbital parameters for the same numbered objects. The distribution of objects in semimajor axis a vs inclination [degrees] is similar for tracklet estimates and well-determined object orbits, apart from a general dispersion in both parameters.

these NSC measurements were crossmatched with observations of numbered and unnumbered minor planets and with isolated tracklets. Additional NSC measurements were associated with all three types of objects through tracklet connections. A breakdown of the number of measurements in each filter, both crossmatched with MPC measurments and associated with one through an NCS tracklet, is found in Table 4.1.

Numbered and Unnumbered Minor Planets: 282,657 measurements identified by CANFind were crossmatched to observations of 26,926 Numbered Minor Planets[3] from the MPC's database. We report an additional 16,525 NSC measurements of these objects that were not included in the MPC observations database; each of these NSC measurements belonged to one of 5,169 tracklets with at least one other measurement that was crossmatched to an existing MPC observation. At most, any one object was associated with 8 different tracklets.

160,088 NSC measurements were crossmatched with measurements of 27,478 UnNum-

[3] https://www.minorplanetcenter.net/iau/ECS/MPCAT-OBS/NumObs.txt.gz

bered Provisionally Designated Objects[4]. Through tracklet association, another 13,995 measurements of 4,399 of these minor planets are identified that were not present in the observations list.

Only one numbered object had more NSC measurements than previously known observations used to calculate its ephemeris (2012 TF3), but 199 objects with known orbits in the MPC Orbit Database were found to have more detections in the NSC than the number used to calculate their orbits. 698 unnumbered objects did not have known orbits at all; the average number of measurements per object for this sample is 10.

Orbital elements of numbered objects were evaluated against initial estimates of each of their corresponding tracklets' estimated orbit orbit. Figure 4.7 compares the semimajor axis to the inclination of tracklet orbit estimates and of numbered objects. Despite general uncertainty (as indicated by the lack of defined Kirkwood gaps in Figure 4.7), the initial estimate of an object's semimajor axis a is a decent indicator of what region of the solar system the orbit occupies in the case of unknown objects with single-tracklet information. This knowledge is applied to measurements of isolated trackets in the NSC.

Isolated Trackets: 276,261 measurements from 65,107 tracklets identified by CANFind were crossmatched with measurements from 67,371 tracklets in the the MPC's Isolated Tracklet File (ITF). An additional 29,737 measurements identified by CANFind were associated with existing tracklets in the ITF. A histogram of the number of measurements per object for numbered/unnumbered objects and isolated tracklets is found in Figure 4.8.

Unassociated Measurements: 3,905,635 measurements belonging to 504,686 tracklets identified by CANFind were not crossmatched with any optical measurement from the MPC observation database at their time of identification in the NSC. A brief analysis of colors derived from NSC measurements belonging to Isolated tracklets, and those unassociated with any object in the MPC observations database, is presented in Section 4. Table 4.2 lists

[4] `https://www.minorplanetcenter.net/iau/ECS/MPCAT-OBS/UnnObs.txt.gz`

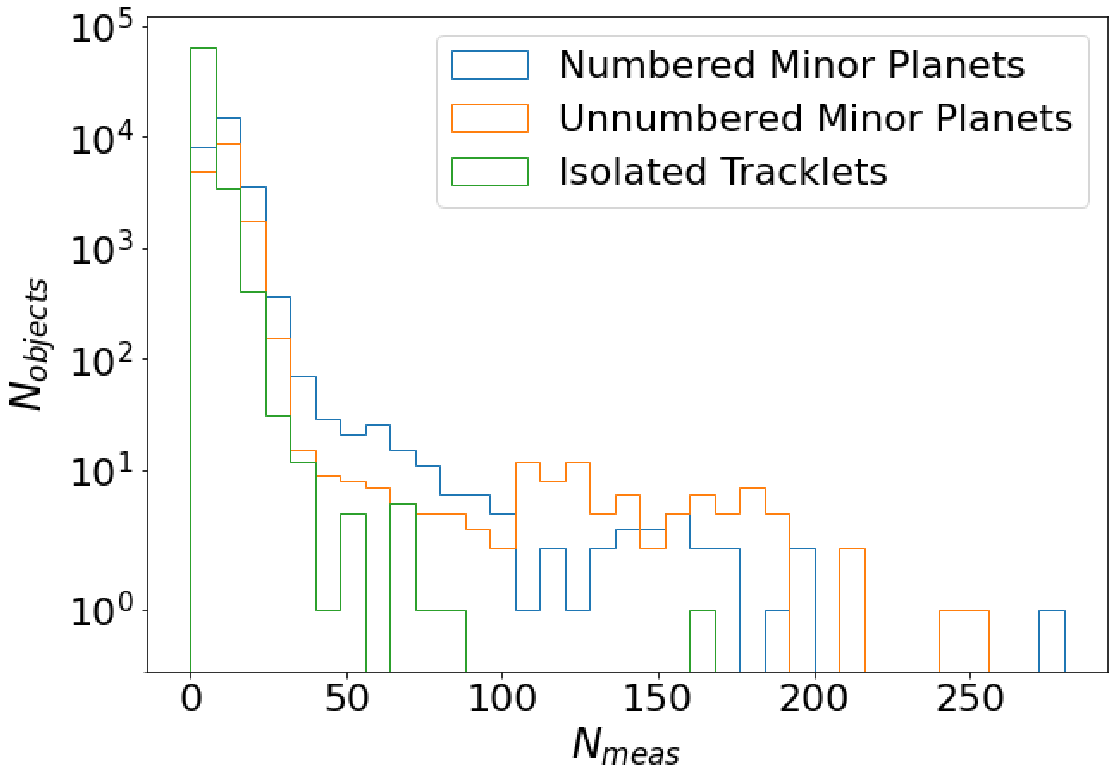

Figure 4.8 Histogram of known objects with observations in the MPC's database that were crossmatched with NSC measurements.

the six most populous colors, and the six most populous multicolors, among unassociated tracklets.

Table 4.1: Number of measurements in each filter for unassociated (UnX) measurements ($N_{meas,u}$), and for measurements either crossmatched with ($N_{meas,x}$), or associated with through NSC tracklets ($N_{meas,n}$), MPC observations of Numbered Minor Planets, Unnumbered Minor Planets, and Isolated Tracklets.

	UnX	Num MP		Unnum MP		Isolated Tracklets	
filter	$N_{meas,u}$	$N_{meas,n}$	$N_{meas,x}$	$N_{meas,n}$	$N_{meas,x}$	$N_{meas,n}$	$N_{meas,x}$
u	364035	412	53	55	4	6	3
g	555538	2700	2959	2026	2355	5417	5407
r	584999	4821	5422	3692	4341	5692	7126
i	509898	810	1147	1110	1082	3977	2716
z	797654	1299	2070	1380	1506	1505	689
Y	666152	214	7	123	1	13	0
VR	427359	6156	271112	4862	151546	10586	262861
Total	3905635	4708	282657	3995	160088	29737	276261

Table 4.2: Six most populous colors, “multicolors” of unassociated tracklets

color	# tracklets	multicolor	# tracklets
g-r	193255	*g+r+i*	116184
r-i	145870	*r+i+z*	26140
g-i	142816	*g+r+z*	16276
i-z	53563	*i+z+Y*	14837
r-z	35268	*g+i+z*	14490
g-z	22008	*r+i+Y*	4550

Color Information in the NSC

Color indices are calculated when possible for objects that either have known rotational periods, or when filter measurements were taken within 10 min in the case of unassociated and isolated tracklets. Known objects were crossmatched with entries in the Asteroid Light Curve Database. When crossmatching potential observations of family members in the NSC, family classifications (Milani et al. (2014), Knežević et al. (2014)) are used.

Of Numbered and Unnumbered Minor Planets

Most of NSC observations of Numbered and Unnumbered Minor Planets are in the VR band. Many objects have two-color information, but the average number of objects with detections in any combination of three filters is ∼20.

25,592 numbered objects have NSC measurements in only one filter, all but 1,124 of them captured in the *VR* band. 605 of those objects have measurements in only two filters, and 540 have measurements in just three filters. Similarly, 14,701 unnumbered objects are only represented with filter in the NSC, 1,193 not measured in *VR*. 582 have just single-color information, and 288 have data for two colors.

The most represented color for both types of object is *g-r,r-i*. 380 numbered objects have NSC measurements in the *gri* bands, between $1.8 \leq a \leq 34.9$ AU, and only 15 have

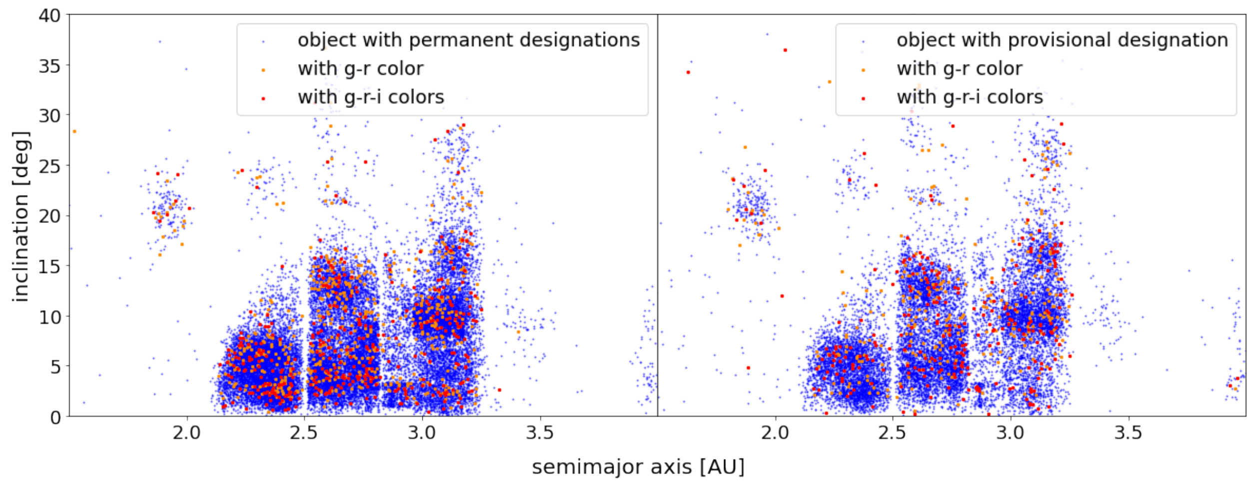

Figure 4.9 Orbital elements of numbered *(left)* and unnumbered *(right)* minor planets with detections in NSC DR2, focused on the Main Belt. Indicated in red and orange are objects with g-r color and g+r+i information.

known rotation periods in the Asteroid Light Cuve Database. The number drops to 287 unnumbered objects with gri measurements, between $1.2 \leq a \leq 45.3$ AU and without an estimated orbit. Most of these objects are in the Main Belt, but are so dispersed throughout orbital element space that few belong to a common collisional family.

Alternatively, 933 and 571 unnumbered objects have g-r color information. Figure 4.9 shows the orbital elements of objects with permanent and provisional designation which were identified in the NSC, indicating those with g-r-i colors and g-r colors.

Of Isolated Tracklets and Unreported Observations

Isolated tracklets were also lacking in color information; unassociated tracklets had the widest variety of color data. Because the rotational period for these objects is not known, the color indices calculated in g-r,r-i for tracklets feature a large ammount of uncertainty that is difficult to determine without more observations. As a result, we look at color in wide regions of orbital element space instead of attempting to constrain an analysis to any localized area.

Figure 4.10 shows the color-color diagram in g-r,r-i space for bins of inclination and phase angle, for objects estimated to reside in the main belt with a semimajor axis $2 \leq a \leq 3.5$ AU. Most objects are observed at or ear opposition; they show a distinct trend from red to blue with increasing inclination. This is consistent with the colors of known objects in the main belt; C-type asteroids are observed more consistently at most inclinations all regions of the area.

As phase angle increases, fewer objects fall into the color trends seen near opposition. It is known that increasing phase angle introduces uncertainty to both an object's observed brightness and color. The highest range of phase angles plotted in Figure 4.10 shows less of a dispersion in color for the redder group of objects than for the bluer group. For all inclinations, there is a lack of blue objects observed at high phase angles in comparison with observations at low phase angles. This is seen best in the highest range of inclinations, in which the blue group of objects is more prevelant than the red group. However, at the highest phase angles, the blue group almost completely disappears while the red group is still visible. This may be interpreted as an affect of phase angle observing that compromises the color of bluer objects more so than red objects, but further investigation is required.

Conclusions and Future Work

From the NSC's 68-billion row measurements table, CANFind and the Tough Transform discerned 4 million measurements of solar system objects, including ones that were identified only through the NOIRLab Source Catalog and not from any of the proposals comprising it.

All measurements were crossmatched with the Minor Planet Center's observations database. 731,000 measurements were crossmatched with existing observations of numbered and unnumbered minor planets, and with isolated tracklets. Most of these observations are in the *VR* band, as opposed to the variety seen in unassociated tracklets.

An initial estimate of tracklet orbits was obtained with the `Find_Orb` software.

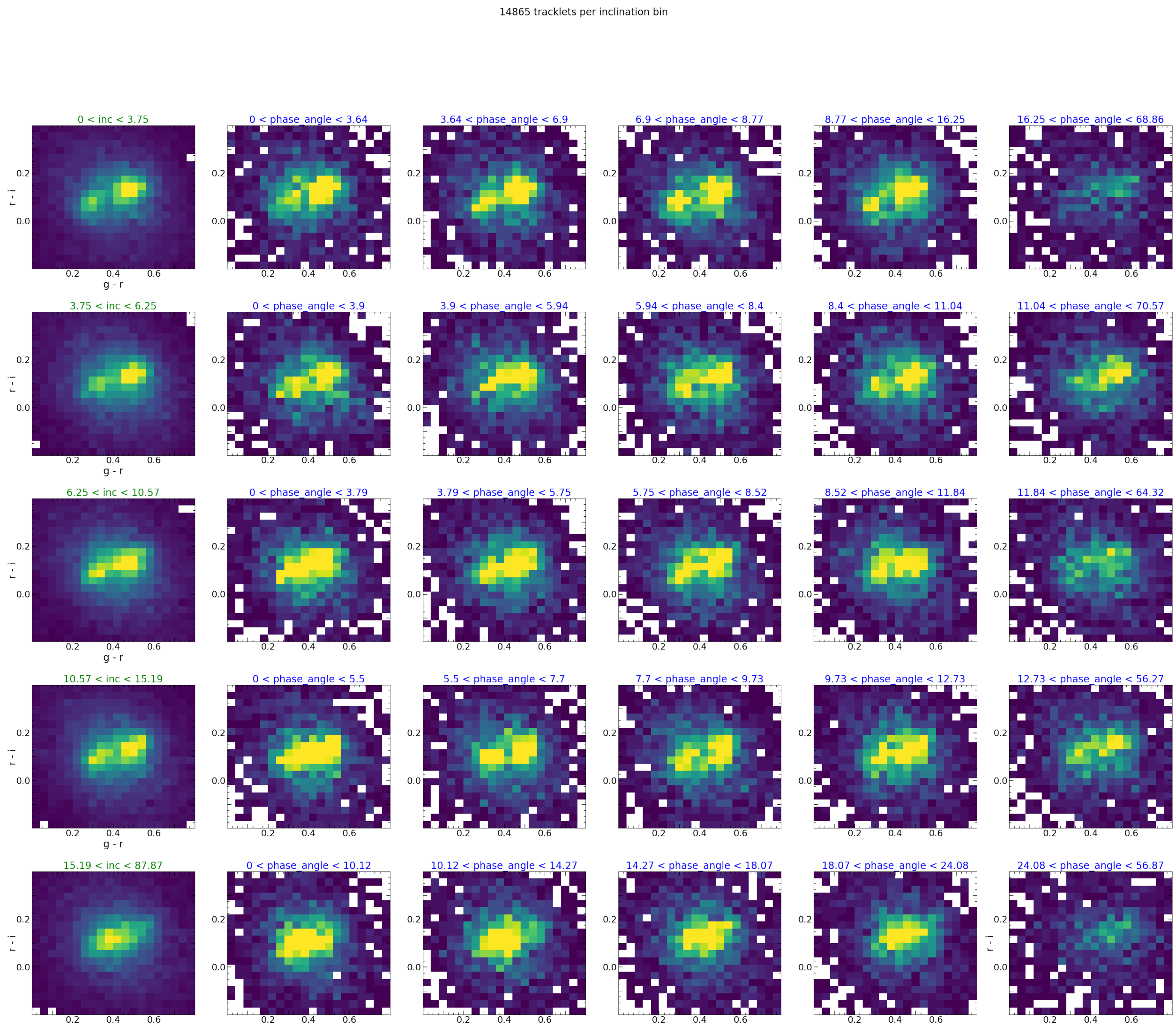

Figure 4.10 Colors of unassociated tracklets in bins of inclination, sized so the number of tracklets in each is the same (left column). Each bin in inclination is again split into bins of phase angle, sized so each has the same number of tracklets (right columns). Most objects are observed at or near opposition.

Comparisons between estimated orbital elements and well-measured orbital elements from the Minor Planet Center suggests that while one evening of observation may not be enough to precisely calculate an object's orbit, it gives a useful indication of its general location in the solar system.

Among Numbered and Unnumbered Minor Planets, a vast majority of measurements are in the VR band. Several hundred objects have multicolor information, but fewer have both this and known rotational periods. The NSC also contains previously unidentified measurements of known objects. Among isolated and unassociated tracklets, a clear affect on object color is seen with increasing phase angles. This seems to affect bluer objects more than redder ones, which should be further explored.

The NOIRLab Source catalog contains millions of detections of solar system objects across the entirety of its current nine-year observation span. DR3 will have even more exposures and an improved processing method, undoubtedly yielding a larger resulting catalog of SSO detections.

Software: *Astropy* (The Astropy Collaboration et al., 2018), *IPython* (Pérez and Granger, 2007), *matplotlib* (Hunter, 2007), *numpy* (Walt et al., 2011), *scipy* (Jones et al., 2001–), *healpy* (Zonca et al., 2019), *scikit-learn* (Pedregosa et al., 2011)

Facilities: CTIO:Blanco (DECam), KPNO:Mayall (Mosaic-3), Steward:Bok (90Prime), Astro Data Lab

CONCLUSION

The NOIRLab Source Catalog has provided the scientific community with uniform data captured with ground-based instruments in the optical-infrared wavelength range since 2017. The third data release of the NSC will contain over half a million images of the sky, and will produce a far larger final catalog. Measurement is updated from previous data releases to capture faint, small sources that were missed in crowded regions. Sources are also modeled with point-spread functions to better estimate their brightness before calibration.

Astrometric calibration remains the same as the process used for DR2, with the updated Gaia DR3 Catalog. Photometric calibration with Gaia synthetic photometry is considered as an alternative to calibration with a combination of smaller reference catalogs. This could address the issue of inconsistent zero-point measurements across the sky, and synthetic photometry can be calculated in all NSC filters. However, synthetic photometry is ultimately rejected for use in the NSC as it appears to falter in areas of the sky which exhibit high levels of extinction and source crowding. Alternate catalogs will be tested and implemented. Once measurement and calibration have been completed, combination and ubercalibration of sources will complete the catalog.

It is shown that the NSC is an excellent resource for solar system study. Two methods were developed to search its measurements for solar system objects: the Computationally Automated NSC tracklet Finder (CANFind) and the Tracklet Hough Transform (Tough Transform). These methods work one after another to sort out detections of distant "stationary" stars and galaxies from the NSC measurements table, then identify tracklets of moving objects in the remaining data.

Over 4 million measurements of moving objects were found in the second data release of the NOIRLab Source Catalog. 3 million of these measurements were identified as tracklets by CANFind (Chapter 3) and the Tough Transform (4). Tracklets were observed in all seven photometric passbands, and many have multicolor information. The initial orbits of these tracklets, calculated by the `Find_Orb` software, reveal that the NSC contains detections of solar system objects all over the solar system, primarily in the Main Asteroid Belt.

NSC observations were crossmatched with observations from the Minor Planet Center's database, then with entries of the Asteroid Light Curve Database to identify objects with known rotational periods so magnitude corrections could be made. Detections of known, numbered and unnumbered minor planets from the Minor Planet Center's observation database were crossmatched with these NSC measurements, as well as detections from the isolated tracklet file. A majority of NSC measurements of moving objects were unknown at the time of their identification by CANFind and the Tough Transform. All types of objects crossmatched with NSC measurements were observed almost exclusively in the VR band, severely limiting the color information available for them.

The most popular color across all types of object is g-r. Several hundred known objects had g-r or g-r,r-i data available, only 15 of which had calcuated rotational periods. An analysis of g-r color of numbered and unnumbered objects may be conducted if careful consideration is taken to account for the variation of asteroid brightness due to rotation and proper motion, among other factors.

Unassociated tracklets were far more abundant and more likely to have measurements in two or more filters. We examine the g-r,r-i colors of Main Belt objects, which were the most represented in the NSC. A general reddening of colors is seen with increasing phase angle for objects at all inclinations. This appears to affect objects with bluer, carbonaceous surfaces more so than redder, silicious surfaces. The presence of this trend in the NSC is an indicator of the ability of large, archival datasets to detect subtle differences and effects among SSO populations, which only become apparent over very long periods of observation.

As larger and more powerful surveys become reality, we must prepare for the influx of new solar system information by carefully studying detections in existing catalogs. The NSC is one of the largest source catalogs available in the optical range, making it a key tool for scientists in multiple fields of astronomy. Vast amounts of data will soon become available for analysis and will reveal countless questions about not just the solar system, but about every aspect of the universe that is studied. This does not detract from the usefulness of archival data, which has countless applications besides the purpose for which it was collected. All sources of information, new and old alike, offer the path to a greater understanding of the orbiting bodies around us and our place among them.

REFERENCES CITED

M. Alexandersen, B. Gladman, C. Veillet, R. Jacobson, M. Brozović, and P. Rousselot. Discovery of Two Additional Jovian Irregulars. , 144(1):21, July 2012. doi: 10.1088/0004-6256/144/1/21.

L. Allen, F. Valdes, D. Trilling, D. James, D. Herrera, C. Fuentes, T. Axelrod, J. Rajagopal, and C. T. I.-A. O. IAU Minor Planet Center. The size distribution of Near-Earth Asteroids from the DECam NEO Survey. In *AAS/Division for Planetary Sciences Meeting Abstracts #48*, volume 48 of *AAS/Division for Planetary Sciences Meeting Abstracts*, page 311.09, Oct. 2016.

K. Batygin and M. E. Brown. Evidence for a Distant Giant Planet in the Solar System. , 151(2):22, Feb. 2016. doi: 10.3847/0004-6256/151/2/22.

K. Batygin, F. C. Adams, M. E. Brown, and J. C. Becker. The planet nine hypothesis. , 805:1–53, May 2019. doi: 10.1016/j.physrep.2019.01.009.

E. Bertin and S. Arnouts. SExtractor: Software for source extraction. , 117:393–404, June 1996. doi: 10.1051/aas:1996164.

B. Bhattacharya, A. Noriega-Crespo, B. E. Penprase, V. S. Meadows, M. Salvato, H. Aussel, D. Frayer, O. Ilbert, E. Le Floc'h, D. Looper, J. Surace, P. Capak, J. D. Giorgini, M. Granvik, C. Grillmair, A. Hagen, G. Helou, W. T. Reach, L. M. Rebull, D. B. Sanders, N. Scoville, K. Sheth, and L. Yan. Mid-infrared Photometric Analysis of Main Belt Asteroids: A Technique for Color-Color Differentiation from Background Astrophysical Sources. , 720(1):114–129, Sept. 2010. doi: 10.1088/0004-637X/720/1/114.

L. Bianchi, J. Herald, B. Efremova, L. Girardi, A. Zabot, P. Marigo, A. Conti, and B. Shiao. GALEX catalogs of UV sources: statistical properties and sample science applications: hot white dwarfs in the Milky Way. , 335(1):161–169, Sept. 2011. doi: 10.1007/s10509-010-0581-x.

A. Boattini, E. C. Beshore, G. J. Garradd, A. R. Gibbs, A. D. Grauer, R. E. Hill, R. A. Kowalski, S. M. Larson, and R. H. McNaught. The Discovery of 2008 TC3 at the Catalina Sky Survey. In *AAS/Division for Planetary Sciences Meeting Abstracts #41*, AAS/Division for Planetary Sciences Meeting Abstracts, page 9.02, Sept. 2009.

B. T. Bolin, M. Delbo, A. Morbidelli, and K. J. Walsh. Yarkovsky V-shape identification of asteroid families. , 282:290–312, Jan. 2017. doi: 10.1016/j.icarus.2016.09.029.

R. Brasser and S. J. Mojzsis. The partitioning of the inner and outer Solar System by a structured protoplanetary disk. *Nature Astronomy*, 4:492–499, Jan. 2020. doi: 10.1038/s41550-019-0978-6.

M. Brown. Observational bias and the clustering of distant eccentric kuiper belt objects. *The Astronomical Journal*, 154, 06 2017. doi: 10.3847/1538-3881/aa79f4.

M. E. Brown and K. Batygin. Observational Constraints on the Orbit and Location of Planet Nine in the Outer Solar System. , 824(2):L23, June 2016. doi: 10.3847/2041-8205/824/2/L23.

M. E. Brown and K. Batygin. Orbital Clustering in the Distant Solar System. , 157(2):62, Feb. 2019. doi: 10.3847/1538-3881/aaf051.

M. E. Brown, C. Trujillo, and D. Rabinowitz. Discovery of a Candidate Inner Oort Cloud Planetoid. , 617(1):645–649, Dec. 2004. doi: 10.1086/422095.

S. J. Bus and R. P. Binzel. Phase II of the Small Main-Belt Asteroid Spectroscopic Survey. A Feature-Based Taxonomy. , 158(1):146–177, July 2002. doi: 10.1006/icar.2002.6856.

W. W. Campbell. Discovery of Asteroids by Photography. , 4(26):264, Nov. 1892. doi: 10.1086/120521.

B. Carry, P. Vernazza, F. Vachier, M. Neveu, J. Berthier, J. Hanuš, M. Ferrais, L. Jorda, M. Marsset, M. Viikinkoski, P. Bartczak, R. Behrend, Z. Benkhaldoun, M. Birlan, J. Castillo-Rogez, F. Cipriani, F. Colas, A. Drouard, G. P. Dudziński, J. Desmars, C. Dumas, J. Ďurech, R. Fetick, T. Fusco, J. Grice, E. Jehin, M. Kaasalainen, A. Kryszczynska, P. Lamy, F. Marchis, A. Marciniak, T. Michalowski, P. Michel, M. Pajuelo, E. Podlewska-Gaca, N. Rambaux, T. Santana-Ros, A. Storrs, P. Tanga, A. Vigan, B. Warner, M. Wieczorek, O. Witasse, and B. Yang. Evidence for differentiation of the most primitive small bodies. , 650:A129, June 2021. doi: 10.1051/0004-6361/202140342.

B. Carry, J. Peloton, R. Le Montagner, M. Mahlke, and J. Berthier. Combined spin orientation and phase function of asteroids. *arXiv e-prints*, art. arXiv:2403.20179, Mar. 2024. doi: 10.48550/arXiv.2403.20179.

K. C. Chambers, E. A. Magnier, N. Metcalfe, H. A. Flewelling, M. E. Huber, C. Z. Waters, L. Denneau, P. W. Draper, D. Farrow, D. P. Finkbeiner, C. Holmberg, J. Koppenhoefer, P. A. Price, A. Rest, R. P. Saglia, E. F. Schlafly, S. J. Smartt, W. Sweeney, R. J. Wainscoat, W. S. Burgett, S. Chastel, T. Grav, J. N. Heasley, K. W. Hodapp, R. Jedicke, N. Kaiser, R. P. Kudritzki, G. A. Luppino, R. H. Lupton, D. G. Monet, J. S. Morgan, P. M. Onaka, B. Shiao, C. W. Stubbs, J. L. Tonry, R. White, E. Bañados, E. F. Bell, R. Bender, E. J. Bernard, M. Boegner, F. Boffi, M. T. Botticella, A. Calamida, S. Casertano, W. P. Chen, X. Chen, S. Cole, N. Deacon, C. Frenk, A. Fitzsimmons, S. Gezari, V. Gibbs, C. Goessl, T. Goggia, R. Gourgue, B. Goldman, P. Grant, E. K. Grebel, N. C. Hambly, G. Hasinger, A. F. Heavens, T. M. Heckman, R. Henderson, T. Henning, M. Holman, U. Hopp, W. H. Ip, S. Isani, M. Jackson, C. D. Keyes, A. M. Koekemoer, R. Kotak, D. Le, D. Liska, K. S. Long, J. R. Lucey, M. Liu, N. F. Martin, G. Masci, B. McLean, E. Mindel, P. Misra, E. Morganson, D. N. A. Murphy, A. Obaika, G. Narayan, M. A. Nieto-Santisteban, P. Norberg, J. A. Peacock, E. A. Pier, M. Postman, N. Primak, C. Rae, A. Rai, A. Riess, A. Riffeser, H. W. Rix, S. Röser, R. Russel, L. Rutz, E. Schilbach, A. S. B. Schultz, D. Scolnic, L. Strolger, A. Szalay, S. Seitz, E. Small, K. W. Smith, D. R.

Soderblom, P. Taylor, R. Thomson, A. N. Taylor, A. R. Thakar, J. Thiel, D. Thilker, D. Unger, Y. Urata, J. Valenti, J. Wagner, T. Walder, F. Walter, S. P. Watters, S. Werner, W. M. Wood-Vasey, and R. Wyse. The Pan-STARRS1 Surveys. *arXiv e-prints*, art. arXiv:1612.05560, Dec. 2016. doi: 10.48550/arXiv.1612.05560.

M. S. Clement, N. A. Kaib, S. N. Raymond, and K. J. Walsh. Mars' growth stunted by an early giant planet instability. , 311:340–356, Sept. 2018. doi: 10.1016/j.icarus.2018.04.008.

M. Connors, P. Wiegert, and C. Veillet. Earth's Trojan asteroid. , 475(7357):481–483, July 2011. doi: 10.1038/nature10233.

C. J. Cunningham, B. G. Marsden, and W. Orchiston. How the first dwarf planet became the asteroid Ceres. *Journal of Astronomical History and Heritage*, 12(3):240–248, Nov. 2009.

Dark Energy Survey Collaboration, T. Abbott, F. B. Abdalla, J. Aleksić, S. Allam, A. Amara, D. Bacon, E. Balbinot, M. Banerji, K. Bechtol, A. Benoit-Lévy, G. M. Bernstein, E. Bertin, J. Blazek, C. Bonnett, S. Bridle, D. Brooks, R. J. Brunner, E. Buckley-Geer, D. L. Burke, G. B. Caminha, D. Capozzi, J. Carlsen, A. Carnero-Rosell, M. Carollo, M. Carrasco-Kind, J. Carretero, F. J. Castander, L. Clerkin, T. Collett, C. Conselice, M. Crocce, C. E. Cunha, C. B. D'Andrea, L. N. da Costa, T. M. Davis, S. Desai, H. T. Diehl, J. P. Dietrich, S. Dodelson, P. Doel, A. Drlica-Wagner, J. Estrada, J. Etherington, A. E. Evrard, J. Fabbri, D. A. Finley, B. Flaugher, R. J. Foley, P. Fosalba, J. Frieman, J. García-Bellido, E. Gaztanaga, D. W. Gerdes, T. Giannantonio, D. A. Goldstein, D. Gruen, R. A. Gruendl, P. Guarnieri, G. Gutierrez, W. Hartley, K. Honscheid, B. Jain, D. J. James, T. Jeltema, S. Jouvel, R. Kessler, A. King, D. Kirk, R. Kron, K. Kuehn, N. Kuropatkin, O. Lahav, T. S. Li, M. Lima, H. Lin, M. A. G. Maia, M. Makler, M. Manera, C. Maraston, J. L. Marshall, P. Martini, R. G. McMahon, P. Melchior, A. Merson, C. J. Miller, R. Miquel, J. J. Mohr, X. Morice-Atkinson, K. Naidoo, E. Neilsen, R. C. Nichol, B. Nord, R. Ogando, F. Ostrovski, A. Palmese, A. Papadopoulos, H. V. Peiris, J. Peoples, W. J. Percival, A. A. Plazas, S. L. Reed, A. Refregier, A. K. Romer, A. Roodman, A. Ross, E. Rozo, E. S. Rykoff, I. Sadeh, M. Sako, C. Sánchez, E. Sanchez, B. Santiago, V. Scarpine, M. Schubnell, I. Sevilla-Noarbe, E. Sheldon, M. Smith, R. C. Smith, M. Soares-Santos, F. Sobreira, M. Soumagnac, E. Suchyta, M. Sullivan, M. Swanson, G. Tarle, J. Thaler, D. Thomas, R. C. Thomas, D. Tucker, J. D. Vieira, V. Vikram, A. R. Walker, R. H. Wechsler, J. Weller, W. Wester, L. Whiteway, H. Wilcox, B. Yanny, Y. Zhang, and J. Zuntz. The Dark Energy Survey: more than dark energy - an overview. , 460(2):1270–1299, Aug. 2016. doi: 10.1093/mnras/stw641.

D. S. P. Dearborn, M. Bruck Syal, B. W. Barbee, G. Gisler, K. Greenaugh, K. M. Howley, R. Leung, J. Lyzhoft, P. L. Miller, J. A. Nuth, C. S. Plesko, B. D. Seery, J. V. Wasem, R. P. Weaver, and M. Zebenay. Options and uncertainties in planetary defense: Impulse-dependent response and the physical properties of asteroids. *Acta Astronautica*, 166: 290–305, Jan. 2020. doi: 10.1016/j.actaastro.2019.10.026.

M. Delbo, C. Avdellidou, and K. J. Walsh. Gaia Reflectance Spectra of Asteroid Collisional Families and the Search for the Origins of the Asteroids Ryugu and Bennu. In *LPI Contributions*, volume 2851 of *LPI Contributions*, page 2245, Aug. 2023.

D. DellaGiustina. Relationships Between Color & Morphology on Bennu. In *European Planetary Science Congress*, pages EPSC2020–481, Sept. 2020. doi: 10.5194/epsc2020-481.

F. E. DeMeo and B. Carry. The taxonomic distribution of asteroids from multi-filter all-sky photometric surveys. , 226(1):723–741, Sept. 2013. doi: 10.1016/j.icarus.2013.06.027.

F. E. DeMeo, R. P. Binzel, S. M. Slivan, and S. J. Bus. An extension of the Bus asteroid taxonomy into the near-infrared. , 202(1):160–180, July 2009. doi: 10.1016/j.icarus.2009.02.005.

L. Denneau, R. Jedicke, T. Grav, M. Granvik, J. Kubica, A. Milani, P. Vereš, R. Wainscoat, D. Chang, F. Pierfederici, N. Kaiser, K. C. Chambers, J. N. Heasley, E. A. Magnier, P. A. Price, J. Myers, J. Kleyna, H. Hsieh, D. Farnocchia, C. Waters, W. H. Sweeney, D. Green, B. Bolin, W. S. Burgett, J. S. Morgan, J. L. Tonry, K. W. Hodapp, S. Chastel, S. Chesley, A. Fitzsimmons, M. Holman, T. Spahr, D. Tholen, G. V. Williams, S. Abe, J. D. Armstrong, T. H. Bressi, R. Holmes, T. Lister, R. S. McMillan, M. Micheli, E. V. Ryan, W. H. Ryan, and J. V. Scotti. The Pan-STARRS Moving Object Processing System. , 125(926):357, Apr. 2013. doi: 10.1086/670337.

S. F. Dermott, D. Li, and A. A. Christou. Deconvolving the complex structure of the asteroid belt. *arXiv e-prints*, art. arXiv:2310.02873, Oct. 2023. doi: 10.48550/arXiv.2310.02873.

A. Dey, D. Rabinowitz, A. Karcher, C. Bebek, C. Baltay, D. Sprayberry, F. Valdes, B. Stupak, J. Donaldson, W. Emmet, T. Hurteau, B. Abareshi, B. Marshall, D. Lang, M. Fitzpatrick, P. Daly, D. Joyce, D. Schlegel, H. Schweiker, L. Allen, B. Blum, and M. Levi. Mosaic3: a red-sensitive upgrade for the prime focus camera at the Mayall 4m telescope. In C. J. Evans, L. Simard, and H. Takami, editors, *Ground-based and Airborne Instrumentation for Astronomy VI*, volume 9908 of *Society of Photo-Optical Instrumentation Engineers (SPIE) Conference Series*, page 99082C, Aug. 2016a. doi: 10.1117/12.2231488.

A. Dey, D. Rabinowitz, A. Karcher, C. Bebek, C. Baltay, D. Sprayberry, F. Valdes, B. Stupak, J. Donaldson, W. Emmet, T. Hurteau, B. Abareshi, B. Marshall, D. Lang, M. Fitzpatrick, P. Daly, D. Joyce, D. Schlegel, H. Schweiker, L. Allen, B. Blum, and M. Levi. Mosaic3: a red-sensitive upgrade for the prime focus camera at the Mayall 4m telescope. In C. J. Evans, L. Simard, and H. Takami, editors, *Ground-based and Airborne Instrumentation for Astronomy VI*, volume 9908 of *Society of Photo-Optical Instrumentation Engineers (SPIE) Conference Series*, page 99082C, Aug. 2016b. doi: 10.1117/12.2231488.

A. Dey, D. J. Schlegel, D. Lang, R. Blum, K. Burleigh, X. Fan, J. R. Findlay, D. Finkbeiner, D. Herrera, S. Juneau, M. Landriau, M. Levi, I. McGreer, A. Meisner, A. D. Myers,

J. Moustakas, P. Nugent, A. Patej, E. F. Schlafly, A. R. Walker, F. Valdes, B. A. Weaver, C. Yèche, H. Zou, X. Zhou, B. Abareshi, T. M. C. Abbott, B. Abolfathi, C. Aguilera, S. Alam, L. Allen, A. Alvarez, J. Annis, B. Ansarinejad, M. Aubert, J. Beechert, E. F. Bell, S. Y. BenZvi, F. Beutler, R. M. Bielby, A. S. Bolton, C. Briceño, E. J. Buckley-Geer, K. Butler, A. Calamida, R. G. Carlberg, P. Carter, R. Casas, F. J. Castander, Y. Choi, J. Comparat, E. Cukanovaite, T. Delubac, K. DeVries, S. Dey, G. Dhungana, M. Dickinson, Z. Ding, J. B. Donaldson, Y. Duan, C. J. Duckworth, S. Eftekharzadeh, D. J. Eisenstein, T. Etourneau, P. A. Fagrelius, J. Farihi, M. Fitzpatrick, A. Font-Ribera, L. Fulmer, B. T. Gänsicke, E. Gaztanaga, K. George, D. W. Gerdes, S. G. A. Gontcho, C. Gorgoni, G. Green, J. Guy, D. Harmer, M. Hernand ez, K. Honscheid, L. W. Huang, D. J. James, B. T. Jannuzi, L. Jiang, R. Joyce, A. Karcher, S. Karkar, R. Kehoe, J.-P. Kneib, A. Kueter-Young, T.-W. Lan, T. R. Lauer, L. Le Guillou, A. Le Van Suu, J. H. Lee, M. Lesser, L. Perreault Levasseur, T. S. Li, J. L. Mann, R. Marshall, C. E. Martínez-Vázquez, P. Martini, H. du Mas des Bourboux, S. McManus, T. G. Meier, B. Ménard, N. Metcalfe, A. Muñoz-Gutiérrez, J. Najita, K. Napier, G. Narayan, J. A. Newman, J. Nie, B. Nord, D. J. Norman, K. A. G. Olsen, A. Paat, N. Palanque-Delabrouille, X. Peng, C. L. Poppett, M. R. Poremba, A. Prakash, D. Rabinowitz, A. Raichoor, M. Rezaie, A. N. Robertson, N. A. Roe, A. J. Ross, N. P. Ross, G. Rudnick, S. Safonova, A. Saha, F. J. Sánchez, E. Savary, H. Schweiker, A. Scott, H.-J. Seo, H. Shan, D. R. Silva, Z. Slepian, C. Soto, D. Sprayberry, R. Staten, C. M. Stillman, R. J. Stupak, D. L. Summers, S. Sien Tie, H. Tirado, M. Vargas-Magaña, A. K. Vivas, R. H. Wechsler, D. Williams, J. Yang, Q. Yang, T. Yapici, D. Zaritsky, A. Zenteno, K. Zhang, T. Zhang, R. Zhou, and Z. Zhou. Overview of the DESI Legacy Imaging Surveys. , 157(5):168, May 2019. doi: 10.3847/1538-3881/ab089d.

J. S. Dohnanyi. Collisional Model of Asteroids and Their Debris. , 74:2531–2554, May 1969. doi: 10.1029/JB074i010p02531.

R. O. Duda and P. E. Hart. Use of the Hough transformation to detect lines and curves in pictures. *Communications of the ACM*, 15(1):11–15, 1 1972. ISSN 00010782. doi: 10.1145/361237.361242.

J. P. Emery, R. P. Binzel, D. T. Britt, M. E. Brown, C. J. A. Howett, A. C. Martin, M. D. Melita, A. C. Souza-Feliciano, and I. Wong. Surface Compositions of Trojan Asteroids. , 220(3):28, Mar. 2024. doi: 10.1007/s11214-024-01060-7.

M. Ester, H.-P. Kriegel, J. Sander, and X. Xu. A density-based algorithm for discovering clusters a density-based algorithm for discovering clusters in large spatial databases with noise. In *Proceedings of the Second International Conference on Knowledge Discovery and Data Mining*, KDD'96, page 226–231. AAAI Press, 1996a.

M. Ester, H.-P. Kriegel, J. Sander, and X. Xu. A density-based algorithm for discovering clusters a density-based algorithm for discovering clusters in large spatial databases with noise. KDD'96, page 226–231. AAAI Press, 1996b.

K. M. Fasbender and D. L. Nidever. Exploring the Solar System with the NOIRLab Source Catalog I: Detecting Objects with CANFind. , 162(6):244, Dec. 2021. doi: 10.3847/1538-3881/ac2230.

S. Ferrone, M. Delbo, C. Avdellidou, R. Melikyan, A. Morbidelli, K. Walsh, and R. Deienno. Identification of a 4.3 billion year old asteroid family and planetesimal population in the Inner Main Belt. , 676:A5, Aug. 2023. doi: 10.1051/0004-6361/202245594.

M. A. Fischler and R. C. Bolles. Random sample consensus: A paradigm for model fitting with applications to image analysis and automated cartography. *Commun. ACM*, 24 (6):381–395, June 1981. ISSN 0001-0782. doi: 10.1145/358669.358692. URL `https://doi.org/10.1145/358669.358692`.

B. Flaugher, H. T. Diehl, K. Honscheid, T. M. C. Abbott, O. Alvarez, R. Angstadt, J. T. Annis, M. Antonik, O. Ballester, L. Beaufore, G. M. Bernstein, R. A. Bernstein, B. Bigelow, M. Bonati, D. Boprie, D. Brooks, E. J. Buckley-Geer, J. Campa, L. Cardiel-Sas, F. J. Castander, J. Castilla, H. Cease, J. M. Cela-Ruiz, S. Chappa, E. Chi, C. Cooper, L. N. da Costa, E. Dede, G. Derylo, D. L. DePoy, J. de Vicente, P. Doel, A. Drlica-Wagner, J. Eiting, A. E. Elliott, J. Emes, J. Estrada, A. Fausti Neto, D. A. Finley, R. Flores, J. Frieman, D. Gerdes, M. D. Gladders, B. Gregory, G. R. Gutierrez, J. Hao, S. E. Holland, S. Holm, D. Huffman, C. Jackson, D. J. James, M. Jonas, A. Karcher, I. Karliner, S. Kent, R. Kessler, M. Kozlovsky, R. G. Kron, D. Kubik, K. Kuehn, S. Kuhlmann, K. Kuk, O. Lahav, A. Lathrop, J. Lee, M. E. Levi, P. Lewis, T. S. Li, I. Mandrichenko, J. L. Marshall, G. Martinez, K. W. Merritt, R. Miquel, F. Muñoz, E. H. Neilsen, R. C. Nichol, B. Nord, R. Ogando, J. Olsen, N. Palaio, K. Patton, J. Peoples, A. A. Plazas, J. Rauch, K. Reil, J. P. Rheault, N. A. Roe, H. Rogers, A. Roodman, E. Sanchez, V. Scarpine, R. H. Schindler, R. Schmidt, R. Schmitt, M. Schubnell, K. Schultz, P. Schurter, L. Scott, S. Serrano, T. M. Shaw, R. C. Smith, M. Soares-Santos, A. Stefanik, W. Stuermer, E. Suchyta, A. Sypniewski, G. Tarle, J. Thaler, R. Tighe, C. Tran, D. Tucker, A. R. Walker, G. Wang, M. Watson, C. Weaverdyck, W. Wester, R. Woods, B. Yanny, and DES Collaboration. The Dark Energy Camera. , 150(5):150, Nov. 2015. doi: 10.1088/0004-6256/150/5/150.

W. C. Fraser, M. Bannister, R. Pike, M. Schwamb, M. Marrset, J. Kavelaars, S. Benecchi, A. Delsanti, A. Guilbert-Lepoutre, A. Parker, N. Peixinho, P. Vernazza, and S.-Y. Wang. Col-OSSOS: Colours of the Outer Solar System Origins Survey. In *AAS/Division for Planetary Sciences Meeting Abstracts #47*, volume 47 of *AAS/Division for Planetary Sciences Meeting Abstracts*, page 211.15, Nov. 2015.

Gaia Collaboration, A. G. A. Brown, A. Vallenari, T. Prusti, J. H. J. de Bruijne, F. Mignard, R. Drimmel, C. Babusiaux, C. A. L. Bailer-Jones, U. Bastian, M. Biermann, D. W. Evans, L. Eyer, F. Jansen, C. Jordi, D. Katz, S. A. Klioner, U. Lammers, L. Lindegren, X. Luri, W. O'Mullane, C. Panem, D. Pourbaix, S. Randich, P. Sartoretti, H. I. Siddiqui, C. Soubiran, V. Valette, F. van Leeuwen, N. A. Walton, C. Aerts, F. Arenou,

M. Cropper, E. Høg, M. G. Lattanzi, E. K. Grebel, A. D. Holland, C. Huc, X. Passot, M. Perryman, L. Bramante, C. Cacciari, J. Castañeda, L. Chaoul, N. Cheek, F. De Angeli, C. Fabricius, R. Guerra, J. Hernández, A. Jean-Antoine-Piccolo, E. Masana, R. Messineo, N. Mowlavi, K. Nienartowicz, D. Ordóñez-Blanco, P. Panuzzo, J. Portell, P. J. Richards, M. Riello, G. M. Seabroke, P. Tanga, F. Thévenin, J. Torra, S. G. Els, G. Gracia-Abril, G. Comoretto, M. Garcia-Reinaldos, T. Lock, E. Mercier, M. Altmann, R. Andrae, T. L. Astraatmadja, I. Bellas-Velidis, K. Benson, J. Berthier, R. Blomme, G. Busso, B. Carry, A. Cellino, G. Clementini, S. Cowell, O. Creevey, J. Cuypers, M. Davidson, J. De Ridder, A. de Torres, L. Delchambre, A. Dell'Oro, C. Ducourant, Y. Frémat, M. García-Torres, E. Gosset, J. L. Halbwachs, N. C. Hambly, D. L. Harrison, M. Hauser, D. Hestroffer, S. T. Hodgkin, H. E. Huckle, A. Hutton, G. Jasniewicz, S. Jordan, M. Kontizas, A. J. Korn, A. C. Lanzafame, M. Manteiga, A. Moitinho, K. Muinonen, J. Osinde, E. Pancino, T. Pauwels, J. M. Petit, A. Recio-Blanco, A. C. Robin, L. M. Sarro, C. Siopis, M. Smith, K. W. Smith, A. Sozzetti, W. Thuillot, W. van Reeven, Y. Viala, U. Abbas, A. Abreu Aramburu, S. Accart, J. J. Aguado, P. M. Allan, W. Allasia, G. Altavilla, M. A. Álvarez, J. Alves, R. I. Anderson, A. H. Andrei, E. Anglada Varela, E. Antiche, T. Antoja, S. Antón, B. Arcay, N. Bach, S. G. Baker, L. Balaguer-Núñez, C. Barache, C. Barata, A. Barbier, F. Barblan, D. Barrado y Navascués, M. Barros, M. A. Barstow, U. Becciani, M. Bellazzini, A. Bello García, V. Belokurov, P. Bendjoya, A. Berihuete, L. Bianchi, O. Bienaymé, F. Billebaud, N. Blagorodnova, S. Blanco-Cuaresma, T. Boch, A. Bombrun, R. Borrachero, S. Bouquillon, G. Bourda, H. Bouy, A. Bragaglia, M. A. Breddels, N. Brouillet, T. Brüsemeister, B. Bucciarelli, P. Burgess, R. Burgon, A. Burlacu, D. Busonero, R. Buzzi, E. Caffau, J. Cambras, H. Campbell, R. Cancelliere, T. Cantat-Gaudin, T. Carlucci, J. M. Carrasco, M. Castellani, P. Charlot, J. Charnas, A. Chiavassa, M. Clotet, G. Cocozza, R. S. Collins, G. Costigan, F. Crifo, N. J. G. Cross, M. Crosta, C. Crowley, C. Dafonte, Y. Damerdji, A. Dapergolas, P. David, M. David, P. De Cat, F. de Felice, P. de Laverny, F. De Luise, R. De March, D. de Martino, R. de Souza, J. Debosscher, E. del Pozo, M. Delbo, A. Delgado, H. E. Delgado, P. Di Matteo, S. Diakite, E. Distefano, C. Dolding, S. Dos Anjos, P. Drazinos, J. Duran, Y. Dzigan, B. Edvardsson, H. Enke, N. W. Evans, G. Eynard Bontemps, C. Fabre, M. Fabrizio, S. Faigler, A. J. Falcão, M. Farràs Casas, L. Federici, G. Fedorets, J. Fernández-Hernández, P. Fernique, A. Fienga, F. Figueras, F. Filippi, K. Findeisen, A. Fonti, M. Fouesneau, E. Fraile, M. Fraser, J. Fuchs, M. Gai, S. Galleti, L. Galluccio, D. Garabato, F. García-Sedano, A. Garofalo, N. Garralda, P. Gavras, J. Gerssen, R. Geyer, G. Gilmore, S. Girona, G. Giuffrida, M. Gomes, A. González-Marcos, J. González-Núñez, J. J. González-Vidal, M. Granvik, A. Guerrier, P. Guillout, J. Guiraud, A. Gúrpide, R. Gutiérrez-Sánchez, L. P. Guy, R. Haigron, D. Hatzidimitriou, M. Haywood, U. Heiter, A. Helmi, D. Hobbs, W. Hofmann, B. Holl, G. Holland, J. A. S. Hunt, A. Hypki, V. Icardi, M. Irwin, G. Jevardat de Fombelle, P. Jofré, P. G. Jonker, A. Jorissen, F. Julbe, A. Karampelas, A. Kochoska, R. Kohley, K. Kolenberg, E. Kontizas, S. E. Koposov, G. Kordopatis, P. Koubsky, A. Krone-Martins, M. Kudryashova, I. Kull, R. K. Bachchan, F. Lacoste-Seris, A. F. Lanza, J. B. Lavigne, C. Le Poncin-Lafitte, Y. Lebreton, T. Lebzelter, S. Leccia, N. Leclerc, I. Lecoeur-Taibi, V. Lemaitre, H. Lenhardt, F. Leroux, S. Liao,

E. Licata, H. E. P. Lindstrøm, T. A. Lister, E. Livanou, A. Lobel, W. Löffler, M. López, D. Lorenz, I. MacDonald, T. Magalhães Fernandes, S. Managau, R. G. Mann, G. Mantelet, O. Marchal, J. M. Marchant, M. Marconi, S. Marinoni, P. M. Marrese, G. Marschalkó, D. J. Marshall, J. M. Martín-Fleitas, M. Martino, N. Mary, G. Matijevič, T. Mazeh, P. J. McMillan, S. Messina, D. Michalik, N. R. Millar, B. M. H. Miranda, D. Molina, R. Molinaro, M. Molinaro, L. Molnár, M. Moniez, P. Montegriffo, R. Mor, A. Mora, R. Morbidelli, T. Morel, S. Morgenthaler, D. Morris, A. F. Mulone, T. Muraveva, I. Musella, J. Narbonne, G. Nelemans, L. Nicastro, L. Noval, C. Ordénovic, J. Ordieres-Meré, P. Osborne, C. Pagani, I. Pagano, F. Pailler, H. Palacin, L. Palaversa, P. Parsons, M. Pecoraro, R. Pedrosa, H. Pentikäinen, B. Pichon, A. M. Piersimoni, F. X. Pineau, E. Plachy, G. Plum, E. Poujoulet, A. Prša, L. Pulone, S. Ragaini, S. Rago, N. Rambaux, M. Ramos-Lerate, P. Ranalli, G. Rauw, A. Read, S. Regibo, C. Reylé, R. A. Ribeiro, L. Rimoldini, V. Ripepi, A. Riva, G. Rixon, M. Roelens, M. Romero-Gómez, N. Rowell, F. Royer, L. Ruiz-Dern, G. Sadowski, T. Sagristà Sellés, J. Sahlmann, J. Salgado, E. Salguero, M. Sarasso, H. Savietto, M. Schultheis, E. Sciacca, M. Segol, J. C. Segovia, D. Segransan, I. C. Shih, R. Smareglia, R. L. Smart, E. Solano, F. Solitro, R. Sordo, S. Soria Nieto, J. Souchay, A. Spagna, F. Spoto, U. Stampa, I. A. Steele, H. Steidelmüller, C. A. Stephenson, H. Stoev, F. F. Suess, M. Süveges, J. Surdej, L. Szabados, E. Szegedi-Elek, D. Tapiador, F. Taris, G. Tauran, M. B. Taylor, R. Teixeira, D. Terrett, B. Tingley, S. C. Trager, C. Turon, A. Ulla, E. Utrilla, G. Valentini, A. van Elteren, E. Van Hemelryck, M. van Leeuwen, M. Varadi, A. Vecchiato, J. Veljanoski, T. Via, D. Vicente, S. Vogt, H. Voss, V. Votruba, S. Voutsinas, G. Walmsley, M. Weiler, K. Weingrill, T. Wevers, Ł. Wyrzykowski, A. Yoldas, M. Žerjal, S. Zucker, C. Zurbach, T. Zwitter, A. Alecu, M. Allen, C. Allende Prieto, A. Amorim, G. Anglada-Escudé, V. Arsenijevic, S. Azaz, P. Balm, M. Beck, H. H. Bernstein, L. Bigot, A. Bijaoui, C. Blasco, M. Bonfigli, G. Bono, S. Boudreault, A. Bressan, S. Brown, P. M. Brunet, P. Bunclark, R. Buonanno, A. G. Butkevich, C. Carret, C. Carrion, L. Chemin, F. Chéreau, L. Corcione, E. Darmigny, K. S. de Boer, P. de Teodoro, P. T. de Zeeuw, C. Delle Luche, C. D. Domingues, P. Dubath, F. Fodor, B. Frézouls, A. Fries, D. Fustes, D. Fyfe, E. Gallardo, J. Gallegos, D. Gardiol, M. Gebran, A. Gomboc, A. Gómez, E. Grux, A. Gueguen, A. Heyrovsky, J. Hoar, G. Iannicola, Y. Isasi Parache, A. M. Janotto, E. Joliet, A. Jonckheere, R. Keil, D. W. Kim, P. Klagyivik, J. Klar, J. Knude, O. Kochukhov, I. Kolka, J. Kos, A. Kutka, V. Lainey, D. LeBouquin, C. Liu, D. Loreggia, V. V. Makarov, M. G. Marseille, C. Martayan, O. Martinez-Rubi, B. Massart, F. Meynadier, S. Mignot, U. Munari, A. T. Nguyen, T. Nordlander, P. Ocvirk, K. S. O'Flaherty, A. Olias Sanz, P. Ortiz, J. Osorio, D. Oszkiewicz, A. Ouzounis, M. Palmer, P. Park, E. Pasquato, C. Peltzer, J. Peralta, F. Péturaud, T. Pieniluoma, E. Pigozzi, J. Poels, G. Prat, T. Prod'homme, F. Raison, J. M. Rebordao, D. Risquez, B. Rocca-Volmerange, S. Rosen, M. I. Ruiz-Fuertes, F. Russo, S. Sembay, I. Serraller Vizcaino, A. Short, A. Siebert, H. Silva, D. Sinachopoulos, E. Slezak, M. Soffel, D. Sosnowska, V. Straižys, M. ter Linden, D. Terrell, S. Theil, C. Tiede, L. Troisi, P. Tsalmantza, D. Tur, M. Vaccari, F. Vachier, P. Valles, W. Van Hamme, L. Veltz, J. Virtanen, J. M. Wallut, R. Wichmann, M. I. Wilkinson, H. Ziaeepour, and S. Zschocke. Gaia Data Release 1. Summary of the astrometric, photometric, and survey properties. , 595:A2, Nov. 2016a. doi: 10.1051/0004-6361/201629512.

Gaia Collaboration, T. Prusti, J. H. J. de Bruijne, A. G. A. Brown, A. Vallenari, C. Babusiaux, C. A. L. Bailer-Jones, U. Bastian, M. Biermann, D. W. Evans, and et al. The Gaia mission. , 595:A1, Nov. 2016b. doi: 10.1051/0004-6361/201629272.

Gaia Collaboration, T. Prusti, J. H. J. de Bruijne, A. G. A. Brown, A. Vallenari, C. Babusiaux, C. A. L. Bailer-Jones, U. Bastian, M. Biermann, D. W. Evans, L. Eyer, F. Jansen, C. Jordi, S. A. Klioner, U. Lammers, L. Lindegren, X. Luri, F. Mignard, D. J. Milligan, C. Panem, V. Poinsignon, D. Pourbaix, S. Randich, G. Sarri, P. Sartoretti, H. I. Siddiqui, C. Soubiran, V. Valette, F. van Leeuwen, N. A. Walton, C. Aerts, F. Arenou, M. Cropper, R. Drimmel, E. Høg, D. Katz, M. G. Lattanzi, W. O'Mullane, E. K. Grebel, A. D. Holland, C. Huc, X. Passot, L. Bramante, C. Cacciari, J. Castañeda, L. Chaoul, N. Cheek, F. De Angeli, C. Fabricius, R. Guerra, J. Hernández, A. Jean-Antoine-Piccolo, E. Masana, R. Messineo, N. Mowlavi, K. Nienartowicz, D. Ordóñez-Blanco, P. Panuzzo, J. Portell, P. J. Richards, M. Riello, G. M. Seabroke, P. Tanga, F. Thévenin, J. Torra, S. G. Els, G. Gracia-Abril, G. Comoretto, M. Garcia-Reinaldos, T. Lock, E. Mercier, M. Altmann, R. Andrae, T. L. Astraatmadja, I. Bellas-Velidis, K. Benson, J. Berthier, R. Blomme, G. Busso, B. Carry, A. Cellino, G. Clementini, S. Cowell, O. Creevey, J. Cuypers, M. Davidson, J. De Ridder, A. de Torres, L. Delchambre, A. Dell'Oro, C. Ducourant, Y. Frémat, M. García-Torres, E. Gosset, J. L. Halbwachs, N. C. Hambly, D. L. Harrison, M. Hauser, D. Hestroffer, S. T. Hodgkin, H. E. Huckle, A. Hutton, G. Jasniewicz, S. Jordan, M. Kontizas, A. J. Korn, A. C. Lanzafame, M. Manteiga, A. Moitinho, K. Muinonen, J. Osinde, E. Pancino, T. Pauwels, J. M. Petit, A. Recio-Blanco, A. C. Robin, L. M. Sarro, C. Siopis, M. Smith, K. W. Smith, A. Sozzetti, W. Thuillot, W. van Reeven, Y. Viala, U. Abbas, A. Abreu Aramburu, S. Accart, J. J. Aguado, P. M. Allan, W. Allasia, G. Altavilla, M. A. Álvarez, J. Alves, R. I. Anderson, A. H. Andrei, E. Anglada Varela, E. Antiche, T. Antoja, S. Antón, B. Arcay, A. Atzei, L. Ayache, N. Bach, S. G. Baker, L. Balaguer-Núñez, C. Barache, C. Barata, A. Barbier, F. Barblan, M. Baroni, D. Barrado y Navascués, M. Barros, M. A. Barstow, U. Becciani, M. Bellazzini, G. Bellei, A. Bello García, V. Belokurov, P. Bendjoya, A. Berihuete, L. Bianchi, O. Bienaymé, F. Billebaud, N. Blagorodnova, S. Blanco-Cuaresma, T. Boch, A. Bombrun, R. Borrachero, S. Bouquillon, G. Bourda, H. Bouy, A. Bragaglia, M. A. Breddels, N. Brouillet, T. Brüsemeister, B. Bucciarelli, F. Budnik, P. Burgess, R. Burgon, A. Burlacu, D. Busonero, R. Buzzi, E. Caffau, J. Cambras, H. Campbell, R. Cancelliere, T. Cantat-Gaudin, T. Carlucci, J. M. Carrasco, M. Castellani, P. Charlot, J. Charnas, P. Charvet, F. Chassat, A. Chiavassa, M. Clotet, G. Cocozza, R. S. Collins, P. Collins, G. Costigan, F. Crifo, N. J. G. Cross, M. Crosta, C. Crowley, C. Dafonte, Y. Damerdji, A. Dapergolas, P. David, M. David, P. De Cat, F. de Felice, P. de Laverny, F. De Luise, R. De March, D. de Martino, R. de Souza, J. Debosscher, E. del Pozo, M. Delbo, A. Delgado, H. E. Delgado, F. di Marco, P. Di Matteo, S. Diakite, E. Distefano, C. Dolding, S. Dos Anjos, P. Drazinos, J. Durán, Y. Dzigan, E. Ecale, B. Edvardsson, H. Enke, M. Erdmann, D. Escolar, M. Espina, N. W. Evans, G. Eynard Bontemps,

C. Fabre, M. Fabrizio, S. Faigler, A. J. Falcão, M. Farràs Casas, F. Faye, L. Federici, G. Fedorets, J. Fernández-Hernández, P. Fernique, A. Fienga, F. Figueras, F. Filippi, K. Findeisen, A. Fonti, M. Fouesneau, E. Fraile, M. Fraser, J. Fuchs, R. Furnell, M. Gai, S. Galleti, L. Galluccio, D. Garabato, F. García-Sedano, P. Garé, A. Garofalo, N. Garralda, P. Gavras, J. Gerssen, R. Geyer, G. Gilmore, S. Girona, G. Giuffrida, M. Gomes, A. González-Marcos, J. González-Núñez, J. J. González-Vidal, M. Granvik, A. Guerrier, P. Guillout, J. Guiraud, A. Gúrpide, R. Gutiérrez-Sánchez, L. P. Guy, R. Haigron, D. Hatzidimitriou, M. Haywood, U. Heiter, A. Helmi, D. Hobbs, W. Hofmann, B. Holl, G. Holland, J. A. S. Hunt, A. Hypki, V. Icardi, M. Irwin, G. Jevardat de Fombelle, P. Jofré, P. G. Jonker, A. Jorissen, F. Julbe, A. Karampelas, A. Kochoska, R. Kohley, K. Kolenberg, E. Kontizas, S. E. Koposov, G. Kordopatis, P. Koubsky, A. Kowalczyk, A. Krone-Martins, M. Kudryashova, I. Kull, R. K. Bachchan, F. Lacoste-Seris, A. F. Lanza, J. B. Lavigne, C. Le Poncin-Lafitte, Y. Lebreton, T. Lebzelter, S. Leccia, N. Leclerc, I. Lecoeur-Taibi, V. Lemaitre, H. Lenhardt, F. Leroux, S. Liao, E. Licata, H. E. P. Lindstrøm, T. A. Lister, E. Livanou, A. Lobel, W. Löffler, M. López, A. Lopez-Lozano, D. Lorenz, T. Loureiro, I. MacDonald, T. Magalhães Fernandes, S. Managau, R. G. Mann, G. Mantelet, O. Marchal, J. M. Marchant, M. Marconi, J. Marie, S. Marinoni, P. M. Marrese, G. Marschalkó, D. J. Marshall, J. M. Martín-Fleitas, M. Martino, N. Mary, G. Matijevič, T. Mazeh, P. J. McMillan, S. Messina, A. Mestre, D. Michalik, N. R. Millar, B. M. H. Miranda, D. Molina, R. Molinaro, M. Molinaro, L. Molnár, M. Moniez, P. Montegriffo, D. Monteiro, R. Mor, A. Mora, R. Morbidelli, T. Morel, S. Morgenthaler, T. Morley, D. Morris, A. F. Mulone, T. Muraveva, I. Musella, J. Narbonne, G. Nelemans, L. Nicastro, L. Noval, C. Ordénovic, J. Ordieres-Meré, P. Osborne, C. Pagani, I. Pagano, F. Pailler, H. Palacin, L. Palaversa, P. Parsons, T. Paulsen, M. Pecoraro, R. Pedrosa, H. Pentikäinen, J. Pereira, B. Pichon, A. M. Piersimoni, F. X. Pineau, E. Plachy, G. Plum, E. Poujoulet, A. Prša, L. Pulone, S. Ragaini, S. Rago, N. Rambaux, M. Ramos-Lerate, P. Ranalli, G. Rauw, A. Read, S. Regibo, F. Renk, C. Reylé, R. A. Ribeiro, L. Rimoldini, V. Ripepi, A. Riva, G. Rixon, M. Roelens, M. Romero-Gómez, N. Rowell, F. Royer, A. Rudolph, L. Ruiz-Dern, G. Sadowski, T. Sagristà Sellés, J. Sahlmann, J. Salgado, E. Salguero, M. Sarasso, H. Savietto, A. Schnorhk, M. Schultheis, E. Sciacca, M. Segol, J. C. Segovia, D. Segransan, E. Serpell, I. C. Shih, R. Smareglia, R. L. Smart, C. Smith, E. Solano, F. Solitro, R. Sordo, S. Soria Nieto, J. Souchay, A. Spagna, F. Spoto, U. Stampa, I. A. Steele, H. Steidelmüller, C. A. Stephenson, H. Stoev, F. F. Suess, M. Süveges, J. Surdej, L. Szabados, E. Szegedi-Elek, D. Tapiador, F. Taris, G. Tauran, M. B. Taylor, R. Teixeira, D. Terrett, B. Tingley, S. C. Trager, C. Turon, A. Ulla, E. Utrilla, G. Valentini, A. van Elteren, E. Van Hemelryck, M. van Leeuwen, M. Varadi, A. Vecchiato, J. Veljanoski, T. Via, D. Vicente, S. Vogt, H. Voss, V. Votruba, S. Voutsinas, G. Walmsley, M. Weiler, K. Weingrill, D. Werner, T. Wevers, G. Whitehead, Ł. Wyrzykowski, A. Yoldas, M. Žerjal, S. Zucker, C. Zurbach, T. Zwitter, A. Alecu, M. Allen, C. Allende Prieto, A. Amorim, G. Anglada-Escudé, V. Arsenijevic, S. Azaz, P. Balm, M. Beck, H. H. Bernstein, L. Bigot, A. Bijaoui, C. Blasco, M. Bonfigli, G. Bono, S. Boudreault, A. Bressan, S. Brown, P. M. Brunet, P. Bunclark, R. Buonanno, A. G. Butkevich, C. Carret, C. Carrion, L. Chemin, F. Chéreau, L. Corcione, E. Darmigny, K. S. de Boer, P. de Teodoro,

P. T. de Zeeuw, C. Delle Luche, C. D. Domingues, P. Dubath, F. Fodor, B. Frézouls, A. Fries, D. Fustes, D. Fyfe, E. Gallardo, J. Gallegos, D. Gardiol, M. Gebran, A. Gomboc, A. Gómez, E. Grux, A. Gueguen, A. Heyrovsky, J. Hoar, G. Iannicola, Y. Isasi Parache, A. M. Janotto, E. Joliet, A. Jonckheere, R. Keil, D. W. Kim, P. Klagyivik, J. Klar, J. Knude, O. Kochukhov, I. Kolka, J. Kos, A. Kutka, V. Lainey, D. LeBouquin, C. Liu, D. Loreggia, V. V. Makarov, M. G. Marseille, C. Martayan, O. Martinez-Rubi, B. Massart, F. Meynadier, S. Mignot, U. Munari, A. T. Nguyen, T. Nordlander, P. Ocvirk, K. S. O'Flaherty, A. Olias Sanz, P. Ortiz, J. Osorio, D. Oszkiewicz, A. Ouzounis, M. Palmer, P. Park, E. Pasquato, C. Peltzer, J. Peralta, F. Péturaud, T. Pieniluoma, E. Pigozzi, J. Poels, G. Prat, T. Prod'homme, F. Raison, J. M. Rebordao, D. Risquez, B. Rocca-Volmerange, S. Rosen, M. I. Ruiz-Fuertes, F. Russo, S. Sembay, I. Serraller Vizcaino, A. Short, A. Siebert, H. Silva, D. Sinachopoulos, E. Slezak, M. Soffel, D. Sosnowska, V. Straižys, M. ter Linden, D. Terrell, S. Theil, C. Tiede, L. Troisi, P. Tsalmantza, D. Tur, M. Vaccari, F. Vachier, P. Valles, W. Van Hamme, L. Veltz, J. Virtanen, J. M. Wallut, R. Wichmann, M. I. Wilkinson, H. Ziaeepour, and S. Zschocke. The Gaia mission. , 595: A1, Nov. 2016c. doi: 10.1051/0004-6361/201629272.

Gaia Collaboration, A. G. A. Brown, A. Vallenari, T. Prusti, J. H. J. de Bruijne, C. Babusiaux, C. A. L. Bailer-Jones, M. Biermann, D. W. Evans, L. Eyer, F. Jansen, C. Jordi, S. A. Klioner, U. Lammers, L. Lindegren, X. Luri, F. Mignard, C. Panem, D. Pourbaix, S. Randich, P. Sartoretti, H. I. Siddiqui, C. Soubiran, F. van Leeuwen, N. A. Walton, F. Arenou, U. Bastian, M. Cropper, R. Drimmel, D. Katz, M. G. Lattanzi, J. Bakker, C. Cacciari, J. Castañeda, L. Chaoul, N. Cheek, F. De Angeli, C. Fabricius, R. Guerra, B. Holl, E. Masana, R. Messineo, N. Mowlavi, K. Nienartowicz, P. Panuzzo, J. Portell, M. Riello, G. M. Seabroke, P. Tanga, F. Thévenin, G. Gracia-Abril, G. Comoretto, M. Garcia-Reinaldos, D. Teyssier, M. Altmann, R. Andrae, M. Audard, I. Bellas-Velidis, K. Benson, J. Berthier, R. Blomme, P. Burgess, G. Busso, B. Carry, A. Cellino, G. Clementini, M. Clotet, O. Creevey, M. Davidson, J. De Ridder, L. Delchambre, A. Dell'Oro, C. Ducourant, J. Fernández-Hernández, M. Fouesneau, Y. Frémat, L. Galluccio, M. García-Torres, J. González-Núñez, J. J. González-Vidal, E. Gosset, L. P. Guy, J. L. Halbwachs, N. C. Hambly, D. L. Harrison, J. Hernández, D. Hestroffer, S. T. Hodgkin, A. Hutton, G. Jasniewicz, A. Jean-Antoine-Piccolo, S. Jordan, A. J. Korn, A. Krone-Martins, A. C. Lanzafame, T. Lebzelter, W. Löffler, M. Manteiga, P. M. Marrese, J. M. Martín-Fleitas, A. Moitinho, A. Mora, K. Muinonen, J. Osinde, E. Pancino, T. Pauwels, J. M. Petit, A. Recio-Blanco, P. J. Richards, L. Rimoldini, A. C. Robin, L. M. Sarro, C. Siopis, M. Smith, A. Sozzetti, M. Süveges, J. Torra, W. van Reeven, U. Abbas, A. Abreu Aramburu, S. Accart, C. Aerts, G. Altavilla, M. A. Álvarez, R. Alvarez, J. Alves, R. I. Anderson, A. H. Andrei, E. Anglada Varela, E. Antiche, T. Antoja, B. Arcay, T. L. Astraatmadja, N. Bach, S. G. Baker, L. Balaguer-Núñez, P. Balm, C. Barache, C. Barata, D. Barbato, F. Barblan, P. S. Barklem, D. Barrado, M. Barros, M. A. Barstow, S. Bartholomé Muñoz, J. L. Bassilana, U. Becciani, M. Bellazzini, A. Berihuete, S. Bertone, L. Bianchi, O. Bienaymé, S. Blanco-Cuaresma, T. Boch, C. Boeche, A. Bombrun, R. Borrachero, D. Bossini, S. Bouquillon, G. Bourda,

A. Bragaglia, L. Bramante, M. A. Breddels, A. Bressan, N. Brouillet, T. Brüsemeister, E. Brugaletta, B. Bucciarelli, A. Burlacu, D. Busonero, A. G. Butkevich, R. Buzzi, E. Caffau, R. Cancelliere, G. Cannizzaro, T. Cantat-Gaudin, R. Carballo, T. Carlucci, J. M. Carrasco, L. Casamiquela, M. Castellani, A. Castro-Ginard, P. Charlot, L. Chemin, A. Chiavassa, G. Cocozza, G. Costigan, S. Cowell, F. Crifo, M. Crosta, C. Crowley, J. Cuypers, C. Dafonte, Y. Damerdji, A. Dapergolas, P. David, M. David, P. de Laverny, F. De Luise, R. De March, D. de Martino, R. de Souza, A. de Torres, J. Debosscher, E. del Pozo, M. Delbo, A. Delgado, H. E. Delgado, P. Di Matteo, S. Diakite, C. Diener, E. Distefano, C. Dolding, P. Drazinos, J. Durán, B. Edvardsson, H. Enke, K. Eriksson, P. Esquej, G. Eynard Bontemps, C. Fabre, M. Fabrizio, S. Faigler, A. J. Falcão, M. Farràs Casas, L. Federici, G. Fedorets, P. Fernique, F. Figueras, F. Filippi, K. Findeisen, A. Fonti, E. Fraile, M. Fraser, B. Frézouls, M. Gai, S. Galleti, D. Garabato, F. García-Sedano, A. Garofalo, N. Garralda, A. Gavel, P. Gavras, J. Gerssen, R. Geyer, P. Giacobbe, G. Gilmore, S. Girona, G. Giuffrida, F. Glass, M. Gomes, M. Granvik, A. Gueguen, A. Guerrier, J. Guiraud, R. Gutiérrez-Sánchez, R. Haigron, D. Hatzidimitriou, M. Hauser, M. Haywood, U. Heiter, A. Helmi, J. Heu, T. Hilger, D. Hobbs, W. Hofmann, G. Holland, H. E. Huckle, A. Hypki, V. Icardi, K. Janßen, G. Jevardat de Fombelle, P. G. Jonker, Á. L. Juhász, F. Julbe, A. Karampelas, A. Kewley, J. Klar, A. Kochoska, R. Kohley, K. Kolenberg, M. Kontizas, E. Kontizas, S. E. Koposov, G. Kordopatis, Z. Kostrzewa-Rutkowska, P. Koubsky, S. Lambert, A. F. Lanza, Y. Lasne, J. B. Lavigne, Y. Le Fustec, C. Le Poncin-Lafitte, Y. Lebreton, S. Leccia, N. Leclerc, I. Lecoeur-Taibi, H. Lenhardt, F. Leroux, S. Liao, E. Licata, H. E. P. Lindstrøm, T. A. Lister, E. Livanou, A. Lobel, M. López, S. Managau, R. G. Mann, G. Mantelet, O. Marchal, J. M. Marchant, M. Marconi, S. Marinoni, G. Marschalkó, D. J. Marshall, M. Martino, G. Marton, N. Mary, D. Massari, G. Matijevič, T. Mazeh, P. J. McMillan, S. Messina, D. Michalik, N. R. Millar, D. Molina, R. Molinaro, L. Molnár, P. Montegriffo, R. Mor, R. Morbidelli, T. Morel, D. Morris, A. F. Mulone, T. Muraveva, I. Musella, G. Nelemans, L. Nicastro, L. Noval, W. O'Mullane, C. Ordénovic, D. Ordóñez-Blanco, P. Osborne, C. Pagani, I. Pagano, F. Pailler, H. Palacin, L. Palaversa, A. Panahi, M. Pawlak, A. M. Piersimoni, F. X. Pineau, E. Plachy, G. Plum, E. Poggio, E. Poujoulet, A. Prša, L. Pulone, E. Racero, S. Ragaini, N. Rambaux, M. Ramos-Lerate, S. Regibo, C. Reylé, F. Riclet, V. Ripepi, A. Riva, A. Rivard, G. Rixon, T. Roegiers, M. Roelens, M. Romero-Gómez, N. Rowell, F. Royer, L. Ruiz-Dern, G. Sadowski, T. Sagristà Sellés, J. Sahlmann, J. Salgado, E. Salguero, N. Sanna, T. Santana-Ros, M. Sarasso, H. Savietto, M. Schultheis, E. Sciacca, M. Segol, J. C. Segovia, D. Ségransan, I. C. Shih, L. Siltala, A. F. Silva, R. L. Smart, K. W. Smith, E. Solano, F. Solitro, R. Sordo, S. Soria Nieto, J. Souchay, A. Spagna, F. Spoto, U. Stampa, I. A. Steele, H. Steidelmüller, C. A. Stephenson, H. Stoev, F. F. Suess, J. Surdej, L. Szabados, E. Szegedi-Elek, D. Tapiador, F. Taris, G. Tauran, M. B. Taylor, R. Teixeira, D. Terrett, P. Teyssandier, W. Thuillot, A. Titarenko, F. Torra Clotet, C. Turon, A. Ulla, E. Utrilla, S. Uzzi, M. Vaillant, G. Valentini, V. Valette, A. van Elteren, E. Van Hemelryck, M. van Leeuwen, M. Vaschetto, A. Vecchiato, J. Veljanoski, Y. Viala, D. Vicente, S. Vogt, C. von Essen, H. Voss, V. Votruba, S. Voutsinas, G. Walmsley, M. Weiler, O. Wertz, T. Wevers, Ł. Wyrzykowski, A. Yoldas, M. Žerjal, H. Ziaeepour, J. Zorec, S. Zschocke,

S. Zucker, C. Zurbach, and T. Zwitter. Gaia Data Release 2. Summary of the contents and survey properties. , 616:A1, Aug. 2018a. doi: 10.1051/0004-6361/201833051.

Gaia Collaboration, A. G. A. Brown, A. Vallenari, T. Prusti, J. H. J. de Bruijne, C. Babusiaux, C. A. L. Bailer-Jones, M. Biermann, D. W. Evans, L. Eyer, F. Jansen, C. Jordi, S. A. Klioner, U. Lammers, L. Lindegren, X. Luri, F. Mignard, C. Panem, D. Pourbaix, S. Randich, P. Sartoretti, H. I. Siddiqui, C. Soubiran, F. van Leeuwen, N. A. Walton, F. Arenou, U. Bastian, M. Cropper, R. Drimmel, D. Katz, M. G. Lattanzi, J. Bakker, C. Cacciari, J. Castañeda, L. Chaoul, N. Cheek, F. De Angeli, C. Fabricius, R. Guerra, B. Holl, E. Masana, R. Messineo, N. Mowlavi, K. Nienartowicz, P. Panuzzo, J. Portell, M. Riello, G. M. Seabroke, P. Tanga, F. Thévenin, G. Gracia-Abril, G. Comoretto, M. Garcia-Reinaldos, D. Teyssier, M. Altmann, R. Andrae, M. Audard, I. Bellas-Velidis, K. Benson, J. Berthier, R. Blomme, P. Burgess, G. Busso, B. Carry, A. Cellino, G. Clementini, M. Clotet, O. Creevey, M. Davidson, J. De Ridder, L. Delchambre, A. Dell'Oro, C. Ducourant, J. Fernández-Hernández, M. Fouesneau, Y. Frémat, L. Galluccio, M. García-Torres, J. González-Núñez, J. J. González-Vidal, E. Gosset, L. P. Guy, J. L. Halbwachs, N. C. Hambly, D. L. Harrison, J. Hernández, D. Hestroffer, S. T. Hodgkin, A. Hutton, G. Jasniewicz, A. Jean-Antoine-Piccolo, S. Jordan, A. J. Korn, A. Krone-Martins, A. C. Lanzafame, T. Lebzelter, W. Löffler, M. Manteiga, P. M. Marrese, J. M. Martín-Fleitas, A. Moitinho, A. Mora, K. Muinonen, J. Osinde, E. Pancino, T. Pauwels, J. M. Petit, A. Recio-Blanco, P. J. Richards, L. Rimoldini, A. C. Robin, L. M. Sarro, C. Siopis, M. Smith, A. Sozzetti, M. Süveges, J. Torra, W. van Reeven, U. Abbas, A. Abreu Aramburu, S. Accart, C. Aerts, G. Altavilla, M. A. Álvarez, R. Alvarez, J. Alves, R. I. Anderson, A. H. Andrei, E. Anglada Varela, E. Antiche, T. Antoja, B. Arcay, T. L. Astraatmadja, N. Bach, S. G. Baker, L. Balaguer-Núñez, P. Balm, C. Barache, C. Barata, D. Barbato, F. Barblan, P. S. Barklem, D. Barrado, M. Barros, M. A. Barstow, S. Bartholomé Muñoz, J. L. Bassilana, U. Becciani, M. Bellazzini, A. Berihuete, S. Bertone, L. Bianchi, O. Bienaymé, S. Blanco-Cuaresma, T. Boch, C. Boeche, A. Bombrun, R. Borrachero, D. Bossini, S. Bouquillon, G. Bourda, A. Bragaglia, L. Bramante, M. A. Breddels, A. Bressan, N. Brouillet, T. Brüsemeister, E. Brugaletta, B. Bucciarelli, A. Burlacu, D. Busonero, A. G. Butkevich, R. Buzzi, E. Caffau, R. Cancelliere, G. Cannizzaro, T. Cantat-Gaudin, R. Carballo, T. Carlucci, J. M. Carrasco, L. Casamiquela, M. Castellani, A. Castro-Ginard, P. Charlot, L. Chemin, A. Chiavassa, G. Cocozza, G. Costigan, S. Cowell, F. Crifo, M. Crosta, C. Crowley, J. Cuypers, C. Dafonte, Y. Damerdji, A. Dapergolas, P. David, M. David, P. de Laverny, F. De Luise, R. De March, D. de Martino, R. de Souza, A. de Torres, J. Debosscher, E. del Pozo, M. Delbo, A. Delgado, H. E. Delgado, P. Di Matteo, S. Diakite, C. Diener, E. Distefano, C. Dolding, P. Drazinos, J. Durán, B. Edvardsson, H. Enke, K. Eriksson, P. Esquej, G. Eynard Bontemps, C. Fabre, M. Fabrizio, S. Faigler, A. J. Falcão, M. Farràs Casas, L. Federici, G. Fedorets, P. Fernique, F. Figueras, F. Filippi, K. Findeisen, A. Fonti, E. Fraile, M. Fraser, B. Frézouls, M. Gai, S. Galleti, D. Garabato, F. García-Sedano, A. Garofalo, N. Garralda, A. Gavel, P. Gavras, J. Gerssen, R. Geyer, P. Giacobbe, G. Gilmore, S. Girona, G. Giuffrida, F. Glass, M. Gomes, M. Granvik, A. Gueguen,

A. Guerrier, J. Guiraud, R. Gutiérrez-Sánchez, R. Haigron, D. Hatzidimitriou, M. Hauser, M. Haywood, U. Heiter, A. Helmi, J. Heu, T. Hilger, D. Hobbs, W. Hofmann, G. Holland, H. E. Huckle, A. Hypki, V. Icardi, K. Janßen, G. Jevardat de Fombelle, P. G. Jonker, Á. L. Juhász, F. Julbe, A. Karampelas, A. Kewley, J. Klar, A. Kochoska, R. Kohley, K. Kolenberg, M. Kontizas, E. Kontizas, S. E. Koposov, G. Kordopatis, Z. Kostrzewa-Rutkowska, P. Koubsky, S. Lambert, A. F. Lanza, Y. Lasne, J. B. Lavigne, Y. Le Fustec, C. Le Poncin-Lafitte, Y. Lebreton, S. Leccia, N. Leclerc, I. Lecoeur-Taibi, H. Lenhardt, F. Leroux, S. Liao, E. Licata, H. E. P. Lindstrøm, T. A. Lister, E. Livanou, A. Lobel, M. López, S. Managau, R. G. Mann, G. Mantelet, O. Marchal, J. M. Marchant, M. Marconi, S. Marinoni, G. Marschalkó, D. J. Marshall, M. Martino, G. Marton, N. Mary, D. Massari, G. Matijevič, T. Mazeh, P. J. McMillan, S. Messina, D. Michalik, N. R. Millar, D. Molina, R. Molinaro, L. Molnár, P. Montegriffo, R. Mor, R. Morbidelli, T. Morel, D. Morris, A. F. Mulone, T. Muraveva, I. Musella, G. Nelemans, L. Nicastro, L. Noval, W. O'Mullane, C. Ordénovic, D. Ordóñez-Blanco, P. Osborne, C. Pagani, I. Pagano, F. Pailler, H. Palacin, L. Palaversa, A. Panahi, M. Pawlak, A. M. Piersimoni, F. X. Pineau, E. Plachy, G. Plum, E. Poggio, E. Poujoulet, A. Prša, L. Pulone, E. Racero, S. Ragaini, N. Rambaux, M. Ramos-Lerate, S. Regibo, C. Reylé, F. Riclet, V. Ripepi, A. Riva, A. Rivard, G. Rixon, T. Roegiers, M. Roelens, M. Romero-Gómez, N. Rowell, F. Royer, L. Ruiz-Dern, G. Sadowski, T. Sagristà Sellés, J. Sahlmann, J. Salgado, E. Salguero, N. Sanna, T. Santana-Ros, M. Sarasso, H. Savietto, M. Schultheis, E. Sciacca, M. Segol, J. C. Segovia, D. Ségransan, I. C. Shih, L. Siltala, A. F. Silva, R. L. Smart, K. W. Smith, E. Solano, F. Solitro, R. Sordo, S. Soria Nieto, J. Souchay, A. Spagna, F. Spoto, U. Stampa, I. A. Steele, H. Steidelmüller, C. A. Stephenson, H. Stoev, F. F. Suess, J. Surdej, L. Szabados, E. Szegedi-Elek, D. Tapiador, F. Taris, G. Tauran, M. B. Taylor, R. Teixeira, D. Terrett, P. Teyssandier, W. Thuillot, A. Titarenko, F. Torra Clotet, C. Turon, A. Ulla, E. Utrilla, S. Uzzi, M. Vaillant, G. Valentini, V. Valette, A. van Elteren, E. Van Hemelryck, M. van Leeuwen, M. Vaschetto, A. Vecchiato, J. Veljanoski, Y. Viala, D. Vicente, S. Vogt, C. von Essen, H. Voss, V. Votruba, S. Voutsinas, G. Walmsley, M. Weiler, O. Wertz, T. Wevers, Ł. Wyrzykowski, A. Yoldas, M. Žerjal, H. Ziaeepour, J. Zorec, S. Zschocke, S. Zucker, C. Zurbach, and T. Zwitter. Gaia Data Release 2. Summary of the contents and survey properties. , 616:A1, Aug. 2018b. doi: 10.1051/0004-6361/201833051.

Gaia Collaboration, A. G. A. Brown, A. Vallenari, T. Prusti, J. H. J. de Bruijne, C. Babusiaux, M. Biermann, O. L. Creevey, D. W. Evans, L. Eyer, A. Hutton, F. Jansen, C. Jordi, S. A. Klioner, U. Lammers, L. Lindegren, X. Luri, F. Mignard, C. Panem, D. Pourbaix, S. Randich, P. Sartoretti, C. Soubiran, N. A. Walton, F. Arenou, C. A. L. Bailer-Jones, U. Bastian, M. Cropper, R. Drimmel, D. Katz, M. G. Lattanzi, F. van Leeuwen, J. Bakker, C. Cacciari, J. Castañeda, F. De Angeli, C. Ducourant, C. Fabricius, M. Fouesneau, Y. Frémat, R. Guerra, A. Guerrier, J. Guiraud, A. Jean-Antoine Piccolo, E. Masana, R. Messineo, N. Mowlavi, C. Nicolas, K. Nienartowicz, F. Pailler, P. Panuzzo, F. Riclet, W. Roux, G. M. Seabroke, R. Sordo, P. Tanga, F. Thévenin, G. Gracia-Abril, J. Portell, D. Teyssier, M. Altmann, R. Andrae, I. Bellas-Velidis, K. Benson, J. Berthier, R. Blomme, E. Brugaletta, P. W. Burgess, G. Busso,

B. Carry, A. Cellino, N. Cheek, G. Clementini, Y. Damerdji, M. Davidson, L. Delchambre, A. Dell'Oro, J. Fernández-Hernández, L. Galluccio, P. García-Lario, M. Garcia-Reinaldos, J. González-Núñez, E. Gosset, R. Haigron, J. L. Halbwachs, N. C. Hambly, D. L. Harrison, D. Hatzidimitriou, U. Heiter, J. Hernández, D. Hestroffer, S. T. Hodgkin, B. Holl, K. Janßen, G. Jevardat de Fombelle, S. Jordan, A. Krone-Martins, A. C. Lanzafame, W. Löffler, A. Lorca, M. Manteiga, O. Marchal, P. M. Marrese, A. Moitinho, A. Mora, K. Muinonen, P. Osborne, E. Pancino, T. Pauwels, J. M. Petit, A. Recio-Blanco, P. J. Richards, M. Riello, L. Rimoldini, A. C. Robin, T. Roegiers, J. Rybizki, L. M. Sarro, C. Siopis, M. Smith, A. Sozzetti, A. Ulla, E. Utrilla, M. van Leeuwen, W. van Reeven, U. Abbas, A. Abreu Aramburu, S. Accart, C. Aerts, J. J. Aguado, M. Ajaj, G. Altavilla, M. A. Álvarez, J. Álvarez Cid-Fuentes, J. Alves, R. I. Anderson, E. Anglada Varela, T. Antoja, M. Audard, D. Baines, S. G. Baker, L. Balaguer-Núñez, E. Balbinot, Z. Balog, C. Barache, D. Barbato, M. Barros, M. A. Barstow, S. Bartolomé, J. L. Bassilana, N. Bauchet, A. Baudesson-Stella, U. Becciani, M. Bellazzini, M. Bernet, S. Bertone, L. Bianchi, S. Blanco-Cuaresma, T. Boch, A. Bombrun, D. Bossini, S. Bouquillon, A. Bragaglia, L. Bramante, E. Breedt, A. Bressan, N. Brouillet, B. Bucciarelli, A. Burlacu, D. Busonero, A. G. Butkevich, R. Buzzi, E. Caffau, R. Cancelliere, H. Cánovas, T. Cantat-Gaudin, R. Carballo, T. Carlucci, M. I. Carnerero, J. M. Carrasco, L. Casamiquela, M. Castellani, A. Castro-Ginard, P. Castro Sampol, L. Chaoul, P. Charlot, L. Chemin, A. Chiavassa, M. R. L. Cioni, G. Comoretto, W. J. Cooper, T. Cornez, S. Cowell, F. Crifo, M. Crosta, C. Crowley, C. Dafonte, A. Dapergolas, M. David, P. David, P. de Laverny, F. De Luise, R. De March, J. De Ridder, R. de Souza, P. de Teodoro, A. de Torres, E. F. del Peloso, E. del Pozo, M. Delbo, A. Delgado, H. E. Delgado, J. B. Delisle, P. Di Matteo, S. Diakite, C. Diener, E. Distefano, C. Dolding, D. Eappachen, B. Edvardsson, H. Enke, P. Esquej, C. Fabre, M. Fabrizio, S. Faigler, G. Fedorets, P. Fernique, A. Fienga, F. Figueras, C. Fouron, F. Fragkoudi, E. Fraile, F. Franke, M. Gai, D. Garabato, A. Garcia-Gutierrez, M. García-Torres, A. Garofalo, P. Gavras, E. Gerlach, R. Geyer, P. Giacobbe, G. Gilmore, S. Girona, G. Giuffrida, R. Gomel, A. Gomez, I. Gonzalez-Santamaria, J. J. González-Vidal, M. Granvik, R. Gutiérrez-Sánchez, L. P. Guy, M. Hauser, M. Haywood, A. Helmi, S. L. Hidalgo, T. Hilger, N. Hładczuk, D. Hobbs, G. Holland, H. E. Huckle, G. Jasniewicz, P. G. Jonker, J. Juaristi Campillo, F. Julbe, L. Karbevska, P. Kervella, S. Khanna, A. Kochoska, M. Kontizas, G. Kordopatis, A. J. Korn, Z. Kostrzewa-Rutkowska, K. Kruszyńska, S. Lambert, A. F. Lanza, Y. Lasne, J. F. Le Campion, Y. Le Fustec, Y. Lebreton, T. Lebzelter, S. Leccia, N. Leclerc, I. Lecoeur-Taibi, S. Liao, E. Licata, E. P. Lindstrøm, T. A. Lister, E. Livanou, A. Lobel, P. Madrero Pardo, S. Managau, R. G. Mann, J. M. Marchant, M. Marconi, M. M. S. Marcos Santos, S. Marinoni, F. Marocco, D. J. Marshall, L. Martin Polo, J. M. Martín-Fleitas, A. Masip, D. Massari, A. Mastrobuono-Battisti, T. Mazeh, P. J. McMillan, S. Messina, D. Michalik, N. R. Millar, A. Mints, D. Molina, R. Molinaro, L. Molnár, P. Montegriffo, R. Mor, R. Morbidelli, T. Morel, D. Morris, A. F. Mulone, D. Munoz, T. Muraveva, C. P. Murphy, I. Musella, L. Noval, C. Ordénovic, G. Orrù, J. Osinde, C. Pagani, I. Pagano, L. Palaversa, P. A. Palicio, A. Panahi, M. Pawlak, X. Peñalosa Esteller, A. Penttilä, A. M. Piersimoni, F. X. Pineau, E. Plachy, G. Plum, E. Poggio, E. Poretti, E. Poujoulet, A. Prša, L. Pulone,

E. Racero, S. Ragaini, M. Rainer, C. M. Raiteri, N. Rambaux, P. Ramos, M. Ramos-Lerate, P. Re Fiorentin, S. Regibo, C. Reylé, V. Ripepi, A. Riva, G. Rixon, N. Robichon, C. Robin, M. Roelens, L. Rohrbasser, M. Romero-Gómez, N. Rowell, F. Royer, K. A. Rybicki, G. Sadowski, A. Sagristà Sellés, J. Sahlmann, J. Salgado, E. Salguero, N. Samaras, V. Sanchez Gimenez, N. Sanna, R. Santoveña, M. Sarasso, M. Schultheis, E. Sciacca, M. Segol, J. C. Segovia, D. Ségransan, D. Semeux, S. Shahaf, H. I. Siddiqui, A. Siebert, L. Siltala, E. Slezak, R. L. Smart, E. Solano, F. Solitro, D. Souami, J. Souchay, A. Spagna, F. Spoto, I. A. Steele, H. Steidelmüller, C. A. Stephenson, M. Süveges, L. Szabados, E. Szegedi-Elek, F. Taris, G. Tauran, M. B. Taylor, R. Teixeira, W. Thuillot, N. Tonello, F. Torra, J. Torra, C. Turon, N. Unger, M. Vaillant, E. van Dillen, O. Vanel, A. Vecchiato, Y. Viala, D. Vicente, S. Voutsinas, M. Weiler, T. Wevers, Ł. Wyrzykowski, A. Yoldas, P. Yvard, H. Zhao, J. Zorec, S. Zucker, C. Zurbach, and T. Zwitter. Gaia Early Data Release 3. Summary of the contents and survey properties. , 649:A1, May 2021. doi: 10.1051/0004-6361/202039657.

Gaia Collaboration, L. Galluccio, M. Delbo, F. De Angeli, T. Pauwels, P. Tanga, F. Mignard, A. Cellino, A. G. A. Brown, K. Muinonen, A. Penttilä, S. Jordan, A. Vallenari, T. Prusti, J. H. J. de Bruijne, F. Arenou, C. Babusiaux, M. Biermann, O. L. Creevey, C. Ducourant, D. W. Evans, L. Eyer, R. Guerra, A. Hutton, C. Jordi, S. A. Klioner, U. L. Lammers, L. Lindegren, X. Luri, C. Panem, D. Pourbaix, S. Randich, P. Sartoretti, C. Soubiran, N. A. Walton, C. A. L. Bailer-Jones, U. Bastian, R. Drimmel, F. Jansen, D. Katz, M. G. Lattanzi, F. van Leeuwen, J. Bakker, C. Cacciari, J. Castañeda, C. Fabricius, M. Fouesneau, Y. Frémat, A. Guerrier, U. Heiter, E. Masana, R. Messineo, N. Mowlavi, C. Nicolas, K. Nienartowicz, F. Pailler, P. Panuzzo, F. Riclet, W. Roux, G. M. Seabroke, R. Sordo, F. Thévenin, G. Gracia-Abril, J. Portell, D. Teyssier, M. Altmann, R. Andrae, M. Audard, I. Bellas-Velidis, K. Benson, J. Berthier, R. Blomme, P. W. Burgess, D. Busonero, G. Busso, H. Cánovas, B. Carry, N. Cheek, G. Clementini, Y. Damerdji, M. Davidson, P. de Teodoro, M. Nuñez Campos, L. Delchambre, A. Dell'Oro, P. Esquej, J. Fernández-Hernández, E. Fraile, D. Garabato, P. García-Lario, E. Gosset, R. Haigron, J. L. Halbwachs, N. C. Hambly, D. L. Harrison, J. Hernández, D. Hestroffer, S. T. Hodgkin, B. Holl, K. Janßen, G. Jevardat de Fombelle, A. Krone-Martins, A. C. Lanzafame, W. Löffler, O. Marchal, P. M. Marrese, A. Moitinho, P. Osborne, E. Pancino, A. Recio-Blanco, C. Reylé, M. Riello, L. Rimoldini, T. Roegiers, J. Rybizki, L. M. Sarro, C. Siopis, M. Smith, A. Sozzetti, E. Utrilla, M. van Leeuwen, U. Abbas, P. Ábrahám, A. Abreu Aramburu, C. Aerts, J. J. Aguado, M. Ajaj, F. Aldea-Montero, G. Altavilla, M. A. Álvarez, J. Alves, R. I. Anderson, E. Anglada Varela, T. Antoja, D. Baines, S. G. Baker, L. Balaguer-Núñez, E. Balbinot, Z. Balog, C. Barache, D. Barbato, M. Barros, M. A. Barstow, S. Bartolomé, J. L. Bassilana, N. Bauchet, U. Becciani, M. Bellazzini, A. Berihuete, M. Bernet, S. Bertone, L. Bianchi, A. Binnenfeld, S. Blanco-Cuaresma, T. Boch, A. Bombrun, D. Bossini, S. Bouquillon, A. Bragaglia, L. Bramante, E. Breedt, A. Bressan, N. Brouillet, E. Brugaletta, B. Bucciarelli, A. Burlacu, A. G. Butkevich, R. Buzzi, E. Caffau, R. Cancelliere, T. Cantat-Gaudin, R. Carballo, T. Carlucci, M. I. Carnerero, J. M. Carrasco, L. Casamiquela, M. Castellani, A. Castro-Ginard, L. Chaoul,

P. Charlot, L. Chemin, V. Chiaramida, A. Chiavassa, N. Chornay, G. Comoretto, G. Contursi, W. J. Cooper, T. Cornez, S. Cowell, F. Crifo, M. Cropper, M. Crosta, C. Crowley, C. Dafonte, A. Dapergolas, P. David, P. de Laverny, F. De Luise, R. De March, J. De Ridder, R. de Souza, A. de Torres, E. F. del Peloso, E. del Pozo, A. Delgado, J. B. Delisle, C. Demouchy, T. E. Dharmawardena, S. Diakite, C. Diener, E. Distefano, C. Dolding, H. Enke, C. Fabre, M. Fabrizio, S. Faigler, G. Fedorets, P. Fernique, F. Figueras, Y. Fournier, C. Fouron, F. Fragkoudi, M. Gai, A. Garcia-Gutierrez, M. Garcia-Reinaldos, M. García-Torres, A. Garofalo, A. Gavel, P. Gavras, E. Gerlach, R. Geyer, P. Giacobbe, G. Gilmore, S. Girona, G. Giuffrida, R. Gomel, A. Gomez, J. González-Núñez, I. González-Santamaría, J. J. González-Vidal, M. Granvik, P. Guillout, J. Guiraud, R. Gutiérrez-Sánchez, L. P. Guy, D. Hatzidimitriou, M. Hauser, M. Haywood, A. Helmer, A. Helmi, M. H. Sarmiento, S. L. Hidalgo, N. Hładczuk, D. Hobbs, G. Holland, H. E. Huckle, K. Jardine, G. Jasniewicz, A. Jean-Antoine Piccolo, Ó. Jiménez-Arranz, J. Juaristi Campillo, F. Julbe, L. Karbevska, P. Kervella, S. Khanna, G. Kordopatis, A. J. Korn, Á. Kóspál, Z. Kostrzewa-Rutkowska, K. Kruszyńska, M. Kun, P. Laizeau, S. Lambert, A. F. Lanza, Y. Lasne, J. F. Le Campion, Y. Lebreton, T. Lebzelter, S. Leccia, N. Leclerc, I. Lecoeur-Taibi, S. Liao, E. L. Licata, H. E. P. Lindstrøm, T. A. Lister, E. Livanou, A. Lobel, A. Lorca, C. Loup, P. Madrero Pardo, A. Magdaleno Romeo, S. Managau, R. G. Mann, M. Manteiga, J. M. Marchant, M. Marconi, J. Marcos, M. M. S. Marcos Santos, D. Marín Pina, S. Marinoni, F. Marocco, D. J. Marshall, L. Martin Polo, J. M. Martín-Fleitas, G. Marton, N. Mary, A. Masip, D. Massari, A. Mastrobuono-Battisti, T. Mazeh, P. J. McMillan, S. Messina, D. Michalik, N. R. Millar, A. Mints, D. Molina, R. Molinaro, L. Molnár, G. Monari, M. Monguió, P. Montegriffo, A. Montero, R. Mor, A. Mora, R. Morbidelli, T. Morel, D. Morris, T. Muraveva, C. P. Murphy, I. Musella, Z. Nagy, L. Noval, F. Ocaña, A. Ogden, C. Ordenovic, J. O. Osinde, C. Pagani, I. Pagano, L. Palaversa, P. A. Palicio, L. Pallas-Quintela, A. Panahi, S. Payne-Wardenaar, X. Peñalosa Esteller, J. M. Petit, B. Pichon, A. M. Piersimoni, F. X. Pineau, E. Plachy, G. Plum, E. Poggio, A. Prša, L. Pulone, E. Racero, S. Ragaini, M. Rainer, C. M. Raiteri, P. Ramos, M. Ramos-Lerate, P. Re Fiorentin, S. Regibo, P. J. Richards, C. Rios Diaz, V. Ripepi, A. Riva, H. W. Rix, G. Rixon, N. Robichon, A. C. Robin, C. Robin, M. Roelens, H. R. O. Rogues, L. Rohrbasser, M. Romero-Gómez, N. Rowell, F. Royer, D. Ruz Mieres, K. A. Rybicki, G. Sadowski, A. Sáez Núñez, A. Sagristà Sellés, J. Sahlmann, E. Salguero, N. Samaras, V. Sanchez Gimenez, N. Sanna, R. Santoveña, M. Sarasso, M. Schultheis, E. Sciacca, M. Segol, J. C. Segovia, D. Ségransan, D. Semeux, S. Shahaf, H. I. Siddiqui, A. Siebert, L. Siltala, A. Silvelo, E. Slezak, I. Slezak, R. L. Smart, O. N. Snaith, E. Solano, F. Solitro, D. Souami, J. Souchay, A. Spagna, L. Spina, F. Spoto, I. A. Steele, H. Steidelmüller, C. A. Stephenson, M. Süveges, J. Surdej, L. Szabados, E. Szegedi-Elek, F. Taris, M. B. Taylor, R. Teixeira, L. Tolomei, N. Tonello, F. Torra, J. Torra, G. Torralba Elipe, M. Trabucchi, A. T. Tsounis, C. Turon, A. Ulla, N. Unger, M. V. Vaillant, E. van Dillen, W. van Reeven, O. Vanel, A. Vecchiato, Y. Viala, D. Vicente, S. Voutsinas, M. Weiler, T. Wevers, Ł. Wyrzykowski, A. Yoldas, P. Yvard, H. Zhao, J. Zorec, S. Zucker, and T. Zwitter. Gaia Data Release 3. Reflectance spectra of Solar System small bodies. , 674:A35, June 2023a. doi: 10.1051/0004-6361/202243791.

Gaia Collaboration, P. Montegriffo, M. Bellazzini, F. De Angeli, R. Andrae, M. A. Barstow, D. Bossini, A. Bragaglia, P. W. Burgess, C. Cacciari, J. M. Carrasco, N. Chornay, L. Delchambre, D. W. Evans, M. Fouesneau, Y. Frémat, D. Garabato, C. Jordi, M. Manteiga, D. Massari, L. Palaversa, E. Pancino, M. Riello, D. Ruz Mieres, N. Sanna, R. Santoveña, R. Sordo, A. Vallenari, N. A. Walton, A. G. A. Brown, T. Prusti, J. H. J. de Bruijne, F. Arenou, C. Babusiaux, M. Biermann, O. L. Creevey, C. Ducourant, L. Eyer, R. Guerra, A. Hutton, S. A. Klioner, U. L. Lammers, L. Lindegren, X. Luri, F. Mignard, C. Panem, D. Pourbaix, S. Randich, P. Sartoretti, C. Soubiran, P. Tanga, C. A. L. Bailer-Jones, U. Bastian, R. Drimmel, F. Jansen, D. Katz, M. G. Lattanzi, F. van Leeuwen, J. Bakker, J. Castañeda, C. Fabricius, L. Galluccio, A. Guerrier, U. Heiter, E. Masana, R. Messineo, N. Mowlavi, C. Nicolas, K. Nienartowicz, F. Pailler, P. Panuzzo, F. Riclet, W. Roux, G. M. Seabroke, F. Thévenin, G. Gracia-Abril, J. Portell, D. Teyssier, M. Altmann, M. Audard, I. Bellas-Velidis, K. Benson, J. Berthier, R. Blomme, D. Busonero, G. Busso, H. Cánovas, B. Carry, A. Cellino, N. Cheek, G. Clementini, Y. Damerdji, M. Davidson, P. de Teodoro, M. Nuñez Campos, A. Dell'Oro, P. Esquej, J. Fernández-Hernández, E. Fraile, P. García-Lario, E. Gosset, R. Haigron, J. L. Halbwachs, N. C. Hambly, D. L. Harrison, J. Hernández, D. Hestroffer, S. T. Hodgkin, B. Holl, K. Janßen, G. Jevardat de Fombelle, S. Jordan, A. Krone-Martins, A. C. Lanzafame, W. Löffler, O. Marchal, P. M. Marrese, A. Moitinho, K. Muinonen, P. Osborne, T. Pauwels, A. Recio-Blanco, C. Reylé, L. Rimoldini, T. Roegiers, J. Rybizki, L. M. Sarro, C. Siopis, M. Smith, A. Sozzetti, E. Utrilla, M. van Leeuwen, U. Abbas, P. Ábrahám, A. Abreu Aramburu, C. Aerts, J. J. Aguado, M. Ajaj, F. Aldea-Montero, G. Altavilla, M. A. Álvarez, J. Alves, R. I. Anderson, E. Anglada Varela, T. Antoja, D. Baines, S. G. Baker, L. Balaguer-Núñez, E. Balbinot, Z. Balog, C. Barache, D. Barbato, M. Barros, S. Bartolomé, J. L. Bassilana, N. Bauchet, U. Becciani, A. Berihuete, M. Bernet, S. Bertone, L. Bianchi, A. Binnenfeld, S. Blanco-Cuaresma, T. Boch, A. Bombrun, S. Bouquillon, L. Bramante, E. Breedt, A. Bressan, N. Brouillet, E. Brugaletta, B. Bucciarelli, A. Burlacu, A. G. Butkevich, R. Buzzi, E. Caffau, R. Cancelliere, T. Cantat-Gaudin, R. Carballo, T. Carlucci, M. I. Carnerero, L. Casamiquela, M. Castellani, A. Castro-Ginard, L. Chaoul, P. Charlot, L. Chemin, V. Chiaramida, A. Chiavassa, G. Comoretto, G. Contursi, W. J. Cooper, T. Cornez, S. Cowell, F. Crifo, M. Cropper, M. Crosta, C. Crowley, C. Dafonte, A. Dapergolas, P. David, P. de Laverny, F. De Luise, R. De March, J. De Ridder, R. de Souza, A. de Torres, E. F. del Peloso, E. del Pozo, M. Delbo, A. Delgado, J. B. Delisle, C. Demouchy, T. E. Dharmawardena, S. Diakite, C. Diener, E. Distefano, C. Dolding, H. Enke, C. Fabre, M. Fabrizio, S. Faigler, G. Fedorets, P. Fernique, F. Figueras, Y. Fournier, C. Fouron, F. Fragkoudi, M. Gai, A. Garcia-Gutierrez, M. Garcia-Reinaldos, M. García-Torres, A. Garofalo, A. Gavel, P. Gavras, E. Gerlach, R. Geyer, P. Giacobbe, G. Gilmore, S. Girona, G. Giuffrida, R. Gomel, A. Gomez, J. González-Núñez, I. González-Santamaría, J. J. González-Vidal, M. Granvik, P. Guillout, J. Guiraud, R. Gutiérrez-Sánchez, L. P. Guy, D. Hatzidimitriou, M. Hauser, M. Haywood, A. Helmer, A. Helmi, M. H. Sarmiento, S. L. Hidalgo, N. Hładczuk, D. Hobbs, G. Holland, H. E. Huckle, K. Jardine, G. Jasniewicz, A. Jean-Antoine Piccolo, Ó. Jiménez-Arranz, J. Juaristi Campillo, F. Julbe, L. Karbevska, P. Kervella, S. Khanna, G. Kordopatis, A. J. Korn, Á. Kóspál, Z. Kostrzewa-Rutkowska, K. Kruszyńska, M. Kun, P. Laizeau, S. Lambert, A. F. Lanza, Y. Lasne, J. F. Le Campion, Y. Lebreton, T. Lebzelter, S. Leccia, N. Leclerc, I. Lecoeur-Taibi, S. Liao, E. L. Licata, H. E. P. Lindstróm, T. A. Lister, E. Livanou, A. Lobel, A. Lorca, C. Loup, P. Madrero Pardo, A. Magdaleno Romeo, S. Managau, R. G. Mann, J. M. Marchant, M. Marconi, J. Marcos, M. M. S. Marcos Santos, D. Marín Pina, S. Marinoni, F. Marocco, D. J. Marshall, L. Martin Polo, J. M. Martín-Fleitas, G. Marton, N. Mary, A. Masip, A. Mastrobuono-Battisti, T. Mazeh, P. J. McMillan, S. Messina, D. Michalik, N. R. Millar, A. Mints, D. Molina, R. Molinaro, L. Molnár, G. Monari, M. Monguió, A. Montero, R. Mor, A. Mora, R. Morbidelli, T. Morel, D. Morris, T. Muraveva, C. P. Murphy, I. Musella, Z. Nagy, L. Noval, F. Ocaña, A. Ogden, C. Ordenovic, J. O. Osinde, C. Pagani, I. Pagano, P. A. Palicio, L. Pallas-Quintela, A. Panahi, S. Payne-Wardenaar, X. Peñalosa Esteller, A. Penttilä, B. Pichon, A. M. Piersimoni, F. X. Pineau, E. Plachy, G. Plum, E. Poggio, A. Prša, L. Pulone, E. Racero, S. Ragaini, M. Rainer, C. M. Raiteri, P. Ramos, M. Ramos-Lerate, P. Re Fiorentin, S. Regibo, P. J. Richards, C. Rios Diaz, V. Ripepi, A. Riva, H. W. Rix, G. Rixon, N. Robichon, A. C. Robin, C. Robin, M. Roelens, H. R. O. Rogues, L. Rohrbasser, M. Romero-Gómez, N. Rowell, F. Royer, K. A. Rybicki, G. Sadowski, A. Sáez Núñez, A. Sagristà Sellés, J. Sahlmann, E. Salguero, N. Samaras, V. Sanchez Gimenez, M. Sarasso, M. S. Schultheis, E. Sciacca, M. Segol, J. C. Segovia, D. Ségransan, D. Semeux, S. Shahaf, H. I. Siddiqui, A. Siebert, L. Siltala, A. Silvelo, E. Slezak, I. Slezak, R. L. Smart, O. N. Snaith, E. Solano, F. Solitro, D. Souami, J. Souchay, A. Spagna, L. Spina, F. Spoto, I. A. Steele, H. Steidelmüller, C. A. Stephenson, M. Süveges, J. Surdej, L. Szabados, E. Szegedi-Elek, F. Taris, M. B. Taylor, R. Teixeira, L. Tolomei, N. Tonello, F. Torra, J. Torra, G. Torralba Elipe, M. Trabucchi, A. T. Tsounis, C. Turon, A. Ulla, N. Unger, M. V. Vaillant, E. van Dillen, W. van Reeven, O. Vanel, A. Vecchiato, Y. Viala, D. Vicente, S. Voutsinas, T. Wevers, Ł. Wyrzykowski, A. Yoldas, P. Yvard, H. Zhao, J. Zorec, S. Zucker, and T. Zwitter. Gaia Data Release 3. The Galaxy in your preferred colours: Synthetic photometry from Gaia low-resolution spectra. , 674:A33, June 2023b. doi: 10.1051/0004-6361/202243709.

Gaia Collaboration, A. Vallenari, A. G. A. Brown, T. Prusti, J. H. J. de Bruijne, F. Arenou, C. Babusiaux, M. Biermann, O. L. Creevey, C. Ducourant, D. W. Evans, L. Eyer, R. Guerra, A. Hutton, C. Jordi, S. A. Klioner, U. L. Lammers, L. Lindegren, X. Luri, F. Mignard, C. Panem, D. Pourbaix, S. Randich, P. Sartoretti, C. Soubiran, P. Tanga, N. A. Walton, C. A. L. Bailer-Jones, U. Bastian, R. Drimmel, F. Jansen, D. Katz, M. G. Lattanzi, F. van Leeuwen, J. Bakker, C. Cacciari, J. Castañeda, F. De Angeli, C. Fabricius, M. Fouesneau, Y. Frémat, L. Galluccio, A. Guerrier, U. Heiter, E. Masana, R. Messineo, N. Mowlavi, C. Nicolas, K. Nienartowicz, F. Pailler, P. Panuzzo, F. Riclet, W. Roux, G. M. Seabroke, R. Sordo, F. Thévenin, G. Gracia-Abril, J. Portell, D. Teyssier, M. Altmann, R. Andrae, M. Audard, I. Bellas-Velidis, K. Benson, J. Berthier, R. Blomme, P. W. Burgess, D. Busonero, G. Busso, H. Cánovas, B. Carry, A. Cellino, N. Cheek, G. Clementini, Y. Damerdji, M. Davidson, P. de Teodoro, M. Nuñez Campos, L. Delchambre, A. Dell'Oro, P. Esquej, J. Fernández-Hernández, E. Fraile, D. Garabato,

P. García-Lario, E. Gosset, R. Haigron, J. L. Halbwachs, N. C. Hambly, D. L. Harrison, J. Hernández, D. Hestroffer, S. T. Hodgkin, B. Holl, K. Janßen, G. Jevardat de Fombelle, S. Jordan, A. Krone-Martins, A. C. Lanzafame, W. Löffler, O. Marchal, P. M. Marrese, A. Moitinho, K. Muinonen, P. Osborne, E. Pancino, T. Pauwels, A. Recio-Blanco, C. Reylé, M. Riello, L. Rimoldini, T. Roegiers, J. Rybizki, L. M. Sarro, C. Siopis, M. Smith, A. Sozzetti, E. Utrilla, M. van Leeuwen, U. Abbas, P. Ábrahám, A. Abreu Aramburu, C. Aerts, J. J. Aguado, M. Ajaj, F. Aldea-Montero, G. Altavilla, M. A. Álvarez, J. Alves, F. Anders, R. I. Anderson, E. Anglada Varela, T. Antoja, D. Baines, S. G. Baker, L. Balaguer-Núñez, E. Balbinot, Z. Balog, C. Barache, D. Barbato, M. Barros, M. A. Barstow, S. Bartolomé, J. L. Bassilana, N. Bauchet, U. Becciani, M. Bellazzini, A. Berihuete, M. Bernet, S. Bertone, L. Bianchi, A. Binnenfeld, S. Blanco-Cuaresma, A. Blazere, T. Boch, A. Bombrun, D. Bossini, S. Bouquillon, A. Bragaglia, L. Bramante, E. Breedt, A. Bressan, N. Brouillet, E. Brugaletta, B. Bucciarelli, A. Burlacu, A. G. Butkevich, R. Buzzi, E. Caffau, R. Cancelliere, T. Cantat-Gaudin, R. Carballo, T. Carlucci, M. I. Carnerero, J. M. Carrasco, L. Casamiquela, M. Castellani, A. Castro-Ginard, L. Chaoul, P. Charlot, L. Chemin, V. Chiaramida, A. Chiavassa, N. Chornay, G. Comoretto, G. Contursi, W. J. Cooper, T. Cornez, S. Cowell, F. Crifo, M. Cropper, M. Crosta, C. Crowley, C. Dafonte, A. Dapergolas, M. David, P. David, P. de Laverny, F. De Luise, R. De March, J. De Ridder, R. de Souza, A. de Torres, E. F. del Peloso, E. del Pozo, M. Delbo, A. Delgado, J. B. Delisle, C. Demouchy, T. E. Dharmawardena, P. Di Matteo, S. Diakite, C. Diener, E. Distefano, C. Dolding, B. Edvardsson, H. Enke, C. Fabre, M. Fabrizio, S. Faigler, G. Fedorets, P. Fernique, A. Fienga, F. Figueras, Y. Fournier, C. Fouron, F. Fragkoudi, M. Gai, A. Garcia-Gutierrez, M. Garcia-Reinaldos, M. García-Torres, A. Garofalo, A. Gavel, P. Gavras, E. Gerlach, R. Geyer, P. Giacobbe, G. Gilmore, S. Girona, G. Giuffrida, R. Gomel, A. Gomez, J. González-Núñez, I. González-Santamaría, J. J. González-Vidal, M. Granvik, P. Guillout, J. Guiraud, R. Gutiérrez-Sánchez, L. P. Guy, D. Hatzidimitriou, M. Hauser, M. Haywood, A. Helmer, A. Helmi, M. H. Sarmiento, S. L. Hidalgo, T. Hilger, N. Hładczuk, D. Hobbs, G. Holland, H. E. Huckle, K. Jardine, G. Jasniewicz, A. Jean-Antoine Piccolo, Ó. Jiménez-Arranz, A. Jorissen, J. Juaristi Campillo, F. Julbe, L. Karbevska, P. Kervella, S. Khanna, M. Kontizas, G. Kordopatis, A. J. Korn, Á. Kóspál, Z. Kostrzewa-Rutkowska, K. Kruszyńska, M. Kun, P. Laizeau, S. Lambert, A. F. Lanza, Y. Lasne, J. F. Le Campion, Y. Lebreton, T. Lebzelter, S. Leccia, N. Leclerc, I. Lecoeur-Taibi, S. Liao, E. L. Licata, H. E. P. Lindstrøm, T. A. Lister, E. Livanou, A. Lobel, A. Lorca, C. Loup, P. Madrero Pardo, A. Magdaleno Romeo, S. Managau, R. G. Mann, M. Manteiga, J. M. Marchant, M. Marconi, J. Marcos, M. M. S. Marcos Santos, D. Marín Pina, S. Marinoni, F. Marocco, D. J. Marshall, L. Martin Polo, J. M. Martín-Fleitas, G. Marton, N. Mary, A. Masip, D. Massari, A. Mastrobuono-Battisti, T. Mazeh, P. J. McMillan, S. Messina, D. Michalik, N. R. Millar, A. Mints, D. Molina, R. Molinaro, L. Molnár, G. Monari, M. Monguió, P. Montegriffo, A. Montero, R. Mor, A. Mora, R. Morbidelli, T. Morel, D. Morris, T. Muraveva, C. P. Murphy, I. Musella, Z. Nagy, L. Noval, F. Ocaña, A. Ogden, C. Ordenovic, J. O. Osinde, C. Pagani, I. Pagano, L. Palaversa, P. A. Palicio, L. Pallas-Quintela, A. Panahi, S. Payne-Wardenaar, X. Peñalosa Esteller, A. Penttilä, B. Pichon, A. M. Piersimoni, F. X. Pineau, E. Plachy,

G. Plum, E. Poggio, A. Prša, L. Pulone, E. Racero, S. Ragaini, M. Rainer, C. M. Raiteri, N. Rambaux, P. Ramos, M. Ramos-Lerate, P. Re Fiorentin, S. Regibo, P. J. Richards, C. Rios Diaz, V. Ripepi, A. Riva, H. W. Rix, G. Rixon, N. Robichon, A. C. Robin, C. Robin, M. Roelens, H. R. O. Rogues, L. Rohrbasser, M. Romero-Gómez, N. Rowell, F. Royer, D. Ruz Mieres, K. A. Rybicki, G. Sadowski, A. Sáez Núñez, A. Sagristà Sellés, J. Sahlmann, E. Salguero, N. Samaras, V. Sanchez Gimenez, N. Sanna, R. Santoveña, M. Sarasso, M. Schultheis, E. Sciacca, M. Segol, J. C. Segovia, D. Ségransan, D. Semeux, S. Shahaf, H. I. Siddiqui, A. Siebert, L. Siltala, A. Silvelo, E. Slezak, I. Slezak, R. L. Smart, O. N. Snaith, E. Solano, F. Solitro, D. Souami, J. Souchay, A. Spagna, L. Spina, F. Spoto, I. A. Steele, H. Steidelmüller, C. A. Stephenson, M. Süveges, J. Surdej, L. Szabados, E. Szegedi-Elek, F. Taris, M. B. Taylor, R. Teixeira, L. Tolomei, N. Tonello, F. Torra, J. Torra, G. Torralba Elipe, M. Trabucchi, A. T. Tsounis, C. Turon, A. Ulla, N. Unger, M. V. Vaillant, E. van Dillen, W. van Reeven, O. Vanel, A. Vecchiato, Y. Viala, D. Vicente, S. Voutsinas, M. Weiler, T. Wevers, Ł. Wyrzykowski, A. Yoldas, P. Yvard, H. Zhao, J. Zorec, S. Zucker, and T. Zwitter. Gaia Data Release 3. Summary of the content and survey properties. , 674:A1, June 2023c. doi: 10.1051/0004-6361/202243940.

T. Gehrels. Scanning with charge-coupled devices. , 58(1):347–375, Dec. 1991. doi: 10.1007/BF01206004.

B. Gladman, D. Davis, C. Neese, R. Jedicke, G. Williams, J. Kavelaars, J. Petit, H. Scholl, M. Holman, B. Warrington, G. Esquerdo, and P. Tricarico. On the asteroid belt's orbital and size distribution. *Icarus*, 202:104–118, 2009.

K. M. Górski, E. Hivon, A. J. Banday, B. D. Wand elt, F. K. Hansen, M. Reinecke, and M. Bartelmann. HEALPix: A Framework for High-Resolution Discretization and Fast Analysis of Data Distributed on the Sphere. , 622(2):759–771, Apr. 2005. doi: 10.1086/427976.

B. Gray. Find_Orb: Orbit determination from observations. Astrophysics Source Code Library, record ascl:2202.016, Feb. 2022.

S. Greenstreet. Orbital dynamics of 2020 AV2: the first Vatira asteroid. *Monthly Notices of the Royal Astronomical Society: Letters*, 493(1):L129–L131, 02 2020. ISSN 1745-3925. doi: 10.1093/mnrasl/slaa025.

I. Groeneveld and G. P. Kuiper. Photometric Studies of Asteroids. I. , 120:200, Sept. 1954. doi: 10.1086/145904.

S. D. J. Gwyn, N. Hill, and J. J. Kavelaars. SSOS: A Moving-Object Image Search Tool for Asteroid Precovery. , 124(916):579, June 2012. doi: 10.1086/666462.

B. M. S. Hansen. Formation of the Terrestrial Planets from a Narrow Annulus. , 703(1):1131–1140, Sept. 2009. doi: 10.1088/0004-637X/703/1/1131.

S. Hasegawa, M. Marsset, F. E. DeMeo, S. J. Bus, M. Ishiguro, D. Kuroda, R. P. Binzel, J. Hanuš, A. M. Nakamura, B. Yang, and P. Vernazza. The Appearance of a “Fresh” Surface on 596 Scheila as a Consequence of the 2010 Impact Event. , 924(1):L9, Jan. 2022. doi: 10.3847/2041-8213/ac415a.

A. A. Henden, S. Levine, D. Terrell, and D. L. Welch. APASS - The Latest Data Release. In *American Astronomical Society Meeting Abstracts #225*, volume 225 of *American Astronomical Society Meeting Abstracts*, page 336.16, Jan. 2015.

P. Herget. The determination of orbits. , 44:153–161, Oct. 1935. doi: 10.1086/105293.

D. W. Hogg, G. D. Quinlan, and S. Tremaine. Dynamical Limits on Dark Mass in the Solar System. , 101:2274, June 1991. doi: 10.1086/115849.

M. J. Holman, M. J. Payne, P. Blankley, R. Janssen, and S. Kuindersma. Finding Asteroids Down the Back of the Couch: A Novel Approach to the Minor Planet Linking Problem. *arXiv e-prints*, art. arXiv:1805.02638, May 2018.

P. C. Hough V. Method and means for recognizing complex patterns, Dec. 1962. URL `https://patents.google.com/patent/US3069654A`.

J. D. Hunter. Matplotlib: A 2D Graphics Environment. *Computing in Science and Engineering*, 9:90–95, May 2007. doi: 10.1109/MCSE.2007.55.

S. Ida and J. Makino. N-Body simulation of gravitational interaction between planetesimals and a protoplanet . I. velocity distribution of planetesimals. , 96(1):107–120, Mar. 1992. doi: 10.1016/0019-1035(92)90008-U.

Ž. Ivezić, S. Tabachnik, R. Rafikov, R. H. Lupton, T. Quinn, M. Hammergren, L. Eyer, J. Chu, J. C. Armstrong, X. Fan, K. Finlator, T. R. Geballe, J. E. Gunn, G. S. Hennessy, G. R. Knapp, S. K. Leggett, J. A. Munn, J. R. Pier, C. M. Rockosi, D. P. Schneider, M. A. Strauss, B. Yanny, J. Brinkmann, I. Csabai, R. B. Hindsley, S. Kent, D. Q. Lamb, B. Margon, T. A. McKay, J. A. Smith, P. Waddel, D. G. York, and SDSS Collaboration. Solar System Objects Observed in the Sloan Digital Sky Survey Commissioning Data. , 122(5):2749–2784, Nov. 2001. doi: 10.1086/323452.

Ž. Ivezić, S. M. Kahn, J. A. Tyson, B. Abel, E. Acosta, R. Allsman, D. Alonso, Y. AlSayyad, S. F. Anderson, J. Andrew, J. R. P. Angel, G. Z. Angeli, R. Ansari, P. Antilogus, C. Araujo, R. Armstrong, K. T. Arndt, P. Astier, É. Aubourg, N. Auza, T. S. Axelrod, D. J. Bard, J. D. Barr, A. Barrau, J. G. Bartlett, A. E. Bauer, B. J. Bauman, S. Baumont, E. Bechtol, K. Bechtol, A. C. Becker, J. Becla, C. Beldica, S. Bellavia, F. B. Bianco, R. Biswas, G. Blanc, J. Blazek, R. D. Bland ford, J. S. Bloom, J. Bogart, T. W. Bond, M. T. Booth, A. W. Borgland, K. Borne, J. F. Bosch, D. Boutigny, C. A. Brackett, A. Bradshaw, W. N. Brand t, M. E. Brown, J. S. Bullock, P. Burchat, D. L. Burke, G. Cagnoli, D. Calabrese, S. Callahan, A. L. Callen, J. L. Carlin, E. L. Carlson, S. Chand rasekharan, G. Charles-Emerson, S. Chesley, E. C. Cheu, H.-F. Chiang, J. Chiang, C. Chirino, D. Chow, D. R.

Ciardi, C. F. Claver, J. Cohen-Tanugi, J. J. Cockrum, R. Coles, A. J. Connolly, K. H. Cook, A. Cooray, K. R. Covey, C. Cribbs, W. Cui, R. Cutri, P. N. Daly, S. F. Daniel, F. Daruich, G. Daubard, G. Daues, W. Dawson, F. Delgado, A. Dellapenna, R. de Peyster, M. de Val-Borro, S. W. Digel, P. Doherty, R. Dubois, G. P. Dubois-Felsmann, J. Durech, F. Economou, T. Eifler, M. Eracleous, B. L. Emmons, A. Fausti Neto, H. Ferguson, E. Figueroa, M. Fisher-Levine, W. Focke, M. D. Foss, J. Frank, M. D. Freemon, E. Gangler, E. Gawiser, J. C. Geary, P. Gee, M. Geha, C. J. B. Gessner, R. R. Gibson, D. K. Gilmore, T. Glanzman, W. Glick, T. Goldina, D. A. Goldstein, I. Goodenow, M. L. Graham, W. J. Gressler, P. Gris, L. P. Guy, A. Guyonnet, G. Haller, R. Harris, P. A. Hascall, J. Haupt, F. Hernand ez, S. Herrmann, E. Hileman, J. Hoblitt, J. A. Hodgson, C. Hogan, J. D. Howard, D. Huang, M. E. Huffer, P. Ingraham, W. R. Innes, S. H. Jacoby, B. Jain, F. Jammes, M. J. Jee, T. Jenness, G. Jernigan, D. Jevremović, K. Johns, A. S. Johnson, M. W. G. Johnson, R. L. Jones, C. Juramy-Gilles, M. Jurić, J. S. Kalirai, N. J. Kallivayalil, B. Kalmbach, J. P. Kantor, P. Karst, M. M. Kasliwal, H. Kelly, R. Kessler, V. Kinnison, D. Kirkby, L. Knox, I. V. Kotov, V. L. Krabbendam, K. S. Krughoff, P. Kubánek, J. Kuczewski, S. Kulkarni, J. Ku, N. R. Kurita, C. S. Lage, R. Lambert, T. Lange, J. B. Langton, L. Le Guillou, D. Levine, M. Liang, K.-T. Lim, C. J. Lintott, K. E. Long, M. Lopez, P. J. Lotz, R. H. Lupton, N. B. Lust, L. A. MacArthur, A. Mahabal, R. Mand elbaum, T. W. Markiewicz, D. S. Marsh, P. J. Marshall, S. Marshall, M. May, R. McKercher, M. McQueen, J. Meyers, M. Migliore, M. Miller, D. J. Mills, C. Miraval, J. Moeyens, F. E. Moolekamp, D. G. Monet, M. Moniez, S. Monkewitz, C. Montgomery, C. B. Morrison, F. Mueller, G. P. Muller, F. Muñoz Arancibia, D. R. Neill, S. P. Newbry, J.-Y. Nief, A. Nomerotski, M. Nordby, P. O'Connor, J. Oliver, S. S. Olivier, K. Olsen, W. O'Mullane, S. Ortiz, S. Osier, R. E. Owen, R. Pain, P. E. Palecek, J. K. Parejko, J. B. Parsons, N. M. Pease, J. M. Peterson, J. R. Peterson, D. L. Petravick, M. E. Libby Petrick, C. E. Petry, F. Pierfederici, S. Pietrowicz, R. Pike, P. A. Pinto, R. Plante, S. Plate, J. P. Plutchak, P. A. Price, M. Prouza, V. Radeka, J. Rajagopal, A. P. Rasmussen, N. Regnault, K. A. Reil, D. J. Reiss, M. A. Reuter, S. T. Ridgway, V. J. Riot, S. Ritz, S. Robinson, W. Roby, A. Roodman, W. Rosing, C. Roucelle, M. R. Rumore, S. Russo, A. Saha, B. Sassolas, T. L. Schalk, P. Schellart, R. H. Schindler, S. Schmidt, D. P. Schneider, M. D. Schneider, W. Schoening, G. Schumacher, M. E. Schwamb, J. Sebag, B. Selvy, G. H. Sembroski, L. G. Seppala, A. Serio, E. Serrano, R. A. Shaw, I. Shipsey, J. Sick, N. Silvestri, C. T. Slater, J. A. Smith, R. C. Smith, S. Sobhani, C. Soldahl, L. Storrie-Lombardi, E. Stover, M. A. Strauss, R. A. Street, C. W. Stubbs, I. S. Sullivan, D. Sweeney, J. D. Swinbank, A. Szalay, P. Takacs, S. A. Tether, J. J. Thaler, J. G. Thayer, S. Thomas, A. J. Thornton, V. Thukral, J. Tice, D. E. Trilling, M. Turri, R. Van Berg, D. Vanden Berk, K. Vetter, F. Virieux, T. Vucina, W. Wahl, L. Walkowicz, B. Walsh, C. W. Walter, D. L. Wang, S.-Y. Wang, M. Warner, O. Wiecha, B. Willman, S. E. Winters, D. Wittman, S. C. Wolff, W. M. Wood-Vasey, X. Wu, B. Xin, P. Yoachim, and H. Zhan. LSST: From Science Drivers to Reference Design and Anticipated Data Products. , 873(2):111, Mar. 2019. doi: 10.3847/1538-4357/ab042c.

R. Jedicke, L. Denneau, T. Grav, J. Heasley, J. Kubica, and Pan-STARRS Collaboration.

The Pan-STARRS Moving Object Processing System. In *AAS/Division for Planetary Sciences Meeting Abstracts #37*, volume 37 of *AAS/Division for Planetary Sciences Meeting Abstracts*, page 14.04, Aug. 2005.

D. Jewitt, H. Hsieh, and J. Agarwal. The Active Asteroids. In *Asteroids IV*, pages 221–241. 2015. doi: 10.2458/azu_uapress_9780816532131-ch012.

C. I. Johnson, R. M. Rich, M. D. Young, I. T. Simion, W. I. Clarkson, C. A. Pilachowski, S. Michael, A. Kunder, A. Koch, and A. K. Vivas. Blanco DECam Bulge Survey (BDBS) II: project performance, data analysis, and early science results. , 499(2):2357–2379, Dec. 2020. doi: 10.1093/mnras/staa2393.

E. Jones, T. Oliphant, P. Peterson, et al. SciPy: Open source scientific tools for Python, 2001–. URL `http://www.scipy.org/`.

R. L. Jones, M. Jurić, and Ž. Ivezić. Asteroid Discovery and Characterization with the Large Synoptic Survey Telescope. In S. R. Chesley, A. Morbidelli, R. Jedicke, and D. Farnocchia, editors, *Asteroids: New Observations, New Models*, volume 318 of *IAU Symposium*, pages 282–292, Jan. 2016. doi: 10.1017/S1743921315008510.

M. Jurić, Ž. Ivezić, and R. H. Lupton. The Sloan Digital Sky Survey Moving Object Catalog. In *American Astronomical Society Meeting Abstracts*, volume 201 of *American Astronomical Society Meeting Abstracts*, page 45.06, Dec. 2002.

M. Juric, Z. Ivezic, R. Lupton, and SDSS Collaboration. The SDSS Moving Object Catalog, Asteroid Data Release 4. In *American Astronomical Society Meeting Abstracts*, volume 211 of *American Astronomical Society Meeting Abstracts*, page 56.05, Dec. 2007.

T. Khain, K. Batygin, and M. E. Brown. The Generation of the Distant Kuiper Belt by Planet Nine from an Initially Broad Perihelion Distribution. , 155(6):250, June 2018. doi: 10.3847/1538-3881/aac212.

T. Kleine, G. Budde, C. Burkhardt, T. S. Kruijer, E. A. Worsham, A. Morbidelli, and F. Nimmo. The Non-carbonaceous-Carbonaceous Meteorite Dichotomy. , 216(4):55, May 2020. doi: 10.1007/s11214-020-00675-w.

Z. Knežević. The History of Asteroid Family Identification. In *IAU General Assembly*, pages 5–6, Mar. 2020. doi: 10.1017/S1743921319003211.

Z. Knežević, A. Milani, A. Cellino, B. Novaković, F. Spoto, and P. Paolicchi. Automated Classification of Asteroids into Families at Work. In *Complex Planetary Systems, Proceedings of the International Astronomical Union*, volume 310, pages 130–133, July 2014. doi: 10.1017/S1743921314008035.

C. Koeberl and B. A. Ivanov. Asteroid impact effects on Snowball Earth. *Meteoritics and Planetary Science*, 54(10):2273–2285, Oct. 2019. doi: 10.1111/maps.13294.

E. Kokubo and S. Ida. Formation of Protoplanets from Planetesimals. In G. Lemarchand and K. Meech, editors, *Bioastronomy 99*, volume 213 of *Astronomical Society of the Pacific Conference Series*, page 51, Jan. 2000.

G. A. Krasinsky, E. V. Pitjeva, M. V. Vasilyev, and E. I. Yagudina. Hidden Mass in the Asteroid Belt. , 158(1):98–105, July 2002. doi: 10.1006/icar.2002.6837.

T. S. Kruijer, C. Burkhardt, G. Budde, and T. Kleine. Age of Jupiter inferred from the distinct genetics and formation times of meteorites. *Proceedings of the National Academy of Science*, 114(26):6712–6716, June 2017. doi: 10.1073/pnas.1704461114.

G. P. Kuiper, Y. Fujita, T. Gehrels, I. Groeneveld, J. Kent, G. van Biesbroeck, and C. J. van Houten. Survey of Asteroids. , 3:289–427, July 1958. doi: 10.1086/190037.

M. Lambrechts and A. Johansen. Forming the cores of giant planets from the radial pebble flux in protoplanetary discs. , 572:A107, Dec. 2014. doi: 10.1051/0004-6361/201424343.

S. Larson, J. Brownlee, C. Hergenrother, and T. Spahr. The Catalina Sky Survey for NEOs. In *Bulletin of the American Astronomical Society*, volume 30, page 1037, Sept. 1998.

A. Lemaitre. Asteroid family classification from very large catalogues. In Z. Knežević and A. Milani, editors, *IAU Colloq. 197: Dynamics of Populations of Planetary Systems*, pages 135–144, Feb. 2005. doi: 10.1017/S1743921304008592.

M. Lieu, L. Conversi, B. Altieri, and B. Carry. Detecting Solar system objects with convolutional neural networks. , 485(4):5831–5842, June 2019. doi: 10.1093/mnras/stz761.

H. W. Lin, Y.-T. Chen, M. J. Holman, W.-H. Ip, M. J. Payne, P. Lacerda, W. C. Fraser, D. W. Gerdes, A. Bieryla, Z. F. Sie, W. P. Chen, W. S. Burgett, L. Denneau, R. Jedicke, N. Kaiser, E. A. Magnier, J. L. Tonry, R. J. Wainscoat, and C. Waters. The Pan-STARRS 1 Discoveries of Five New Neptune Trojans. , 152(5):147, Nov. 2016. doi: 10.3847/0004-6256/152/5/147.

L. Lindegren, S. A. Klioner, J. Hernández, A. Bombrun, M. Ramos-Lerate, H. Steidelmüller, U. Bastian, M. Biermann, A. de Torres, E. Gerlach, R. Geyer, T. Hilger, D. Hobbs, U. Lammers, P. J. McMillan, C. A. Stephenson, J. Castañeda, M. Davidson, C. Fabricius, G. Gracia-Abril, J. Portell, N. Rowell, D. Teyssier, F. Torra, S. Bartolomé, M. Clotet, N. Garralda, J. J. González-Vidal, J. Torra, U. Abbas, M. Altmann, E. Anglada Varela, L. Balaguer-Núñez, Z. Balog, C. Barache, U. Becciani, M. Bernet, S. Bertone, L. Bianchi, S. Bouquillon, A. G. A. Brown, B. Bucciarelli, D. Busonero, A. G. Butkevich, R. Buzzi, R. Cancelliere, T. Carlucci, P. Charlot, M. R. L. Cioni, M. Crosta, C. Crowley, E. F. del Peloso, E. del Pozo, R. Drimmel, P. Esquej, A. Fienga, E. Fraile, M. Gai, M. Garcia-Reinaldos, R. Guerra, N. C. Hambly, M. Hauser, K. Janßen, S. Jordan, Z. Kostrzewa-Rutkowska, M. G. Lattanzi, S. Liao, E. Licata, T. A. Lister, W. Löffler, J. M. Marchant, A. Masip, F. Mignard, A. Mints, D. Molina, A. Mora, R. Morbidelli, C. P. Murphy, C. Pagani, P. Panuzzo, X. Peñalosa Esteller, E. Poggio, P. Re Fiorentin, A. Riva,

A. Sagristà Sellés, V. Sanchez Gimenez, M. Sarasso, E. Sciacca, H. I. Siddiqui, R. L. Smart, D. Souami, A. Spagna, I. A. Steele, F. Taris, E. Utrilla, W. van Reeven, and A. Vecchiato. Gaia Early Data Release 3. The astrometric solution. , 649:A2, May 2021. doi: 10.1051/0004-6361/202039709.

E. A. Magnier, E. F. Schlafly, D. P. Finkbeiner, J. L. Tonry, B. Goldman, S. Röser, E. Schilbach, S. Casertano, K. C. Chambers, H. A. Flewelling, M. E. Huber, P. A. Price, W. E. Sweeney, C. Z. Waters, L. Denneau, P. W. Draper, K. W. Hodapp, R. Jedicke, N. Kaiser, R. P. Kudritzki, N. Metcalfe, C. W. Stubbs, and R. J. Wainscoat. Pan-STARRS Photometric and Astrometric Calibration. , 251(1):6, Nov. 2020. doi: 10.3847/1538-4365/abb82a.

A. Mainzer, T. Grav, J. Bauer, J. Masiero, R. S. McMillan, R. M. Cutri, R. Walker, E. Wright, P. Eisenhardt, D. J. Tholen, T. Spahr, R. Jedicke, L. Denneau, E. DeBaun, D. Elsbury, T. Gautier, S. Gomillion, E. Hand, W. Mo, J. Watkins, A. Wilkins, G. L. Bryngelson, A. Del Pino Molina, S. Desai, M. Gómez Camus, S. L. Hidalgo, I. Konstantopoulos, J. A. Larsen, C. Maleszewski, M. A. Malkan, J. C. Mauduit, B. L. Mullan, E. W. Olszewski, J. Pforr, A. Saro, J. V. Scotti, and L. H. Wasserman. NEOWISE Observations of Near-Earth Objects: Preliminary Results. , 743(2):156, Dec. 2011. doi: 10.1088/0004-637X/743/2/156.

S. Marchi, B. Black, N. Drabon, D. Ebel, R. Fu, B. Johnson, T. Schulz, and K. Wuennemann. Understanding the Effects of Asteroid Collisions Across Earth's Great Oxidation 3.5-2 Ga. *LPI Contributions*, 2134:1008, Sept. 2019.

L. Markwardt, D. W. Gerdes, R. Malhotra, J. C. Becker, S. J. Hamilton, and F. C. Adams. Search for L5 Earth Trojans with DECam. , 492(4):6105–6119, Mar. 2020. doi: 10.1093/mnras/staa232.

A. McNeill, N. Erasmus, D. E. Trilling, J. P. Emery, J. L. Tonry, L. Denneau, H. Flewelling, A. Heinze, B. Stalder, and H. J. Weiland. Comparison of the Physical Properties of the L4 and L5 Trojan Asteroids from ATLAS Data. , 2(1):6, Feb. 2021. doi: 10.3847/PSJ/abcccd.

A. Milani, A. Cellino, Z. Knežević, B. Novaković, F. Spoto, and P. Paolicchi. Asteroid families classification: Exploiting very large datasets. , 239:46–73, Sept. 2014. doi: 10.1016/j.icarus.2014.05.039.

J. Moeyens and M. Juric. THOR: An Algorithm for Cadence-Independent Asteroid Discovery. In *EPSC-DPS Joint Meeting 2019*, volume 2019, pages EPSC–DPS2019–1404, Sept. 2019.

J. Moeyens, M. Juric, S. Nelson, J. Ford, D. Bektesevic, A. Connolly, S. Eggl, Z. Ivezic, L. Jones, J. B. Kalmbach, and H. Smotherman. THOR: Searching for Asteroids Without Tracklets. In *AAS/Division for Planetary Sciences Meeting Abstracts*, volume 53 of *AAS/Division for Planetary Sciences Meeting Abstracts*, page 101.07, Oct. 2021.

F. Moreno, A. C. Bagatin, G. Tancredi, J.-Y. Li, A. Rossi, F. Ferrari, M. Hirabayashi, E. Fahnestock, A. Maury, R. Sandness, A. S. Rivkin, A. Cheng, T. L. Farnham, S. Soldini, C. Giordano, G. Merisio, P. Panicucci, M. Pugliatti, A. J. Castro-Tirado, E. Fernández-García, i. Pérez-García, S. Ivanovski, A. Penttila, L. Kolokolova, J. Licandro, O. Muñoz, Z. Gray, J. L. Ortiz, and Z.-Y. Lin. Characterization of the Ejecta from the NASA/DART Impact on Dimorphos: Observations and Monte Carlo Models. , 4(8):138, Aug. 2023. doi: 10.3847/PSJ/ace827.

D. Morrison. The Spaceguard Survey: Report of the NASA International Near-Earth-Object Detection Workshop, Jan. 1992.

D. Nesvorný, R. Jedicke, R. J. Whiteley, and Ž. Ivezić. Evidence for asteroid space weathering from the Sloan Digital Sky Survey. , 173(1):132–152, Jan. 2005. doi: 10.1016/j.icarus.2004.07.026.

D. Nesvorný, M. Brož, and V. Carruba. Identification and Dynamical Properties of Asteroid Families. In *Asteroids IV*, pages 297–321. 2015. doi: 10.2458/azu_uapress_9780816532131-ch016.

D. Nesvorný, N. Dauphas, D. Vokrouhlický, R. Deienno, and T. Hopp. Isotopic trichotomy of main belt asteroids from implantation of outer solar system planetesimals. *Earth and Planetary Science Letters*, 626:118521, Jan. 2024. doi: 10.1016/j.epsl.2023.118521.

D. L. Nidever, K. Olsen, A. R. Walker, A. K. Vivas, R. D. Blum, C. Kaleida, Y. Choi, B. C. Conn, R. A. Gruendl, E. F. Bell, G. Besla, R. R. Muñoz, C. Gallart, N. F. Martin, E. W. Olszewski, A. Saha, A. Monachesi, M. Monelli, T. J. L. de Boer, L. C. Johnson, D. Zaritsky, G. S. Stringfellow, R. P. van der Marel, M.-R. L. Cioni, S. Jin, S. R. Majewski, D. Martinez-Delgado, L. Monteagudo, N. E. D. Noël, E. J. Bernard, A. Kunder, Y.-H. Chu, C. P. M. Bell, F. Santana, J. Frechem, G. E. Medina, V. Parkash, J. C. Serón Navarrete, and C. Hayes. SMASH: Survey of the MAgellanic Stellar History. , 154:199, Nov. 2017. doi: 10.3847/1538-3881/aa8d1c.

D. L. Nidever, A. Dey, K. Olsen, S. Ridgway, R. Nikutta, S. Juneau, M. Fitzpatrick, A. Scott, and F. Valdes. First Data Release of the All-sky NOAO Source Catalog. , 156(3):131, Sep 2018. doi: 10.3847/1538-3881/aad68f.

D. L. Nidever, A. Dey, K. Fasbender, S. Juneau, A. M. Meisner, J. Wishart, A. Scott, K. Matt, R. Nikutta, and R. Pucha. Second Data Release of the All-sky NOIRLab Source Catalog. *arXiv e-prints*, art. arXiv:2011.08868, Nov. 2020.

D. L. Nidever, A. Dey, K. Fasbender, S. Juneau, A. M. Meisner, J. Wishart, A. Scott, K. Matt, R. Nikutta, and R. Pucha. Second Data Release of the All-sky NOIRLab Source Catalog. , 161(4):192, Apr. 2021. doi: 10.3847/1538-3881/abd6e1.

B. Novaković, D. Vokrouhlický, F. Spoto, and D. Nesvorný. Asteroid families: properties, recent advances, and future opportunities. *Celestial Mechanics and Dynamical Astronomy*, 134(4):34, Aug. 2022. doi: 10.1007/s10569-022-10091-7.

D. P. O'Brien, K. J. Walsh, A. Morbidelli, S. N. Raymond, and A. M. Mandell. Water delivery and giant impacts in the 'Grand Tack' scenario. , 239:74–84, Sept. 2014. doi: 10.1016/j.icarus.2014.05.009.

C. A. Onken, C. Wolf, M. S. Bessell, S.-W. Chang, L. C. Luvaul, J. L. Tonry, M. C. White, and G. S. Da Costa. SkyMapper Southern Survey: Data Release 4. *arXiv e-prints*, art. arXiv:2402.02015, Feb. 2024. doi: 10.48550/arXiv.2402.02015.

N. Padmanabhan, D. J. Schlegel, D. P. Finkbeiner, J. C. Barentine, M. R. Blanton, H. J. Brewington, J. E. Gunn, M. Harvanek, D. W. Hogg, Ž. Ivezić, D. Johnston, S. M. Kent, S. J. Kleinman, G. R. Knapp, J. Krzesinski, D. Long, J. Neilsen, Eric H., A. Nitta, C. Loomis, R. H. Lupton, S. Roweis, S. A. Snedden, M. A. Strauss, and D. L. Tucker. An Improved Photometric Calibration of the Sloan Digital Sky Survey Imaging Data. , 674 (2):1217–1233, Feb. 2008. doi: 10.1086/524677.

A. Parker, Ž. Ivezić, M. Jurić, R. Lupton, M. D. Sekora, and A. Kowalski. The size distributions of asteroid families in the SDSS Moving Object Catalog 4. , 198(1):138–155, Nov. 2008. doi: 10.1016/j.icarus.2008.07.002.

F. Pedregosa, G. Varoquaux, A. Gramfort, V. Michel, B. Thirion, O. Grisel, M. Blondel, P. Prettenhofer, R. Weiss, V. Dubourg, J. Vanderplas, A. Passos, D. Cournapeau, M. Brucher, M. Perrot, and E. Duchesnay. Scikit-learn: Machine learning in Python. *Journal of Machine Learning Research*, 12:2825–2830, 2011.

J. Peña, C. Fuentes, F. Förster, J. Martínez-Palomera, G. Cabrera-Vives, J. C. Maureira, P. Huijse, P. A. Estévez, L. Galbany, S. González-Gaitán, and T. de Jaeger. Asteroids' size distribution and colors from HITS. *The Astronomical Journal*, 159(4):148, mar 2020. doi: 10.3847/1538-3881/ab7338. URL `https://doi.org/10.3847%2F1538-3881%2Fab7338`.

V. Perdelwitz, M. Völschow, and H. M. Müller. A new approach to distant solar system object detection in large survey data sets. , 615:A159, Aug. 2018. doi: 10.1051/0004-6361/201732254.

F. Pérez and B. E. Granger. IPython: a system for interactive scientific computing. *Computing in Science and Engineering*, 9(3):21–29, May 2007. ISSN 1521-9615. doi: 10.1109/MCSE.2007.53. URL `http://ipython.org`.

O. P. Popova, P. Jenniskens, V. Emel'yanenko, A. Kartashova, E. Biryukov, S. Khaibrakhmanov, V. Shuvalov, Y. Rybnov, A. Dudorov, V. I. Grokhovsky, D. D. Badyukov, Q.-Z. Yin, P. S. Gural, J. Albers, M. Granvik, L. G. Evers, J. Kuiper, V. Kharlamov, A. Solovyov, Y. S. Rusakov, S. Korotkiy, I. Serdyuk, A. V. Korochantsev, M. Y. Larionov, D. Glazachev, A. E. Mayer, G. Gisler, S. V. Gladkovsky, J. Wimpenny,

M. E. Sanborn, A. Yamakawa, K. L. Verosub, D. J. Rowland, S. Roeske, N. W. Botto, J. M. Friedrich, M. E. Zolensky, L. Le, D. Ross, K. Ziegler, T. Nakamura, I. Ahn, J. I. Lee, Q. Zhou, X.-H. Li, Q.-L. Li, Y. Liu, G.-Q. Tang, T. Hiroi, D. Sears, I. A. Weinstein, A. S. Vokhmintsev, A. V. Ishchenko, P. Schmitt-Kopplin, N. Hertkorn, K. Nagao, M. K. Haba, M. Komatsu, T. Mikouchi, and aff34. Chelyabinsk Airburst, Damage Assessment, Meteorite Recovery, and Characterization. *Science*, 342(6162):1069–1073, Nov. 2013. doi: 10.1126/science.1242642.

S. H. Pravdo, D. L. Rabinowitz, E. F. Helin, K. J. Lawrence, R. J. Bambery, C. C. Clark, S. L. Groom, S. Levin, J. Lorre, S. B. Shaklan, P. Kervin, J. A. Africano, P. Sydney, and V. Soohoo. The Near-Earth Asteroid Tracking (NEAT) Program: an Automated System for Telescope Control, Wide-Field Imaging, and Object Detection. , 117(3):1616–1633, Mar. 1999. doi: 10.1086/300769.

D. L. Rabinowitz. Detection of earth-approaching asteroids in near real time. , 101:1518–1529, Apr. 1991. doi: 10.1086/115785.

J. Radon. Translated as 'on determining functions from their integral values along certain manifolds' by p.c. parks (1986). *Medical Imaging, IEEE Transactions on*, 5:170 – 176, 01 1917. doi: 10.1109/TMI.1986.4307775.

S. N. Raymond and D. Nesvorný. Origin and Dynamical Evolution of the Asteroid Belt. In *Vesta and Ceres. Insights from the Dawn Mission for the Origin of the Solar System*, page 227. 2022. doi: 10.1017/9781108856324.019.

A. Rest, B. Sinnott, D. L. Welch, J. L. Prieto, F. B. Bianco, T. Matheson, R. C. Smith, and N. B. Suntzeff. Light Echoes of Ancient Transients with the Blanco 4m Telescope. In S. Points and A. Kunder, editors, *Fifty Years of Wide Field Studies in the Southern Hemisphere: Resolved Stellar Populations of the Galactic Bulge and Magellanic Clouds*, volume 491 of *Astronomical Society of the Pacific Conference Series*, page 247, May 2015.

R. M. Rich. The Galactic Bulge. In S. Points and A. Kunder, editors, *Fifty Years of Wide Field Studies in the Southern Hemisphere: Resolved Stellar Populations of the Galactic Bulge and Magellanic Clouds*, volume 491 of *Astronomical Society of the Pacific Conference Series*, page 59, May 2015.

T. Saifollahi, G. Verdoes Kleijn, R. Williams, M. Micheli, T. Santana-Ros, E. Helmich, D. Koschny, and L. Conversi. Mining archival data from wide-field astronomical surveys in search of near-Earth objects. , 673:A93, May 2023. doi: 10.1051/0004-6361/202345957.

E. F. Schlafly, G. M. Green, D. Lang, T. Daylan, D. P. Finkbeiner, A. Lee, A. M. Meisner, D. Schlegel, and F. Valdes. The DECam Plane Survey: Optical Photometry of Two Billion Objects in the Southern Galactic Plane. , 234(2):39, Feb. 2018. doi: 10.3847/1538-4365/aaa3e2.

D. J. Schlegel, D. P. Finkbeiner, and M. Davis. Maps of Dust Infrared Emission for Use in Estimation of Reddening and Cosmic Microwave Background Radiation Foregrounds. , 500(2):525–553, June 1998. doi: 10.1086/305772.

M. E. Schwamb, W. C. Fraser, M. T. Bannister, M. Marsset, R. E. Pike, J. J. Kavelaars, S. D. Benecchi, M. J. Lehner, S.-Y. Wang, A. Thirouin, A. Delsanti, N. Peixinho, K. Volk, M. Alexandersen, Y.-T. Chen, B. Gladman, S. D. J. Gwyn, and J.-M. Petit. Col-OSSOS: The Colors of the Outer Solar System Origins Survey. , 243(1):12, July 2019. doi: 10.3847/1538-4365/ab2194.

M. E. Schwamb, R. L. Jones, P. Yoachim, K. Volk, R. C. Dorsey, C. Opitom, S. Greenstreet, T. Lister, C. Snodgrass, B. T. Bolin, L. Inno, M. T. Bannister, S. Eggl, M. Solontoi, M. S. P. Kelley, M. Jurić, H. W. Lin, D. Ragozzine, P. H. Bernardinelli, S. R. Chesley, T. Daylan, J. Ďurech, W. C. Fraser, M. Granvik, M. M. Knight, C. M. Lisse, R. Malhotra, W. J. Oldroyd, A. Thirouin, and Q. Ye. Tuning the Legacy Survey of Space and Time (LSST) Observing Strategy for Solar System Science. , 266(2):22, June 2023. doi: 10.3847/1538-4365/acc173.

S. S. Sheppard and C. A. Trujillo. The Size Distribution of the Neptune Trojans and the Missing Intermediate-sized Planetesimals. , 723(2):L233–L237, Nov 2010. doi: 10.1088/2041-8205/723/2/L233.

S. S. Sheppard, C. A. Trujillo, D. J. Tholen, and N. Kaib. A New High Perihelion Trans-Plutonian Inner Oort Cloud Object: 2015 TG387. , 157(4):139, Apr. 2019. doi: 10.3847/1538-3881/ab0895.

M. F. Skrutskie, R. M. Cutri, R. Stiening, M. D. Weinberg, S. Schneider, J. M. Carpenter, C. Beichman, R. Capps, T. Chester, J. Elias, J. Huchra, J. Liebert, C. Lonsdale, D. G. Monet, S. Price, P. Seitzer, T. Jarrett, J. D. Kirkpatrick, J. E. Gizis, E. Howard, T. Evans, J. Fowler, L. Fullmer, R. Hurt, R. Light, E. L. Kopan, K. A. Marsh, H. L. McCallon, R. Tam, S. Van Dyk, and S. Wheelock. The Two Micron All Sky Survey (2MASS). , 131 (2):1163–1183, Feb. 2006. doi: 10.1086/498708.

T. Stefanut, V. Bacu, C. Nandra, D. Balasz, D. Gorgan, and O. Vaduvescu. NEARBY Platform: Algorithm for Automated Asteroids Detection in Astronomical Images. *arXiv e-prints*, art. arXiv:1901.02545, Jan. 2019.

P. B. Stetson. DAOPHOT: A Computer Program for Crowded-Field Stellar Photometry. , 99:191, Mar. 1987. doi: 10.1086/131977.

P. B. Stetson. On the Growth-Curve Method for Calibrating Stellar Photometry with CCDs. , 102:932, Aug. 1990. doi: 10.1086/132719.

G. H. Stokes, J. B. Evans, H. E. M. Viggh, F. C. Shelly, and E. C. Pearce. Lincoln Near-Earth Asteroid Program (LINEAR). , 148(1):21–28, Nov. 2000. doi: 10.1006/icar.2000.6493.

P. Tanga, T. Pauwels, F. Mignard, K. Muinonen, A. Cellino, P. David, D. Hestroffer, F. Spoto, J. Berthier, J. Guiraud, W. Roux, B. Carry, M. Delbo, A. Dell'Oro, C. Fouron, L. Galluccio, A. Jonckheere, S. A. Klioner, Y. Lefustec, L. Liberato, C. Ordénovic, I. Oreshina-Slezak, A. Penttilä, F. Pailler, C. Panem, J. M. Petit, J. Portell, E. Poujoulet, W. Thuillot, E. Van Hemelryck, A. Burlacu, Y. Lasne, and S. Managau. Gaia Data Release 3. The Solar System survey. , 674:A12, June 2023. doi: 10.1051/0004-6361/202243796.

T. Terai, J. Takahashi, and Y. Itoh. High Ecliptic Latitude Survey for Small Main-belt Asteroids. , 146(5):111, Nov. 2013. doi: 10.1088/0004-6256/146/5/111.

The Astropy Collaboration, A. M. Price-Whelan, B. M. Sipőcz, H. M. Günther, P. L. Lim, S. M. Crawford, S. Conseil, D. L. Shupe, M. W. Craig, N. Dencheva, A. Ginsburg, J. T. VanderPlas, L. D. Bradley, D. Pérez-Suárez, M. de Val-Borro, T. L. Aldcroft, K. L. Cruz, T. P. Robitaille, E. J. Tollerud, C. Ardelean, T. Babej, M. Bachetti, A. V. Bakanov, S. P. Bamford, G. Barentsen, P. Barmby, A. Baumbach, K. L. Berry, F. Biscani, M. Boquien, K. A. Bostroem, L. G. Bouma, G. B. Brammer, E. M. Bray, H. Breytenbach, H. Buddelmeijer, D. J. Burke, G. Calderone, J. L. Cano Rodríguez, M. Cara, J. V. M. Cardoso, S. Cheedella, Y. Copin, D. Crichton, D. DÁvella, C. Deil, É. Depagne, J. P. Dietrich, A. Donath, M. Droettboom, N. Earl, T. Erben, S. Fabbro, L. A. Ferreira, T. Finethy, R. T. Fox, L. H. Garrison, S. L. J. Gibbons, D. A. Goldstein, R. Gommers, J. P. Greco, P. Greenfield, A. M. Groener, F. Grollier, A. Hagen, P. Hirst, D. Homeier, A. J. Horton, G. Hosseinzadeh, L. Hu, J. S. Hunkeler, Ž. Ivezić, A. Jain, T. Jenness, G. Kanarek, S. Kendrew, N. S. Kern, W. E. Kerzendorf, A. Khvalko, J. King, D. Kirkby, A. M. Kulkarni, A. Kumar, A. Lee, D. Lenz, S. P. Littlefair, Z. Ma, D. M. Macleod, M. Mastropietro, C. McCully, S. Montagnac, B. M. Morris, M. Mueller, S. J. Mumford, D. Muna, N. A. Murphy, S. Nelson, G. H. Nguyen, J. P. Ninan, M. Nöthe, S. Ogaz, S. Oh, J. K. Parejko, N. Parley, S. Pascual, R. Patil, A. A. Patil, A. L. Plunkett, J. X. Prochaska, T. Rastogi, V. Reddy Janga, J. Sabater, P. Sakurikar, M. Seifert, L. E. Sherbert, H. Sherwood-Taylor, A. Y. Shih, J. Sick, M. T. Silbiger, S. Singanamalla, L. P. Singer, P. H. Sladen, K. A. Sooley, S. Sornarajah, O. Streicher, P. Teuben, S. W. Thomas, G. R. Tremblay, J. E. H. Turner, V. Terrón, M. H. van Kerkwijk, A. de la Vega, L. L. Watkins, B. A. Weaver, J. B. Whitmore, J. Woillez, and V. Zabalza. The Astropy Project: Building an inclusive, open-science project and status of the v2.0 core package. *ArXiv e-prints*, Jan. 2018.

D. J. Tholen and M. A. Barucci. Asteroid taxonomy. In R. P. Binzel, T. Gehrels, and M. S. Matthews, editors, *Asteroids II*, pages 298–315, Jan. 1989.

J. L. Tonry, L. Denneau, A. N. Heinze, B. Stalder, K. W. Smith, S. J. Smartt, C. W. Stubbs, H. J. Weiland , and A. Rest. ATLAS: A High-cadence All-sky Survey System. , 130(988): 064505, June 2018. doi: 10.1088/1538-3873/aabadf.

A. Trinquier, J.-L. Birck, and C. J. Allègre. Widespread ^{54}Cr Heterogeneity in the Inner Solar System. , 655(2):1179–1185, Feb. 2007. doi: 10.1086/510360.

C. A. Trujillo and S. S. Sheppard. A Sedna-like body with a perihelion of 80 astronomical units. , 507(7493):471–474, Mar. 2014. doi: 10.1038/nature13156.

P. Veres and S. R. Chesley. Near-Earth Object Orbit Linking with the Large Synoptic Survey Telescope. , 154(13), Nov 2017.

P. Vereš, R. Jedicke, A. Fitzsimmons, L. Denneau, M. Granvik, B. Bolin, S. Chastel, R. J. Wainscoat, W. S. Burgett, K. C. Chambers, H. Flewelling, N. Kaiser, E. A. Magnier, J. S. Morgan, P. A. Price, J. L. Tonry, and C. Waters. Absolute magnitudes and slope parameters for 250,000 asteroids observed by Pan-STARRS PS1 - Preliminary results. , 261:34–47, Nov. 2015. doi: 10.1016/j.icarus.2015.08.007.

D. Vokrouhlický, W. F. Bottke, S. R. Chesley, D. J. Scheeres, and T. S. Statler. The Yarkovsky and YORP Effects. In *Asteroids IV*, pages 509–531. 2015. doi: 10.2458/azu_uapress_9780816532131-ch027.

K. J. Walsh, A. Morbidelli, S. N. Raymond, D. P. O'Brien, and A. M. Mandell. A low mass for Mars from Jupiter's early gas-driven migration. , 475(7355):206–209, July 2011. doi: 10.1038/nature10201.

S. v. d. Walt, S. C. Colbert, and G. Varoquaux. The numpy array: A structure for efficient numerical computation. *Computing in Science and Engg.*, 13(2):22–30, Mar. 2011. ISSN 1521-9615. doi: 10.1109/MCSE.2011.37. URL `http://dx.doi.org/10.1109/MCSE.2011.37`.

B. D. Warner, A. W. Harris, and P. Pravec. The asteroid lightcurve database. , 202(1): 134–146, July 2009. doi: 10.1016/j.icarus.2009.02.003.

P. H. Warren. Stable-isotopic anomalies and the accretionary assemblage of the Earth and Mars: A subordinate role for carbonaceous chondrites. *Earth and Planetary Science Letters*, 311(1):93–100, Nov. 2011. doi: 10.1016/j.epsl.2011.08.047.

R. Weryk, G. Williams, and R. Wainscoat. Linking Isolated Tracklets to Improve Asteroid Discovery. In *American Astronomical Society Meeting Abstracts*, American Astronomical Society Meeting Abstracts, page 329.05, Jan. 2020.

G. W. Wetherill and G. R. Stewart. Accumulation of a swarm of small planetesimals. , 77 (2):330–357, Feb. 1989. doi: 10.1016/0019-1035(89)90093-6.

Q. Ye, F. J. Masci, W.-H. Ip, T. A. Prince, G. Helou, D. Farnocchia, E. C. Bellm, R. Dekany, M. J. Graham, S. R. Kulkarni, T. Kupfer, A. Mahabal, C.-C. Ngeow, D. J. Reiley, and M. T. Soumagnac. A Twilight Search for Atiras, Vatiras, and Co-orbital Asteroids: Preliminary Results. , 159(2):70, Feb. 2020. doi: 10.3847/1538-3881/ab629c.

F. Yoshida and T. Nakamura. Subaru Main Belt Asteroid Survey (SMBAS)—Size and color distributions of small main-belt asteroids. , 55(9):1113–1125, June 2007. doi: 10.1016/j.pss.2006.11.016.

Y. Zhang and P. Michel. Shapes, structures, and evolution of small bodies. *Astrodynamics*, 5(4):293–329, Dec. 2021. doi: 10.1007/s42064-021-0128-7.

A. Zonca, L. Singer, D. Lenz, M. Reinecke, C. Rosset, E. Hivon, and K. Gorski. healpy: equal area pixelization and spherical harmonics transforms for data on the sphere in python. *Journal of Open Source Software*, 4(35):1298, Mar. 2019. doi: 10.21105/joss.01298. URL `https://doi.org/10.21105/joss.01298`.

H. Zou, X. Zhou, X. Fan, T. Zhang, Z. Zhou, J. Nie, X. Peng, I. McGreer, L. Jiang, A. Dey, D. Fan, B. He, Z. Jiang, D. Lang, M. Lesser, J. Ma, S. Mao, D. Schlegel, and J. Wang. Project Overview of the Beijing-Arizona Sky Survey. , 129(976):064101, June 2017. doi: 10.1088/1538-3873/aa65ba.